Development of a Method to Measure the Flexural Rigidity of Nanofibers

vorgelegt von
M. Sc.
Renata Fortini Moustafa Osman

an der Fakultät V - Verkehrs- und Maschinensysteme
der Technischen Universität Berlin
zur Erlangung des akademischen Grades

Doktorin der Ingenieurwissenschaften
-Dr.-Ing.-
genehmigte Dissertation

Promotionsausschuss:

Vorsitzender: Prof. Dr. rer. nat. Wolfgang H. Müller

Gutachter: Prof. Dr.-Ing. Utz von Wagner

Gutachter: Prof. Dr. rer. nat. Heinz Sturm

Gutachterin: Prof. Dr.-Ing. Kerstin Kracht

Tag der wissenschaftlichen Aussprache: 13. Mai 2022

Berlin 2022

Acknowledgment

I immensely appreciate the contribution of so many thoughtful people that participated in the completion of this thesis along the last five years. I am very thankful for their comments, their critics, their trust, their patience and their time.

To start, I would like to thank Dr. Pedro Dolabella Portella with all my heart for encouraging and supporting me to make the decision to come to Berlin and start a PhD project at the BAM.

Secondly, I have no words to express my gratitude to Prof. Heinz Sturm for offering me the opportunity to work and develop this project. He assisted and pushed me forward, especially in the most critical moments. Heinz was a very supportive supervisor at all times. In addition, our work group at BAM had the perfect harmony, and I am very thankful to my colleagues for all their incentive and appreciation.

One of the most special contributions came from Prof. Kerstin Kracht, who I admire enormously. Prof. Kracht's assistance and perseverance gave me the extra inspiration needed to conclude the project. She always believed in me, and never hesitated to make time in her extremely busy agenda to advise me. I am deeply grateful for that. Alongside, I was very lucky and honored to have on board Prof. Utz von Wagner, who encouraged me to stretch and refine my knowledge, improving substantially the content of this study.

Furthermore, the outcome of this work would not have been the same without the collaboration and determination of our partners from BAuA, Dr. Asmus Meyer-Plath and Dr. Domenic Kehren. Their expertise and technical skills were crucial to achieve the project's important milestones.

I want to thank Christiane Weimann from BAM and Ulrich Gernert from ZELMI-TU Berlin for sharing their microscopy analysis skills, which allowed me to perform experiments inside electron scanning microscopes with conviction.

Naturally, I would like to thank the financial support from BAuA, and BAM for enabling this work to be developed in its equipment and facilities.

Last but not least, the tremendous care, patience, and love of Fabian, and the cheer of my friends and family gave me focus and confidence to reach my goals.

Abstract

In the last decades, a new class of materials with outstanding properties at the nanometric scale was presented to the world along with promising advances in various areas of technology. Such materials showed great electrical and thermal conductivity, and remarkable mechanical properties. Among these nanoscale materials, the nanofibers were promptly foreseen as great reinforcement substitutes for macroscale particles in composite materials, especially where lightweight plays a decisive role. However, areas of research concerned with the impact of these materials on the environment began to shed light on the consequences of nanofibers that are released to the atmosphere at the manufacture or at the disposal phase, for example. These studies showed that free airborne biopersistent nanofibers having certain dimensional characteristics can provoke serious health issues when they reach the deep airways of the respiratory system through inhalation. Furthermore, the harm caused by biopersistent nanofibers was directly related to their flexural rigidity. Thus, knowing the mechanical behavior of these materials became crucial not only for the potential application in structural components, but also to control the spread of rigid nanofibers before the potential risks are assessed.

The presented work proposes a novel method to evaluate the flexural rigidity of nanofibers by employing a non-complex experimental setup using the Dynamic Scanning Electron Microscopy technique. In this method, the Young's modulus of cantilevered nanofibers was obtained through mechanical excitation and resonance detection experiments based on the Euler-Bernoulli beam theory. Upon deriving the Young's modulus experimentally, the flexural rigidity was calculated and discussed.

Multi-walled carbon nanotubes and silicon carbide nanowires were investigated. The results showed scattered values of Young's modulus from 15 to 161 GPa and 105 to 340 GPa, respectively. The nanotubes exhibited a curvilinear morphology, which is not exactly in accordance with the Euler-Bernoulli principle. However, it was important to examine this material since it became a benchmark for toxicological studies. For that, an alternative model to determine the Young's modulus based on the vibration of curved beams was proposed and compared to Euler-Bernoulli. In addition, the curvy shape of the nanotubes was noticed to increase uncertainties on the length measurements performed via SEM images, because it produces a projected length different from the fiber's true length. This effect can cause error deviations in average up to 59% on the Young's modulus. To minimize these errors, a parallax method to reconstruct the 3D model of the fiber based on the 2D images with different tilt angles is recommended. On the other hand, the silicon carbide nanowires were very straight, showing a vibration behavior very approximate to the theoretical values for perfect linear elastic beams, and an average error of 18.6% on the Young's modulus.

Both nanofibers showed flexural rigidity values above the critical rigidity threshold of 10^{-19} $N{\cdot}m^2$, which is the maximum permitted to prevent damages in defense cells of lungs. Therefore, these fibers were classified as potential hazard for humans. The method described is applicable to nanofibers and nanowires with known material density, exhibiting a beam-like shape and electrically conductive or semiconductive.

Zusammenfassung

In den letzten Jahrzehnten wurde der Welt eine neue Klasse von Materialien mit herausragenden Eigenschaften im nanometerbereich vorgestellt, die vielversprechende Fortschritte in verschiedenen Technologiebereichen ermöglicht. Diese Materialien weisen eine hohe elektrische und thermische Leitfähigkeit sowie bemerkenswerte mechanische Eigenschaften auf. Unter diesen nanoskaligen Materialien wurden die Nanofasern sofort als großartiger Verstärkungsersatz für makroskopische Partikel in Verbundwerkstoffen vorhergesehen, insbesondere dort, wo das Gewicht eine entscheidende Rolle spielt. Forschungsbereiche, die sich mit den Auswirkungen dieser Materialien auf die Umwelt befassen, begannen jedoch, die Folgen von Nanofasern zu beleuchten, die z. B. bei der Herstellung oder bei der Entsorgung in die Atmosphäre abgegeben werden. Diese Studien haben gezeigt, dass frei in der Luft schwebende biopersistente Nanofasern mit bestimmten Abmessungsmerkmalen ernsthafte Gesundheitsprobleme hervorrufen können, wenn sie durch Einatmen in die tiefen Atemwege gelangen. Die durch biopersistente Nanofasern verursachten Schäden standen außerdem in direktem Zusammenhang mit ihrer Biegesteifigkeit. Daher ist die Kenntnis des mechanischen Verhaltens dieser Materialien nicht nur für die potenzielle Anwendung in Strukturbauteilen von entscheidender Bedeutung, sondern auch, um die Verbreitung von starren Nanofasern zu kontrollieren, bevor die potenziellen Risiken bewertet werden.

In der vorliegenden Arbeit wird eine neuartige Methode zur Bewertung der Biegesteifigkeit von Nanofasern vorgeschlagen, bei der ein unkomplizierter Versuchsaufbau unter Verwendung der dynamischen Rasterelektronenmikroskopie-Technik verwendet wird. Bei dieser Methode wurde der Elastizitätsmodul von freitragenden Nanofasern durch mechanische Anregung und Resonanzdetektionsexperimente auf der Grundlage der Euler-Bernoulli-Theorie ermittelt. Nach der experimentellen Ableitung des Elastizitätsmoduls wurde die Biegesteifigkeit berechnet und diskutiert.

MWCNTs und SiC NWs wurden untersucht. Die Ergebnisse zeigten verstreute Werte des Elastizitätsmoduls von 15 bis 161 GPa bzw. 105 bis 340 GPa. Die CNTs wiesen eine gekrümmte Morphologie auf, die nicht genau mit dem Euler-Bernoulli-Prinzip übereinstimmt. Dennoch war es wichtig, dieses Material zu untersuchen, da es als Maßstab für toxikologische Studien diente. Die gekrümmte Form der CNTs erhöhte die Unsicherheiten bei den Längenmessungen, die mittels SEM-Bildern durchgeführt wurden. Dieser Effekt kann zu Fehlerabweichungen von durchschnittlich bis zu 59 % beim Elastizitätsmodul führen. Um diese Fehler zu minimieren, wird ein 3D-Rekonstruktionsmodell der Faser auf der Grundlage der 2D-Bilder empfohlen. Andererseits waren die SiC NWs sehr gerade und zeigten ein Schwingungsverhalten, das einem perfekten linearen elastischen Balken sehr nahe kam, und einen durchschnittlichen Fehler von 18,6 % beim Elastizitätsmodul. Beide Nanofasern wurden als potenzielle Gefahr für den Menschen eingestuft, da ihre Biegesteifigkeitswerte über der kritischen Steifigkeit von 10^{-19} $N \cdot m^2$ lagen. Die beschriebene Methode ist auf Nanofasern mit bekannter Dichte anwendbar, die eine balkenartige Form aufweisen und elektrisch leitfähig oder halbleitend sind.

Contents

List of Figures iii
List of Tables viii
List of abbreviations ix
1. Introduction 1
1.1 Motivation 1
1.2 Objective 3
1.3 Thesis Structure 3
2. Fundamentals 4
2.1 Linear Elasticity of Materials 4
2.1.1 The engineering approach 4
2.1.2 The stress-strain relationship for three dimensional isotropic materials 7
2.2 The Euler-Bernoulli Beam Theory 11
2.2.1 Flexural vibrations of a beam 11
2.3 Flexural Rigidity of a beam 18
2.4 In situ investigation of the elastic properties of nanofibers 18
2.4.1 Tests with atomic force microscopy 19
2.4.2 Tests with electron microscopy 22
2.4.3 Other techniques 27
3. Materials 28
3.1 Carbon Nanotubes 28
3.1.1 Synthesis of Carbon Nanotubes through catalytic chemical vapor deposition 30
3.1.2 Elastic behavior of MWCNTs 31
3.1.3 Multi-walled carbon nanotubes studied 34
3.2 Silicon Carbide Nanowires 35
3.2.1 Elastic properties of SiC NWs 38
3.3 Piezoelectric Actuators 39
4. Methods 41
4.1 Preparation of Free-Standing Nanofibers 41
4.1.1 Fixation of nanofibers using PEDOT:PSS polymer 41
4.1.2 Fixation of nanofibers using the focused ion beam scanning microscope 44
4.2 The Dynamic Scanning Electron Microscopy technique 46
4.2.1 Electron microscopy imaging and lock-in amplifier analysis 47

4.2.2 Estimation of resonance frequencies and Young's modulus....48
4.2.3 Error estimation....50
5. Results and Discussion....50
5.1 Fiber clamping....50
5.2 MWCNTs....53
5.2.1 Determination of the dimensions of the nanotubes....53
5.2.2 Young's modulus measurements of MWCNTs....56
5.2.3 Influence of an extra mass on the detected resonance frequencies....60
5.2.4 Characterization of the MWCNTs with transmission electron microscopy....62
5.2.5 Energy dissipation....64
5.2.6 The compatibility of the MWCNTs with the Euler-Bernoulli beam theory....68
5.2.7 Vibration of Curved Beams....69
5.2.8 Determination of the Young's modulus using the curved beams theory....75
5.3 Silicon Carbide Nanowires....76
5.3.1 Young's modulus measurements of SiC NWs....76
5.3.2 Length and diameter measurements of SiC nanowires....80
5.3.3 Error estimation for the Young's modulus of SiC NWs....83
5.3.4 Energy dissipation in the excitation tests of SiC NWs....84
5.4 Flexural rigidity of nanofibers....85
5.5 Analysis of the effect of the boundary conditions on the first natural frequencies and on the rigidity of the nanofibers studied....89
6. Remarks....97
6.1 Recalculation of the error estimation for the MWCNTs....97
6.2 Three-dimensional reconstruction of curved nanofibers....99
7. Conclusion....100
8. Research Prospects....103
9. References....104

List of Figures

Figure 1: simplified stress - strain curve for a crystallographic elastic material under tensile loading. Within the elastic region, the material can undergo loading until the yield point with no permanent deformation. From that point on, the nonelastic region starts, and an irreversible plastic deformation is formed. Image adapted from [28]. 5

Figure 2: plot of Force versus interatomic separation (***r***) for atoms with weak bonds (blue) and atoms with strong bonds (red). Interatomic distances above the values where the peak of the curve is defined are irreversible. Image extracted from [29]. 6

Figure 3: stress state of an infinitesimal part of a material showing the orthogonal and the tangential stresses. 7

Figure 4: model of an Euler-Bernoulli beam under vibration (top), and a free-body diagram of a infinitesimal element of the beam under bending forces. 11

Figure 5: resonance frequencies and mode shapes of the first four eigenmodes with the exact position of the nodes along the beam length. Image extracted from [37]. 18

Figure 6: schematic examples of force vs. displacement bending tests in an atomic force microscope. In (a), the nanowire is clamped on one side and the force applied by the cantilever tip is applied at the end of the wire; and in (b) the scheme of a doubly-clamped nanowire, where the force is applied at the center and both extremities are fixed. Image extracted from the article [40]. 20

Figure 7: Illustration of clamping techniques used in AFM to test the mechanical properties of nanowires: the image on the left shows how SiC nanowires or carbon nanotubes were pinned on a substrate by square pads [41]; the two images on the right show nanotubes suspended over a membrane to receive the vertical force exerted by the AFM cantilever tip [3, 38] 20

Figure 8: the AFM cantilever tip scans over a vertically aligned ZnO nanowire in contact mode producing a deflection on the nanowire. The images from (a) to (e) show the different stages of the bending test with the correlating lateral force recording [42] 21

Figure 9: TEM images of the experimental setup and testing of CNTs via electrostatic deflections. The upper figure shows a scheme of the electrode and counter electrode on opposite sides with an applied voltage. Below, there is a series of images of one CNT being tested: (a) at stationary mode; (b, c) at the first mode of resonance and (d) at the second mode of resonance [43]. 23

Figure 10: (a) SEM image of a MEMS with thermal actuator used to test carbon nanotubes; (b) a high magnification SEM image of a MWCNT suspended in the gap between the actuator (left side) and the load sensor of the MEMS [53]. 24

Figure 11: SEM image of a "push-to-pull" micromechanical device used to test nanowires with the view of the nanoindenter in the lower part of the image, and a close-up of the specimen under tension at the central part of the device (right) [55]. 24

Figure 12: SEM image of a molybdenum dioxide (MoO_2) nanowire being deflected by a tungsten tip and the image correlation to obtain the resulting displacement $\boldsymbol{\delta}$ [57]. 25

Figure 13: SEM images of a single MWCNTs being tested with AFM cantilevers. In (a) a lower magnification view of the two cantilevers setup and in (b) a closer look of the nanotube clamping on each tip [5]. 26

Figure 14: (a) model of the fullerene C_{60} molecular structure [70]; (b) Carbon allotropes: a fullerene on the left, a single-wall nanotube at the center, and a graphene sheet on the right. 29

Figure 15: scheme showing the three different types of carbon nanotubes according to the chirality: (a) armchair; (b) zigzag; (c) chiral; and the representation of the chiral vector on a graphene sheet (right) [71]. 29

Figure 16: Schematic model of a catalytic chemical vapor deposition process showing in (a) the tubular reactor in which the chemical processes occur and in (b) the growth mechanism of a CNT [72].....30

Figure 17: High resolution SEM images of a set of the NM-401 MWCNTs samples used in this project. The nanotubes in these images are fixed on a PEDOT:PSS film standing free on piezoelectric quartz crystal units. High resolution SEM Hitachi SU8230 from BAuA.....35

Figure 18: examples of polytypes of SiC [86].....36

Figure 19: some examples of the most common morphologies: (a) Typical nanowire, (b) hierarchical, beaded nanochains, (d) bamboo-like, (e) twin, (f) bicrystalline, (g1) SiC core-based nanocables, (g2) nanochains, (g3) SiC shell-based nanocables, (h) nanoarrays [87].....37

Figure 20: SEM images of different morphologies of SiC nanofibers observed during the qualitative analysis of the samples prepared for the resonance detection tests [89]. 38

Figure 21: a tuning fork quartz crystal unit as purchased (right) and after the removal of the metallic cover. These piezoelectric quartz units were used as actuators for the excitation of the fibers. The fibers were fixed standing free on the tip of these units, and the ones standing out on the edges could be analyzed.....40

Figure 22. A closer look of the piezo quartz unit soldered to the SMB connector (left); the complete configuration of the piezo quartz containing multi-walled carbon nanotubes: the piezo is connected to a SMB adaptor and to the vacuum chamber electric feedthrough. This setup was then fixed on an aluminum stub and mounted on the SEM stage for the experiments (right).....40

Figure 23: Examples of the piezo quartz units presenting the nanofibers at the tip (black spot). 42

Figure 24. Schematic of the electrostatic nanofiber aerosol precipitation setup: Aerosol generation chamber supplied with carrier gas (left); sedimentation chamber (center); electrostatic precipitator (right). Image extracted from the article [91].....43

Figure 25. SEM images of the configuration of the nanofibers standing free on the edges of the piezos, fixed by the PEDOT:PSS polymer film: (left column) MWCNTs used in this work, and (right column) silicon carbide nanowires tested. 43

Figure 26: sequence of FIB-SEM images showing the step-by-step of the attempt to select one single CNT to be fixed onto a piezo via Pt deposition; in the first row, a long and straight MWCNT is collected from a substrate with many others MWCNTs. The nanotube attaches to the microscopic needle though electrostatic forces; in the second row, the needle brings the nanotube to the piezo and places it in a pre-defined position, where the Pt deposition will next occur; in the third row, a block of solidified Pt is formed at the basis of the nanotube, fixing it on the piezo. Next, after the needle releases the CNT, it is possible to notice an accumulated mass of Pt from the base until the middle length of the fiber. 45

Figure 27: . Experimental setup of the dynamic scanning electron microscopy (DySEM) technique used to measure the resonance frequencies of nanofibers. 48

Figure 28. Examples of the theoretical estimations for the resonance frequency ranges of the carbon nanotubes. The color spectrum shows the range of resonance frequencies and Young's modulus ***EY*** for carbon nanotubes (CNTs) 10 μm long at: (a) first and (b) second modes; and resonance frequency ranges for CNTs with a predefined Young's modulus of 160 GPa at: (c) first and (d) second modes (d). Image extracted from the paper [91, 93]. 49

Figure 29: SEM images of a carbon fiber fixed on a solidified Field's metal film. Image (a) shows a detailed front view of the connection of the base of the fiber to the alloy, and image (b) shows a side view of the base of the fiber, where it is possible to notice the exact point at which the fiber is embedded in the film. In image (c), the carbon fiber is vibrating at the first mode of resonance. 52

Figure 30: MWCNTs type NM-401 used in this work standing on the edge of a piezo fixed by the PEDOT:PSS polymer film. 54

Figure 31. High resolution SEM images of the length determined from two different projections of the three different MWCNT: (a) the front view gives a value of 6.77 μm and (b) the side view shows a visibly higher length of 7.38 μm; (c) the front view image shows 4.56 μm of length and (d) the side view presents the same fiber with 6.21 μm of length; (e) the front view length is 5.64 μm and (f) the side view length is 5.83 μm. The SEM images were obtained at BAuA with a High resolution SEM Hitachi SU8230 and the in-image measurements were performed with the software Olympus IMS at ZELMI – TU Berlin. 55

Figure 32. SEM image of a MWCNT showing the thickness collected at four different points of the fiber for the determination of the average diameter (SEM Hitachi, SU8030). 56

Figure 33: DySEM images of two different MWCNTs under excitation, one nanotube is shown on the left column and the other on the right column; (a, d) the nanotubes are at stationary mode; (b, e) the nanotubes are vibrating at the first mode and (c, f) the nanotubes are vibrating at the second mode. 58

Figure 34: Graphs of the Young's modulus values ***E*** vs. diameter ***D*** for the NM-401 MWCNTs tested in this work. Graph (a) shows all the results presented in Table 6, and Graph (b) highlight the nanotubes that exhibited resonance at first and at second mode of vibration. 59

Figure 35: A SEM image of a MWCNT from the group of nanotubes tested, which presents a volume defect in a region proximate to a vibration node. This nanotube is vibrating at the second mode of resonance. 61

Figure 36: The red fiber represents the nanotube under excitation. The first column is at null excitation, the second column refers to the first mode and the last column to the second mode. (a) a perfect straight and uniform carbon nanotube; (b) with a spherical mass at half the length of the nanotube's body; (c) and at the tip. The simulation showed that an extra mass located at the center of the tube has a smaller impact on the resonance frequencies than a mass at the tip. Image created by Dr. Asmus Meyer-Plath from BAuA. 61

Figure 37: Graph showing the importance of the detection of further modes of vibration upon exciting nanofibers that are likely to exhibit volume defects along their length.....62

Figure 38: regular camera photographs taken through the lenses of an optical microscope showing two steps of the sample holder configuration. On the left image, the cut piezo was placed onto the TEM sample holder and on the right image, the area designated to be analyzed in the TEM is fixed with the TEM clamping tool. 63

Figure 39: Examples of bright field TEM images of MWCNTs type NM-401 used in this project; (a) shows a curved nanotube; (b), (c) and (d) show some irregularities on the morphology, such as branches and non-uniformity of diameter; (e) shows the misalignment of the multiple walls. 64

Figure 40: resonance frequency curve of a MWCNT: (left) Lorentzian fit of amplitude vs. frequency for the resonance frequency of a MWCNTs with $\boldsymbol{D}$ = 102 nm, $\boldsymbol{L}$ = 12 μm, $\boldsymbol{E1}$ = 82.1 ±16.4 and $\boldsymbol{\nu 1}$ = 651.1 kHz, where $\mathbf{Q} = \boldsymbol{\nu 1 \Delta \nu} = 85$; (right) demonstration of the quality factor derivation Applied voltage of 10 V.....66

Figure 41: simplified model of the oscillating fiber as a single-degree-of-freedom system. 67

Figure 42: curved beam geometry and coordinates. 70

Figure 43: a free-body diagram of a small element of the curved beam.....71

Figure 44: example of a post processing performed on a SEM image of MWCNT 8, where a circumference is drawn over the fiber and the radius is an approximate value obtained based on the scale bar.....75

Figure 45: Graphs of the Young's modulus values $\boldsymbol{E}$ vs. diameter $\boldsymbol{D}$ for the SiC NWs tested in this work. Graph (a) shows all the results presented in Table 9, graph (b) indicates which results belong to which type of SiC morphologies: nanowire or twinned. 78

Figure 46: DySEM images of three different SiC NWs at stationary mode (column a); vibrating at first mode (column b); and vibrating at second mode (column c). 80

Figure 47: a SEM image of a silicon carbide twinned type illustrating how the focus can be an auxiliar tool to indicate that the length measured in the observed projection is not the true length. At the fixation point, the image of the fiber is sharp, however, it becomes unsharp at the tip, signalizing that the fiber is leaning towards other planes, and that the displayed length of 11.76 μm is smaller than the real fiber length. 81

Figure 48: Diagram showing the direction of tilt of the piezo inside of the SEM chamber to evaluate the length from another perspective (for the nanowires on the right edge). 82

Figure 49: a series of SEM images showing the length measurement for a set of SiC NWs from two different perspectives: the images on the left column are at 0° piezo tilt and the images on the right column are at 60° piezo tilt.....82

Figure 50: SEM images of the measurement of the diameter of a SiC nanowires in four different points. The diameter used in the Euler-Bernoulli formula was defined as the average of the values obtained from these SEM images. This procedure was applied to all the nanowires tested (Zeiss EVO MA 10) 83

Figure 51: Lorentzian fit of amplitude vs. frequency curves and the correspondent quality factors for four SiC NWs. The letter *d* in each graph stands for the diameter of the nanowires. The disposition of the graphs in clockwise order represents the data of NWs 6, 7, 11 and 12 from Table 9 respectively. 85

Figure 52: Plot of the rigidity data of silicon carbide nanowires and multi-walled carbon nanotubes tested in this work. The rigidity data is displayed in the logarithmic scale, highlighting the rigidity threshold of 10^{-19} Nm^2. All the fibers presented are potential hazard agents during phagocytosis 87

Figure 53: Graph of the flexural rigidity of the MWCNTs tested. The nanotubes are organized according to the sequence presented in Table 6, i.e., from the thinnest to the thickest nanotube. 88

Figure 54: Graph showing the variations on the rigidity of the twelve SiC NWs tested. 88

Figure 55: image of the nanowire's fixation point covered with the deposition material at the base (left); approximate data points showing the tendency of increasing the resonance frequency with higher dimensions of clamp material, until reaching a stable resonance value (at around 780 kHz) with an optimal clamp width. Image and data extracted from [104]. 90

Figure 56: Euler-Bernoulli beam supported by a rotational spring.....90

Figure 57: plot of the characteristic equation for the result of $\boldsymbol{detA = 0}$. Graph obtained in Microsoft Excel, which has a numeric precision of 15 significant digits that may affect the accuracy of the data collected. The color sequency blue, yellow, green, red, magenta illustrates the plots of functions of $\boldsymbol{k}$ equals to $\mathbf{0}, \mathbf{1}, \mathbf{10}, \mathbf{100}, \infty$, respectively.....95

Figure 58: data showing the Young's modulus of an individual SiC nanowire (number 4 from Table 9) calculated for each boundary condition from $\boldsymbol{k = 1}$ to the fixed-free state $\boldsymbol{k} \to \infty$.....97

Figure 59: SEM images of a silicon carbide nanowire fixed at the tip of an AFM cantilever, used for the 3D reconstruction of the nanowire: (a) the sample has 0° of tilt; (b) a side view with 90° tilt. (c) 3D model of the nanowire created with the parallax method from Huang et al. [60]. .99

List of Tables

Table 1: Voigt matrix notation 8

Table 2: Previous studies of the Young's modulus of MWCNTs with different diameters, produced by the most common synthesis methods as reported by other authors. The Young's ($\boldsymbol{EY}$) and the Young's modulus ($\boldsymbol{E}$) values are approximated to the values given in the literature. "F vs. δ" stands for force-versus-deflection testing....33

Table 3: Previous results of Young's modulus of SiC NWs and the testing methods used to characterize the mechanical properties 39

Table 4: Specification of the carbon fibers Tenax®-E HTS45....51

Table 5: Experimental ($\boldsymbol{vexp}$) and theoretical ($\boldsymbol{vth}$) values of the resonance frequency measurements of one carbon fiber on a Field's metal film. The theoretical values were calculated using $\boldsymbol{\rho}$ and $\boldsymbol{E}$ from the fiber specification and the diameter ($\boldsymbol{Dexp}$) and length ($\boldsymbol{L}$) were measured during the experiment. The Young's modulus found experimentally is described as $\boldsymbol{Eexp}$. The error in the Young's modulus was calculated as 15.4%. 52

Table 6: Young's modulus of MWCNTs produced by chemical vapor deposition. $\boldsymbol{E1}$ is the Young's modulus determined from the first mode and $\boldsymbol{E2}$ is the bending determined from the second mode, according to Equation 2.63. The estimated experimental errors are ± 3 nm for $\boldsymbol{D}$, ± 200 nm for $\boldsymbol{L}$ and ± 1 kHz for $\boldsymbol{\nu 1}$ and $\boldsymbol{\nu 2}$. We neglect the inner diameter $\boldsymbol{Di}$ for its contribution is very small for the MWCNTs studied here due to the 4th power dependence in the second moment of area: $\boldsymbol{DiD4 \ll 1}$. The theoretical ratio between the non-dimensional resonance frequencies $\boldsymbol{\beta 22 \beta 12}$ equals $\boldsymbol{\nu 2 \nu 1 = 6.267}$ (see Section 2.2.1). $\boldsymbol{E}$ specifies the weighted average of $\boldsymbol{E1}$ and $\boldsymbol{E2}$. 57

Table 7: Values of resonance frequencies at first and second mode obtained from finite elements simulation for a CNT. The second column shows the frequencies of a pristine CNT; the third column presents the resonances of a CNT with an extra mass in the middle length; and the last column shows the resonances for a CNT with a mass at the tip. The percentage values refer to the frequencies of the pristine CNT. 62

Table 8: values of coefficients $\boldsymbol{A1}$ to $\boldsymbol{A4}$ to insert into Equation 5.24....74

Table 9: Young's modulus of the SiC NWs tested. *D* is the diameter of the nanowires, *L* is their length, $\boldsymbol{\nu m}$ is the resonance frequency, $\boldsymbol{E1}$ is the Young's modulus at the first mode, $\boldsymbol{E2}$ is the Young's modulus at the second mode and $\boldsymbol{E3}$ is the Young's modulus at the third mode. The estimated experimental errors are ± 3 nm for $\boldsymbol{D}$, ± 800 nm for $\boldsymbol{L}$ and ± 1 kHz for $\boldsymbol{\nu 1}$, $\boldsymbol{\nu 2}$, and $\boldsymbol{\nu 3}$. The average error for $\boldsymbol{E}$ is 18.6% and the error associated to each $\boldsymbol{E}$ is presented in Table 10. 77

Table 10: Young's modulus of SiC NWs from Table 9 with the associated error values. 83

Table 11: Young's modulus of one individual SiC nanowire calculated according to each value of the ratio $\boldsymbol{k}$, at the first mode of resonance. The error associated to $\boldsymbol{E}$ is 11.7% (Table 10). ...96

Table 12: Young's modulus of the MWCNTs from Table 6 with the updated error values....98

List of abbreviations

2D	two-dimensional
3D	three-dimensional
AFM	atomic force microscopy
BAM	Bundesanstalt für Materialforschung und -prüfung
BAuA	Bundesanstalt für Arbeitsschutz und Arbeitsmedizin
BNC	Belling-Lee connector
CCVD	catalytic chemical vapor deposition
CFCs	chlorofluorocarbons
CNTs	carbon nanotubes
CVD	chemical vapor deposition
D	diameter
DDTs	dichlorodiphenyltrichloroethane
DySEM	dynamic scanning electron microscopy
E	Young's modulus
E-B	Euler-Bernoulli
FEG	field emission gun
FIB	focused ion beam
FWHM	full width at half maximum
GPa	gigapascal
Hz	hertz
JRC	Joint Research Center
L	length
LDV	laser Doppler vibrometry
LIA	lock-in amplifier
MEMS	microelectromechanical systems
MPa	megapascal
MWCNTs	multi-walled carbon nanotubes
NAS	nanoparticle aerosol sampler
NEMS	nanoelectromechanical systems
nm	namometer

NWs	nanowires
PCB	printed circuit board
PEDOT:PSS	Poly(3,4-ethylenedioxythiophene) polystyrene sulfonate
Q	quality factor
R	flexural rigidity
R_{cr}	critical flexural rigidity
SAM	self-assembled monolayers
SDOF	single-degree-of-freedom
SEM	scanning electron microscope
SiC	silicon carbide
SMB	sub-miniature version B
TEM	transmission electron microscope
TPa	terapascal
TU	Technische Universität
V	volt
V_{ac}	Alternate current voltage
V_{dc}	Direct current voltage
VLS	vapor-liquid-solid
VS	vapor-solid
WHO	World Health Organization
ZELMI	Zentraleinrichtung Elektronenmikroskopie
ZnO	zinc oxide
σ	stress
β	non-dimensional natural frequencies
ϵ	strain
μm	micrometer

1. Introduction

1.1 Motivation

One of the greatest achievements of Materials Science has been the discovery and development of nanomaterials and the unique properties brought up by the arrangement of atoms in well-defined structures at the nanometric scale. Many nanomaterials with the shape of nanofibers such as nanotubes and nanowires present remarkable electrical and thermal conductivity characteristics, and outstanding mechanical properties. These attributes combined with their lightweight make them very promising to be used as reinforcement in composites. However, for the application as structural components, one needs to have a full knowledge of their mechanical behavior starting, for example, with their Young's modulus E and their flexural rigidity. Until the present date, the available technology capable of reaching the nanometric scale to measure the mechanical properties of materials is still limited, and there are so far no reference standards for such tests. For this reason, many researchers are working on the development of different methods to be able to describe the properties of these materials, either theoretically by using computational simulations or by experimental approaches [1]. Among the experimental procedures, techniques involving microscopy are essential since the object of analysis is of very small dimensions. The most common tests use atomic force microscopy or electron microscopy and are combined with various principles of mechanical testing like bending, uniaxial loading, nanoindentation and resonance frequencies detection.

Among the nanomaterials discovered in the last decades, one special class has been drawing considerably the attention of researchers due to its extraordinary characteristics, boosting the search for techniques to evaluate the mechanical properties of nanofibers. This class of materials are the carbon nanotubes (CNTs), which consist of carbon atoms bonded together in repeated hexagonal shapes forming a tube of a graphene sheet with very high aspect ratio. Such microstructures provide this material with many important properties like great electrical and thermal conductivity and a tensile strength even higher than that of steel. Some researchers tested the mechanical properties of MWCNTs and found values from 0.1 to 1.28 TPa for its Young's modulus [2-11]. Such high modulus and other promising properties led many research institutions to support projects involving the investigation of new techniques to synthesize nanotubes in a more optimized way and to deepen the knowledge about its behavior. An example of that was seen in 2000, when the US government raised the National Nanotechnology Initiative to investigate primarily CNTs and it has invested almost $29 billion in nanotechnology-related research over the last twenty years.

Parallel to the increase of projects aiming at better understanding the properties and behavior of carbon nanotubes and the possible applications for them, many researchers from health and environment areas began to shed light on the potential risks brought up by the direct contact of these nanofibers with humans. In 2002, Gorman published a work highlighting the needs for further studies concerning the impacts of new materials in the health and environment before they were established as an industrial product. In her work, she refers

to the wide usage of harmful chemicals discovered in the 20th century, like chlorofluorocarbons and dichlorodiphenyltrichloroethane (CFCs and DDTs, respectively), which were later withdrawn from the market after the confirmation of serious damages to the atmosphere and to the human health [12]. Similarly happened with asbestos fibers that, after being extensively used in many applications were found to cause lungs cancer upon inhalation [13]. These fibers have chemical characteristics of a durable fiber, meaning that human cells are not able to decompose them to absorb their constituent parts. The biopersistence aspect combined with a length higher than 20 μm, a thickness under 3 μm and the aspect ratio above 3 make these materials particularly pathogenic [14, 15]. Even if the stiffness is not taken into consideration (asbestos' Young's modulus ~ 165 GPa [16]). Based on studies concerning pathogenic fibers, the World Health Organization (WHO) defined that potentially rigid and biopersistent fibers with length > 5 μm, thickness < 3 μm and aspect ratio > 3 may pose harm to lungs [17].

Considering its very small dimensions, nanomaterials can easily be carried away in different mediums until it reaches the body of humans or animals without being noticed. If it reaches groundwater, it can be incorporated into the food chain, or if it stays on the air, it can be inhaled. For being very lightweight, resistant, and having the characteristics of a fine powder, CNTs can be released into the air during production, use or disposal. During manufacture and handling, CNTs may undergo some mechanical processes like powder milling, agitation, and pulverization, which increase the chances of fine particles to become airborne respirable dust leading to occupational hazards. To avoid that workers involved in these processes are not exposed to contamination risks, production facilities with modern and advanced hygiene standards are required. And consequently, the costs of production tend to be higher [18]. CNTs have become commercially available and started to be used in large scale in distinct types of products, but there is still the question of how this material behaves upon abrasion and deterioration and if it breaks contact with its original matrix, would it be released into the atmosphere joining pollution? The same concept can be applied for general waste containing these and other nanofibers. Without the proper selective disposal, these particles can be dispersed into the air and water and return to human or nature contact [19, 20].

With so many signs that carbon nanotubes may pose risks for humans and for the environment as airborne particles, many researchers started to investigate the effects of CNTs in contact with the main parts of the respiratory system and the parameters involved in their pathogenicity. The conclusion from these studies was that rigid and long carbon nanotubes cause indeed strong inflammation in defense cells (macrophages) and necrosis in the lungs of mice, possibly leading to cancer, but no significant inflammation was observed for short nor flexible and tangled carbon nanotubes. Furthermore, the harm that CNTs provoke in macrophages was associated with their bending response and with their flexural rigidity, being denominated as "frustrated phagocytosis" [13, 21-25].

Carbon nanotubes and other nanofibers are very promising materials, that can bring significant progress to science and technology, and it would be a throwback not to incorporate these materials into the industry and society. On the other hand, these materials may be harmful to humans, depending on how rigid they are and how they are handled. Therefore, knowing accurately the mechanical properties of nanomaterials is beneficial not only for the

application in all suitable and possible ways, but also to prevent that some advances in the Materials Science jeopardize the health of people and the environment.

1.2 Objective

This work was carried out in the Bundesanstalt für Materialforschung und -prüfung (BAM Berlin) in cooperation with the Bundesanstalt für Arbeitsschutz und Arbeitsmedizin (BAuA Berlin), with the aim to develop a routinely applicable method to investigate the rigidity of nanofibers. To achieve this, the resonance frequencies of commercial multi-walled carbon nanotubes (MWCNTs) and silicon carbide nanowires (SiC NWs) were experimentally detected using the Dynamic Scanning Electron Microscopy [DySEM] technique [26, 27]. To evaluate the stiffness of the nanofibers, the corresponding Young's modulus were obtained by applying the Euler-Bernoulli beam theory, followed by the calculation of the flexural rigidity. For the testing setup, the fibers were fixed standing free on the edges of a piezoelectric quartz crystal drive through which mechanical excitation was transmitted. Critical points of this project were the measurement of the fiber's dimensions, the shape compatibility of the MWCNTs with the Euler-Bernoulli theory, and the effect of the fiber clamping on the boundary conditions. The method proposed can be implemented for nanofibers and nanowires that present a beam-like shape, have known density, and are electrically conductive or semi-conductive. The term "nanofibers" refers to all types of nanomaterials with a fiber-like morphology, such as nanowires and nanotubes.

The study presented here is a continuation of the master thesis "Mechanische Eigenschaften Nanoskaliger Fasern" of Jan Troeltsch, concluded in 2014 . Most of the project's activities took place in the laboratories of the BAM, however in the initial phase, microscopy analysis and a few experiments were carried out in the Zentraleinrichtung Elektronenmikroskopie at the Technische Universität Berlin (ZELMI TU Berlin), and at BAuA.

1.3 Thesis Structure

The next chapter comprises the fundamentals regarding the linear elasticity of materials, the introduction to the Euler-Bernoulli beam theory, and a state of the art of the testing techniques used to study the elastic properties of nanofibers. Chapter 3 and 4 describe the main materials used in the project, the procedures employed in the sample preparation step to fix cantilevered nanofibers, and how the DySEM technique is applied to detect the resonance frequencies of nanofibers. The chapter 5 contains the results of the excitation tests performed with the MWCNTs and the SiC NWs, the discussions about the critical aspects of the method, the acquisition of the flexural rigidity of the nanofibers, and an evaluation of the boundary conditions impact on the first natural frequencies. In chapter 6, additional analysis on certain aspects of the method formulation are provided, such as the effect of the boundary conditions on the natural frequencies. The chapter 7 summarizes the results obtained in this project and recalls the toxicology perspective of rigid nanofibers. Finally, chapter 8 presents key points of this method that could potentially be improved in further studies.

2. Fundamentals

2.1 Linear Elasticity of Materials

2.1.1 The engineering approach

In all kinds of structural applications, a component is designed to respond to a specific level of stress within its elastic regime, where deformation is reversible. Contrary to the elastic regime, the plastic regime is avoided since any permanent modification of its shape or microstructure might start a series of unpredictable and undesirable behaviors, leading to failure. In this way, to build safe engineering structures and components subjected to unidirectional loading, one of the first technical limiting parameters to be verified is the Young's modulus of materials and the related yield strength. For this reason, the majority of works related to the mechanical properties of nanofibers and nanomaterials in general involves an investigation of their elastic properties. In addition, this coefficient represents a response in the macroscopic scale of the amount of energy required to move the atoms constitutive of the material apart without breaking their chemical bonds. In this sense, the elastic modulus is a very reliable coefficient that express the resistance of materials from an atomic scale to the conduct in the bulky form.

Most of the crystallographic engineering materials present an elastic linear regime during the initial phase of loading, and a subsequent plastic regime. This means that when a component is subjected to a force, it starts to deform presenting a linear strain rate with the increase of the load applied. In practice, there is also the onset of a non-linear elastic regime shortly before plasticity starts. Once the load is removed, the material returns to its original form. Upon increase of the load beyond the elastic phase, the material reaches the yield point, from which the deformation becomes plastic and the strain rate changes to a nonlinear regime. This nonlinearity is a consequence of deformation mechanisms that take place at the microscopic scale, such as dislocations in metals. At the plastic phase, the deformation is permanent, and it ceases when at a higher load the material fails, leading to fracture. This behavior of materials under axial stress is represented by the stress-strain curve. In some cases, the exact point at which the material starts to yield may not be clearly seen in the stress-strain curve. For this reason, a convention was adopted in which the yield stress is obtained through a straight line drawn parallel to the elastic phase graph, positioned at an offset of 0.002 on the strain axis. The intersection of this offset line with the stress-strain curve gives the engineering yield stress value. Figure 1 shows a typical engineering stress-strain curve that represents the behavior of a crystallographic material under tensile testing. The relationship between stress (σ) and strain (ϵ) during the elastic regime of materials under tensile loading is described by Hooke's law (Equation 2.1). The Young's modulus or modulus of elasticity (E) is the parameter used to quantify the elasticity, or the stiffness of materials and it is obtained from the slope of the linear section of the plot of stress versus strain of a material submitted to a tensile test.

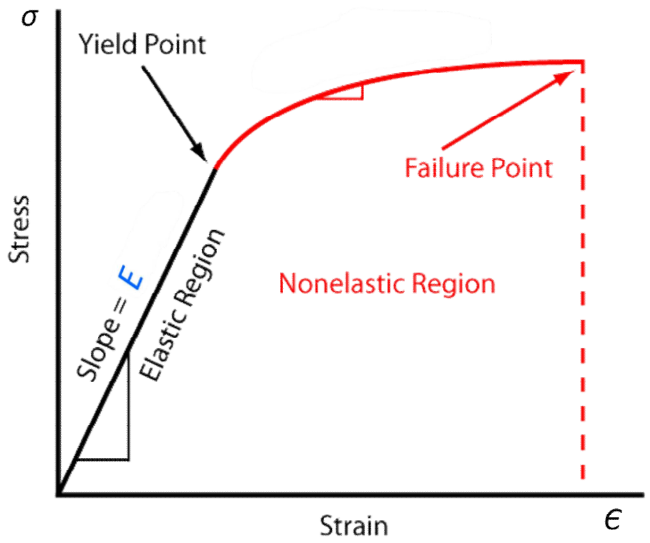

Figure 1: simplified stress - strain curve for a crystallographic elastic material under tensile loading. Within the elastic region, the material can undergo loading until the yield point with no permanent deformation. From that point on, the nonelastic region starts, and an irreversible plastic deformation is formed. Image adapted from [28].

$$\sigma = E\epsilon \tag{2.1}$$

The macroscopic elastic response of a material under loading is displayed at the atomic scale by the variation of the distance between atoms. In other words, when the material is subjected to a force below the yield point, the atomic bonds are being stretched and the atoms are moving apart from one another, without breaking the bonds apart. Or, in the case of compressive loading, the atoms are being brought together to a minimum permissible distance to each other. When the load is released, the atoms return to their original equilibrium state and the deformation disappears. Here, it is clear that the modulus of elasticity E is directly proportional to the forces of attraction and repulsion between the atoms, which is represented by the slope of the force (F) versus interatomic separation plot at the equilibrium distance r_0 (Figure 2) and it is represented by the following equation:

$$E \propto \left(\frac{dF}{dr}\right)_{r_0} \tag{2.2}$$

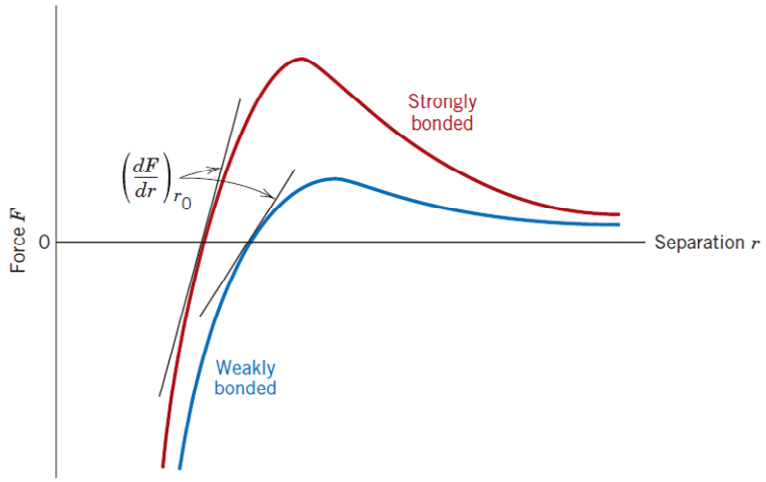

Figure 2: plot of Force versus interatomic separation (r) for atoms with weak bonds (blue) and atoms with strong bonds (red). Interatomic distances above the values where the peak of the curve is defined are irreversible. Image extracted from [29].

When low levels of load are applied generating shear stresses, the material presents an elastic response similar to the behavior under tensile loading, which can be described by the equation

$$\tau = G\gamma \tag{2.3}$$

where τ is the shear stress, G is the shear modulus and γ is the shear angle. Similar to the Young's modulus, the shear modulus is obtained from the slope of the linear elastic region of the shear stress-strain curve.

During a tensile test for an isotropic material, while an elastic elongation and strain occur in the direction of the applied stresses, a shrinkage of the specimen perpendicular to the direction of loading takes place. From this contraction, the compressive strains can be accounted and the Poisson's ratio ν can be derived. Considering that the load is applied in the z direction and ϵ_z is the corresponding strain, the lateral strains ϵ_x and ϵ_y will be equal and from opposite signs, according to the relation

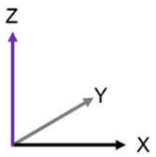

$$\nu = -\frac{\epsilon_x}{\epsilon_z} = -\frac{\epsilon_y}{\epsilon_z} \tag{2.4}$$

Furthermore, for isotropic elastic materials the shear and elastic moduli are related to the Poisson's ratio as follows

$$E = 2G(1 + \nu) \tag{2.5}$$

For materials that are anisotropic, the characterization of their elastic properties will require more than two elastic constants, depending on how the change of the crystal orientation affects their response. For the fact that most of the engineering materials are isotropic, the analysis of the stresses and strain in three-dimensional state is very often formulated considering isotropic conditions.

2.1.2 The stress-strain relationship for three dimensional isotropic materials

In a deeper analysis of a continuous three-dimensional material based on the references [30-32] , external forces f acting on its surfaces generate the stresses that can be measured by analyzing the physical state on an infinitesimal part of the whole volume, which is represented in Figure 3 .

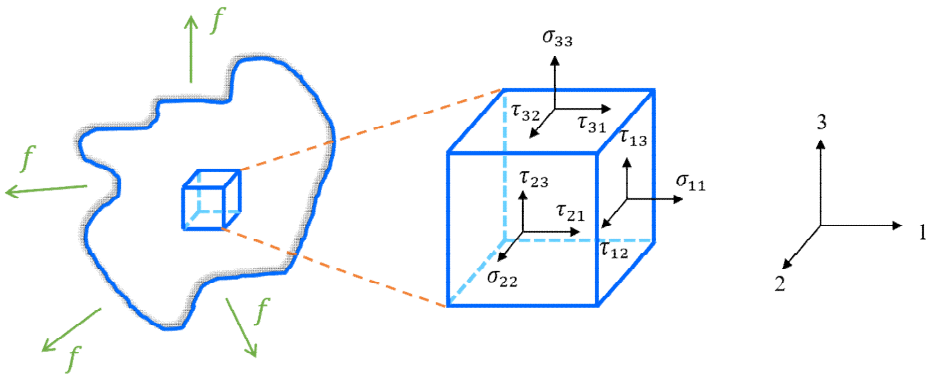

Figure 3: stress state of an infinitesimal part of a material showing the orthogonal and the tangential stresses.

The effect of the stress and the strain on the region around the point of application of the force is represented by the stress tensor $\boldsymbol{\sigma_{ij}}$ and the strain tensor $\boldsymbol{\varepsilon_{ij}}$ (Equation 2.6).

$$\boldsymbol{\sigma_{ij}} = \begin{pmatrix} \sigma_{11} & \tau_{12} & \tau_{13} \\ \tau_{21} & \sigma_{22} & \tau_{23} \\ \tau_{31} & \tau_{32} & \sigma_{33} \end{pmatrix} \qquad \boldsymbol{\varepsilon_{ij}} = \begin{pmatrix} \varepsilon_{11} & \varepsilon_{12y} & \varepsilon_{13} \\ \varepsilon_{21} & \varepsilon_{22} & \varepsilon_{23} \\ \varepsilon_{31} & \varepsilon_{32} & \varepsilon_{33} \end{pmatrix} \tag{2.6}$$

where σ_{ij} are the normal stresses and τ_{ij} are the shear stresses.

Thus, considering a material with a linear elastic response, the Hooke's Law presented in Equation 2.1 can be rewritten as

$$\boldsymbol{\sigma_{ij}} = \boldsymbol{C_{ijkl}\varepsilon_{kl}} \tag{2.7}$$

where $\boldsymbol{C_{ijkl}}$ is the elastic or stiffness tensor. Since $\boldsymbol{\sigma_{ij}}$ and $\boldsymbol{\varepsilon_{ij}}$ are second-order tensors, $\boldsymbol{C_{ijkl}}$ is a fourth-order tensor with 81 terms. For symmetric conditions, $\boldsymbol{\sigma_{ij}} = \boldsymbol{\sigma_{ji}}$, $\boldsymbol{\varepsilon_{ij}} = \boldsymbol{\varepsilon_{ji}}$, and $\boldsymbol{C_{ijkl}} = \boldsymbol{C_{jikl}} = \boldsymbol{C_{ijlk}} = \boldsymbol{C_{jikl}}$, and the number of terms of the elastic tensor reduces from 81 to 36, which is the general form of the stress-strain relation for anisotropic materials. Furthermore, using Voigt notation, the stiffness tensor can be simplified to the matrix notation by replacing ij or kl by a or b, where $i, j, k, l = 1,2,3$ and $a, b = 1,2,3,4,5,6$, according to Table 1.

Table 1: Voigt matrix notation

ij or kl	$\boldsymbol{a}$ or $\boldsymbol{b}$
11	1
22	2
33	3
23 or **32**	4
31 or **13**	5
12 or **21**	6

With Voigt notation, Equation 2.7 can be rewritten in detail as follows:

$$\begin{aligned}\sigma_{ij} = {} & C_{ij11}\varepsilon_{11} + C_{ij12}\varepsilon_{12} + C_{ij13}\varepsilon_{13} \\ & + C_{ij21}\varepsilon_{21} + C_{ij22}\varepsilon_{22} + C_{ij23}\varepsilon_{23} \\ & + C_{ij31}\varepsilon_{31} + C_{ij32}\varepsilon_{32} + C_{ij33}\varepsilon_{33}\end{aligned} \qquad i, j = 1,2,3 \tag{2.8}$$

As stated before, $\boldsymbol{\varepsilon_{ij}} = \boldsymbol{\varepsilon_{ji}}$, and $\boldsymbol{C_{ijkl}} = \boldsymbol{C_{jikl}} = \boldsymbol{C_{ijlk}} = \boldsymbol{C_{jikl}}$, for symmetric conditions, thus Equation 2.8 can be rearranged as

$$\sigma_{ij} = C_{ij11}\varepsilon_{11} + C_{ij22}\varepsilon_{22} + C_{ij33}\varepsilon_{33} + 2C_{ij23}\varepsilon_{23} + 2C_{ij31}\varepsilon_{31} + 2C_{ij12}\varepsilon_{12} \qquad i, j = 1,2,3 \tag{2.9}$$

Now, applying Voigt notation as well, the above equation can be expressed in matrix form as

$$\begin{bmatrix}\sigma_{11}\\ \sigma_{22}\\ \sigma_{33}\\ \tau_{23}\\ \tau_{31}\\ \tau_{12}\end{bmatrix} = \begin{bmatrix}C_{11} & C_{12} & C_{13} & C_{14} & C_{15} & C_{16}\\ C_{12} & C_{22} & C_{23} & C_{24} & C_{25} & C_{26}\\ C_{13} & C_{23} & C_{33} & C_{34} & C_{35} & C_{36}\\ C_{14} & C_{24} & C_{34} & C_{44} & C_{45} & C_{46}\\ C_{15} & C_{25} & C_{35} & C_{45} & C_{55} & C_{56}\\ C_{16} & C_{26} & C_{36} & C_{46} & C_{56} & C_{66}\end{bmatrix}\begin{bmatrix}\varepsilon_{11}\\ \varepsilon_{22}\\ \varepsilon_{33}\\ 2\varepsilon_{23}\\ 2\varepsilon_{31}\\ 2\varepsilon_{12}\end{bmatrix} \tag{2.10}$$

which can be simplified as

$$\begin{bmatrix}\sigma_{11}\\ \sigma_{22}\\ \sigma_{33}\\ \tau_{23}\\ \tau_{31}\\ \tau_{12}\end{bmatrix} = \begin{bmatrix}C_{11} & C_{12} & C_{13} & C_{14} & C_{15} & C_{16}\\ & C_{22} & C_{23} & C_{24} & C_{25} & C_{26}\\ & & C_{33} & C_{34} & C_{35} & C_{36}\\ & & & C_{44} & C_{45} & C_{46}\\ & sym. & & & C_{55} & C_{56}\\ & & & & & C_{66}\end{bmatrix}\begin{bmatrix}\varepsilon_{11}\\ \varepsilon_{22}\\ \varepsilon_{33}\\ 2\varepsilon_{23}\\ 2\varepsilon_{31}\\ 2\varepsilon_{12}\end{bmatrix} \tag{2.11}$$

An additional representation of the stiffness tensor for isotropic materials is using the Kronecker delta δ_{ij} and the *Lamé constants*, λ and μ, as follows:

$$C_{ijkl} = \lambda\delta_{ij}\delta_{kl} + \mu\left(\delta_{ik}\delta_{jl} + \delta_{il}\delta_{jk}\right) \tag{2.12}$$

The Kronecker delta is defined as 0 for $i \neq j$ and 1 for $i = j$; being $i, j = 1,2,3$. The *Lamé constants* are material constants related directly to the Young's modulus and the shear modulus, as given

$$\lambda = \frac{\nu E}{(1+\nu)(1-2\nu)}, \qquad \mu = G = \frac{E}{2(1+\nu)}, \qquad \nu = \frac{\lambda}{2(\lambda+\mu)} \tag{2.13}$$

Consequently, the stress-strain relationship can be expressed in terms of the *Lamé constants*, as well:

$$\sigma_{11} = \lambda(\varepsilon_{11} + \varepsilon_{22} + \varepsilon_{33}) + 2\mu\varepsilon_{11} \tag{2.14}$$

$$\sigma_{22} = \lambda(\varepsilon_{11} + \varepsilon_{22} + \varepsilon_{33}) + 2\mu\varepsilon_{22} \tag{2.15}$$

$$\sigma_{33} = \lambda(\varepsilon_{11} + \varepsilon_{22} + \varepsilon_{33}) + 2\mu\varepsilon_{33} \tag{2.16}$$

$$\tau_{23} = 2\mu\varepsilon_{23} = \mu\gamma_{23} \tag{2.17}$$

$$\tau_{13} = 2\mu\varepsilon_{13} = \mu\gamma_{13} \tag{2.18}$$

$$\tau_{12} = 2\mu\varepsilon_{12} = \mu\gamma_{12} \tag{2.19}$$

And the corresponding stiffness matrix $\boldsymbol{C}$ is

$$\boldsymbol{C} = \begin{bmatrix} \lambda+2\mu & \lambda & \lambda & 0 & 0 & 0 \\ & \lambda+2\mu & \lambda & 0 & 0 & 0 \\ & & \lambda+2\mu & 0 & 0 & 0 \\ & & & \mu & 0 & 0 \\ & sym. & & & \mu & 0 \\ & & & & & \mu \end{bmatrix} \tag{2.20}$$

In the same way, the strain-stress relation can be expressed by

$$\boldsymbol{\varepsilon} = \boldsymbol{S}\boldsymbol{\sigma} \tag{2.21}$$

where $\boldsymbol{S}$ is the compliance matrix and $\boldsymbol{S} = \boldsymbol{C}^{-1}$. Therefore, the matrix representation of $\boldsymbol{S}$ for isometric materials is

$$\boldsymbol{S} = \begin{bmatrix} 1/E & -\nu/E & -\nu/E & 0 & 0 & 0 \\ & 1/E & -\nu/E & 0 & 0 & 0 \\ & & 1/E & 0 & 0 & 0 \\ & & & 2(1+\nu)/E & 0 & 0 \\ & sym. & & & 2(1+\nu)/E & 0 \\ & & & & & 2(1+\nu)/E \end{bmatrix} \tag{2.22}$$

Finally, it has been demonstrated that, for uniform materials whose properties are the same independently of the orientation and yet present linear elastic behavior, the stress-strain relationship is defined in terms of the two elastic constants, Young's modulus E and the Shear modulus G.

2.2 The Euler-Bernoulli Beam Theory

The Euler-Bernoulli beam theory, also known as classical beam theory, describes the elastic behavior of a static or a dynamic beam submitted to axial forces and bending. In an excited beam, the corresponding stresses and displacements may be dependent on the applied force function. Furthermore, in the case of free vibrations, two important parameters of the system are the natural frequencies and the corresponding mode shapes, which relate directly to the Young's modulus of materials, as will be presented next. If the frequency of excitation matches a natural frequency, large vibration amplitudes result (resonance).

This theory considers the type of material (Young's modulus, density), the deformation pattern of the beam (nodes of vibration), the geometry of the beam and its internal equilibrium. In systems where a material is being subjected to flexural deformations as a result of forces that produce bending, the inner arc experiences compressive stresses while the outer arc experiences tensile stresses. In this case the stress-strain relationship in the linear elastic region is similar to the case of axial forces.

2.2.1 Flexural vibrations of a beam

To represent the forces acting on a beam vibrating under bending, let's first consider a beam with a rectangular cross-section $A(x)$, with height h_z, thickness t_y, and length l [33]:

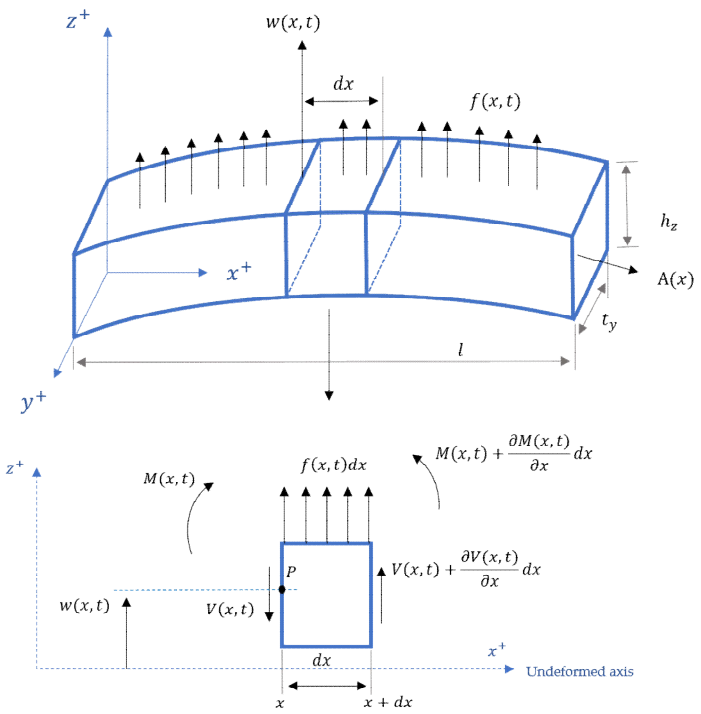

Figure 4: model of an Euler-Bernoulli beam under vibration (top), and a free-body diagram of a infinitesimal element of the beam under bending forces.

Where $f(x,t)$ and $w(x,t)$ are respectively the transverse force and the transverse displacement (or bending displacement) of the beam in space and time, $V(x,t)$ is the shear force and $M(x,t)$ is the bending moment, which is described in detail in section 9.3 of reference [34] and is defined by the relation:

$$M\,(x,t) = EI_x \frac{\partial^2 w(x,t)}{\partial x^2} \tag{2.23}$$

The product of the Young's modulus E and the cross-sectional area moment of inertia I_x about the y axis represent the flexural rigidity of the beam, and the second derivative of $w(x,t)$ represents the rate of variation of the displacement with the change in the position x.

According to Newton's Second Law the sum of the forces acting on the direction of the z axis is equal to mass times acceleration, which yields :

$$\left(V(x,t) + \frac{\partial V(x,t)}{\partial x}\,dx\right) - V(x,t) + f(x,t)dx = \rho A_x dx\,\frac{\partial^2 w(x,t)}{\partial t^2} \tag{2.24}$$

where $V(x,t)$ is the shear force, and the term on the right side of the equation is the inertial force of the element. The product ρA_x is the linear density of the beam. For beams where $l/h_y \geq 10$ and $l/t_z \geq 10$, or with an aspect ratio it can be assumed that the shear deformation is much smaller than the transversal deformation $w(x,t)$, meaning that there is no bending on the sides of the element dx.

Next, the summation of the moments on dx about the point P is described as

$$\left(M(x,t) + \frac{\partial M(x,t)}{\partial x}\,dx\right) - M(x,t) + \left[V(x,t) + \frac{\partial V(x,t)}{\partial x}dx\right]dx + [f(x,t)dx]\frac{dx}{2} = 0 \tag{2.25}$$

that can be simplified as

$$\left[\frac{\partial M(x,t)}{\partial x} + V(x,t)\right]dx + \left[\frac{\partial V(x,t)}{\partial x} + \frac{f(x,t)}{2}\right](dx^2) = 0 \tag{2.26}$$

As dx is infinitesimal small, the term dx^2 can be approximate to zero, thus

$$V(x,t) = -\frac{\partial M(x,t)}{\partial x} \tag{2.27}$$

and replacing this expression in Equation (2.24) yields

$$-\frac{\partial M(x,t)}{\partial x}-\frac{\partial\left(\frac{\partial M(x,t)}{\partial x}\right)}{\partial x}dx+\frac{\partial M(x,t)}{\partial x}+f(x,t)dx=\rho A(x)dx\frac{\partial^2 w(x,t)}{\partial t^2} \tag{2.28}$$

$$-\frac{\partial^2 M(x,t)}{\partial x^2}dx+f(x,t)dx=\rho A(x)dx\frac{\partial^2 w(x,t)}{\partial t^2} \tag{2.29}$$

$$f(x,t)=\rho A(x)\frac{\partial^2 w(x,t)}{\partial t^2}+\frac{\partial^2 M(x,t)}{\partial x^2} \tag{2.30}$$

Now, replacing Equation 2.23 into Equation 2.30:

$$f(x,t)=\rho A(x)\frac{\partial^2 w(x,t)}{\partial t^2}+\frac{\partial^2}{\partial x^2}\left[EI(x)\frac{\partial^2 w(x,t)}{\partial x^2}\right] \tag{2.31}$$

which for a uniform and homogeneous beam, the equation of motion results in

$$EI\frac{\partial^4 w(x,t)}{\partial x^4}+\rho A\frac{\partial^2 w(x,t)}{\partial t^2}=f(x,t) \tag{2.32}$$

For a free vibration beam, $f(x,t)=0$, and Equation 2.32 can be rewritten as

$$c^2\frac{\partial^4 w(x,t)}{\partial x^4}+\frac{\partial^2 w(x,t)}{\partial t^2}=0 \tag{2.33}$$

where

$$c=\sqrt{\frac{EI}{\rho A}} \tag{2.34}$$

The equation of motion (Equation 2.32) contains a fourth-order derivative with respect to x and a second-order derivative with respect to time. Thus, to calculate the solution for $w(x,t)$, beside the four boundary conditions, two initial conditions, one for the lateral displacement ($w_0(x)$) and one for the velocity ($\dot{w}_0(x)$) are specified at $t = 0$:

$$w(x, t = 0) = w_0(x) \qquad \frac{\partial w(x, t = 0)}{\partial t} = \dot{w}_0(x) \tag{2.35}$$

The boundary conditions to solve the equation with respect to x in a separation of variables solution are described by analyzing the following parameters at each end of the beam:

the deflection $$w(x,t) \tag{2.36}$$

the slope of the deflection $$\frac{\partial w(x,t)}{\partial x} \tag{2.37}$$

the bending moment $$\frac{EI\partial^2 w(x,t)}{\partial x^2} \tag{2.38}$$

and the shear force $$\frac{\partial}{\partial x}\left(EI\frac{\partial^2 w(x,t)}{\partial x^2}\right) \tag{2.39}$$

For a cantilevered beam (clamped-free), the deflection and the slope are unrestricted at the free end, but the bending moment and the shear force are null:

$$EI\frac{\partial^2 w}{\partial x^2} = 0 \tag{2.40}$$

$$\frac{\partial}{\partial x}\left[EI\frac{\partial^2 w}{\partial x^2}\right] = 0 \tag{2.41}$$

Additionally,

$$w(0,t) = 0 \qquad \frac{\partial w(0,t)}{\partial x} = 0 \tag{2.42}$$

Separating the variables and substituting in (2.33) leads to:

$$w(x,t) = X(x)\,T(t) \tag{2.43}$$

$$\frac{c^2}{X(x)}\frac{d^4X(x)}{dx^4} = -\frac{1}{T(t)}\frac{d^2T(t)}{dt^2} = \omega^2 \tag{2.44}$$

where $a = \omega^2$ is a positive constant. Equation (2.44) can be simplified into two equations:

$$\frac{d^4X(x)}{dx^4} - \beta^4 X(x) = 0 \tag{2.45}$$

$$\frac{d^2T(t)}{dt^2} + \omega^2 T(t) = 0 \tag{2.46}$$

where

$$\beta^4 = \frac{\omega^2}{c^2} = \frac{\rho A \omega^2}{EI} \tag{2.47}$$

The solution of Equation (2.46) follows:

$$T(t) = A\cos\omega t + B\sin\omega t \tag{2.48}$$

where A and B are constants from the initial conditions. For the solution of Equation (2.45), it's assumed that:

$$X(x) = Ce^{sx} \tag{2.49}$$

where C and s are constants and

$$s^4 + \beta^4 = 0 \tag{2.50}$$

$$s_{1,2} = \pm\beta, \qquad s_{3,4} = \pm i\beta \tag{2.51}$$

Thus, the solution of Equation (2.45) becomes

$$X(x) = C_1 e^{\beta x} + C_2 e^{-\beta x} + C_3 e^{i\beta x} + C_4 e^{-i\beta x} \tag{2.52}$$

where C_1, C_2, C_3 and C_4 are different constants. The equation above can also be expressed as:

$$X(x) = C_1 \cos\beta x + C_2 \sin\beta x + C_3 \cosh\beta x + C_4 \sinh\beta x \tag{2.53}$$

or

$$\begin{aligned} X(x) = C_1 (\cos\beta x + \cosh\beta x) + C_2(\cos\beta x - \cosh\beta x) + C_3(\sin\beta x + \sinh\beta x) \\ + C_4(\sin\beta x - \sinh\beta x) \end{aligned} \tag{2.54}$$

The function $X(x)$ is the *mode shape* or *characteristic function* of the beam and C_1, C_2, C_3 and C_4 are constants that can be found from the boundary conditions. For a fixed-free beam, the boundary conditions are:

$$X_n(x) = C_n[\sin\beta_n x - \sinh\beta_n x - \alpha_n(\cos\beta_n x - \cosh\beta_n x)] \tag{2.55}$$

where

$$\alpha_n = \left(\frac{\sin\beta_n l + \sinh\beta_n l}{\cos\beta_n l + \cosh\beta_n l}\right) \tag{2.56}$$

and

$$\cos\beta_n l \cdot \cosh\beta_n l = -1 \tag{2.57}$$

Further, the equation of the *natural frequency of vibration* of the beam is ω and can be derived from Equation 2.47:

$$\omega = \beta^2 \sqrt{\frac{EI}{\rho A}} = (\beta l)^2 \sqrt{\frac{EI}{\rho A l^4}} \tag{2.58}$$

and $\omega = 2\pi\nu$. Thus, for the flexural natural frequencies of cantilever beams with a free end, Equation (2.58) can be generally written as:

$$\nu_m = \frac{(\beta_m l)^2}{2\pi} \sqrt{\frac{EI}{\rho A l^4}} \tag{2.59}$$

The Equation (2.57) has infinitely many solutions, from which the Euler-Bernoulli coefficients $k_m := \beta_m l$ of the individual eigenmodes m are derived. For a free end cantilevered beam, the first four coefficients are $k_1 = 1.8751$, $k_2 = 4.6941$, $k_3 = 7.8547$, $k_4 = 10.9956$ [35].

The nanofibers studied here have a cylindrical shape with inner diameter D_i and outer diameter D (in the case of the nanotubes), or only an outer diameter D (for the nanowires). Thus, the cross-sectional area moment of inertia I and the cross-sectional area A are described as [36]:

$$I = \frac{\pi}{64}\left(D^4 - D_i^4\right) \xrightarrow{D \gg D_i} I \approx \frac{\pi}{64} D^4 \tag{2.60}$$

$$A = \frac{\pi D^2}{4} \tag{2.61}$$

Thus, from Equation (2.59) the natural frequencies of cantilevered nanofibers can be defined as:

$$\nu_m = \frac{k_m^2}{8\pi l^2} D \sqrt{\frac{E}{\rho}} \qquad (m = 1, 2, \dots) \tag{2.62}$$

where l is the length of the nanofiber from the fixation point to its tip, E is the Young's modulus. Figure 5 illustrates the natural frequencies and the mode shapes for the first four eigenmodes.

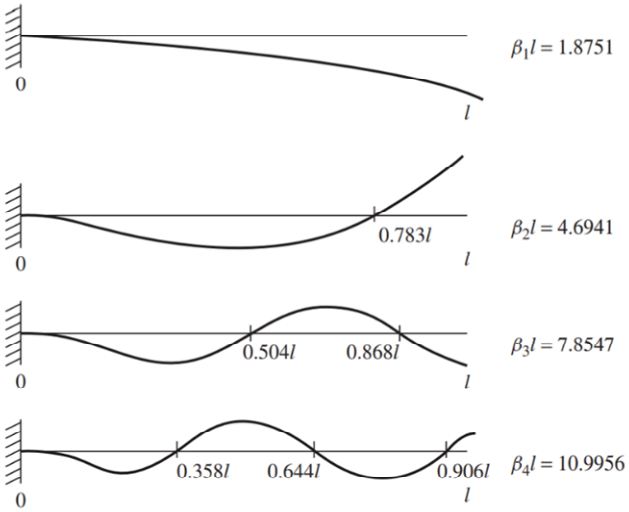

Figure 5: resonance frequencies and mode shapes of the first four eigenmodes with the exact position of the nodes along the beam length. Image extracted from [37].

To obtain the Young's modulus E, the equation 2.62 can be written as:

$$E = \frac{64\pi^2}{\beta_m^4} \cdot \frac{l^4 \, \rho \, v_m^2}{D^2} \qquad (m = 1, 2, \dots) \tag{2.63}$$

2.3 Flexural Rigidity of a beam

Physically, the flexural rigidity R of a fiber is defined as the product of Young's modulus E and second moment of axial area I [36]:

$$R = E \cdot I \tag{2.64}$$

and the cross-sectional area moment of inertia for a beam with the shape of a cylinder is $\frac{\pi}{64} D^4$ (Equation 2.60). Thus, Equation 2.64 can be written as:

$$R = E \cdot \frac{\pi}{64} D^4 \tag{2.65}$$

2.4 In situ investigation of the elastic properties of nanofibers

Having the dimensions in the nanometric scale makes it a challenge for researchers to measure the elastic behavior of nanomaterials in the same way that it is made with the bulky

counterpart, due to the limitations in manipulating such small samples. In addition, the physics prevailing in the nanoworld not always is the same as the one governing the materials at the macroscopic scale, making the results in some cases unpredictable or very complex to assess. Thus, to help predicting the behavior of materials where the eyes and the technology cannot yet reach, the scientific community has been applying the principles of mechanics of materials to test nanofibers with the aid of several microscopy techniques and advanced scientific instruments, occasionally combined with computational simulations. The most established experimental techniques rely on procedures to manipulate the nanomaterials using atomic force microscopy (AFM), scanning electron microscopy and transmission electron microscopy (SEM and TEM, respectively). Much of the research to investigate the properties of nanofibers has been made with carbon nanotubes, since its discovery almost thirty years ago. Their promising and remarkable properties triggered the development of techniques to test and to investigate in detail such materials and other nanofibers of interest. Because of the large number of reported works concerning CNTs, and for the fact that this material was investigated in this thesis, many of the techniques that are going to be listed next were implemented during the investigation of these materials.

2.4.1 Tests with atomic force microscopy

The atomic force microscope is an instrument that provides as main function topographical imaging through the deflections response of a cantilever that scans over the surface of a material. In this principle a laser beam is focused on the cantilever's top surface, and the changes on the direction of the reflected beam are monitored reproducing the surface of the material. In addition to the surface characterization feature, the AFM is capable of providing mechanical information of the sample being tested by simultaneously recording the force applied on a probe and the resulting displacement with very high resolution, or by detecting the resonance frequencies of nanowires and applying the elastic beam theory. The force versus displacement measurement usually is made via bending tests where a transversal load is applied through the cantilever tip on the suspended nanofiber, which is clamped onto a substrate on one end or on both extremities (Figure 6a and b, respectively). As the load increases, the nanofiber is further deflected and the changes in the elongation of the fiber is recorded producing a Force (F) vs. displacement (δ) curve. In the published works [3, 7, 38, 39], for static cases and general boundary conditions, the elasticity modulus E has been obtained with the formula :

$$E = \frac{L^3 F}{\alpha I \delta} \tag{2.66}$$

where L is the length from the clamping point to the loading point, F is the applied force, α is 3 for a free end beams and 192 for beams clamped on both sides, δ is the nanofiber deflection, and I is the cross-sectional area moment of inertia, which for a cylinder is $\pi D^4/64$.

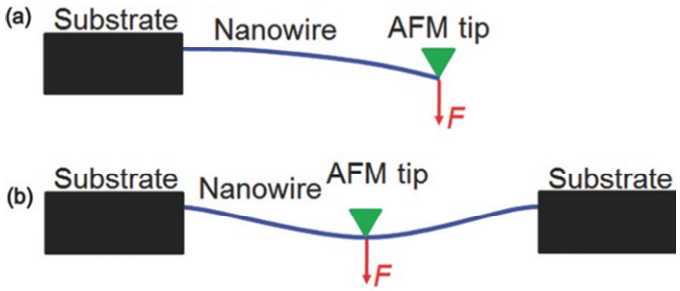

Figure 6: schematic examples of force vs. displacement bending tests in an atomic force microscope. In (a), the nanowire is clamped on one side and the force applied by the cantilever tip is applied at the end of the wire; and in (b) the scheme of a doubly-clamped nanowire, where the force is applied at the center and both extremities are fixed. Image extracted from the article [40].

The clamping of the nanofibers can be accomplished by deposition on a well-polished porous membrane made of alumina, or polycarbonate, in a way that a certain amount of fibers will end up suspended over the pores of the membrane. The section of the nanofiber hanging over the pore will then receive the load exerted from the cantilever tip. Another alternative to prepare nanofibers for the force vs. displacement test is by dispersing and depositing them on a cleaved substrate, and then laying a grid of square pads on them to later test the suspended ones [3, 7, 38, 39, 41]. Examples of these types of clamping can be seen in the figure below.

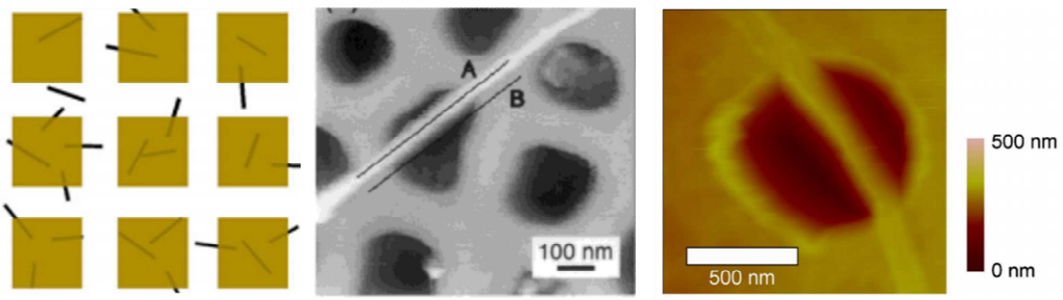

Figure 7: Illustration of clamping techniques used in AFM to test the mechanical properties of nanowires: the image on the left shows how SiC nanowires or carbon nanotubes were pinned on a substrate by square pads [41]; the two images on the right show nanotubes suspended over a membrane to receive the vertical force exerted by the AFM cantilever tip [3, 38]

Another configuration of bending test in the AFM was reported by Song et al. during the mechanical characterization of zinc oxide (ZnO) nanowires [42]. Vertically aligned ZnO nanowire arrays were scanned by a cantilever in contact mode, as illustrated in Figure 8. To extract the elastic modulus of the nanofibers, the lateral force required for the cantilever tip to bend the top of the nanowire is recorded and inserted into Equation 2.66. The length L is derived by analyzing the geometry of the bent fiber in the stage of maximum deflection and extracting the values of vertical and lateral displacement.

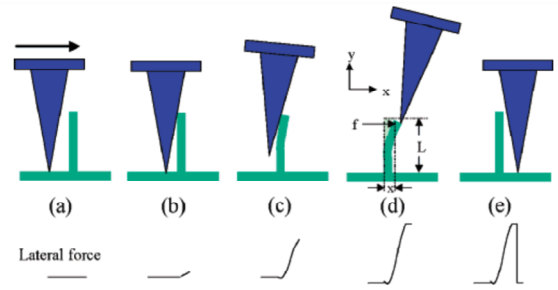

Figure 8: the AFM cantilever tip scans over a vertically aligned ZnO nanowire in contact mode producing a deflection on the nanowire. The images from (a) to (e) show the different stages of the bending test with the correlating lateral force recording [42]

AFM can also be used to extract the mechanical properties of nanofibers by detecting their resonance frequencies and applying the frequency calculations for mode resonances from the Euler-Bernoulli beam theory. In [8], the authors used a side gate electrode with oscillating voltages to electrostatically excite a doubly clamped carbon nanotube, while the vibration of the nanotube was sensed by a cantilever in tapping mode, and measured by a lock-in amplifier. The resulting resonance frequencies were inserted in the Euler-Bernoulli formula, and the Young's modulus were then obtained. Despite the quality factor Q of this type of experiment being in the range from 3 to 20, which is an indication of high energy dissipation in the test setup, this method presents an additional alternative to measure the elastic properties of nanofibers with atomic force microscopy. In vibration experiments, commonly the quality factor is used to describe the damping present in the system, and the relation between quality factor and damping ratio ζ is as follows:

$$Q \equiv \frac{1}{2\zeta} = \frac{\sqrt{km}}{c} \tag{2.67}$$

where k is the stiffness, m is the mass and c is the damping coefficient. Thus, the smaller is the damping ratio, the higher is the quality factor, meaning that the system does not present significant energy losses.

In the force vs. displacement tests performed with the AFM the error of the Young's modulus can vary from 20 – 50% for MWCNTs [3, 7, 39]. This is often associated with uncertainties in the selection of the exact point to measure the distance L and especially with the diameter to be considered in cases where it varies along the length of the fiber. Both parameters have a significant influence on the value of the modulus, since L is to the 3rd power and D is to the 4th power (Equation 2.66), for the static case. In addition, the data regarding the force and the displacement obtained from different sources may vary, due to the different conventions adopted on how the data is displayed. Therefore, for AFM bending tests to represent a reliable approach to evaluate the elastic properties of nanofibers, the distance to

the load point and the diameter should be accurately determined. Moreover, it would be a more powerful tool if the microstructure of the specimens could be observed in detail during the elastic deformations, which is better accomplish with electron microscopy.

2.4.2 Tests with electron microscopy

Using an electron microscope to perform tests in nanofibers and nanowires brings significant advantages in terms of observation and assessment of the mechanisms that integrate the dynamics of nanomaterials. This class of instruments permit the recording of the nanofiber's direct response to mechanical loading and vibration, such as displacement variations, the onset of deformation patterns, the change of the morphology of the fiber, and other unknown phenomena. Other important aspects of electron microscopes are the close examination of the fiber fixation point, and the measurement of the shape dimensions with high resolution. In addition, considering that microstructure features, such as rippling of multi-walled carbon nanotubes and stacking faults of SiC NWs do have influence on the mechanical response of nanomaterials, more and more the assistance of a scanning or a transmission electron microscope to deeply investigate and understand the elastic and plastic properties of these materials is becoming indispensable. Furthermore, the advances in microscopy techniques, with the development of ultra-sensitivity manipulation tools capable of handling nanofibers individually, place these instruments on a preferred spot when it comes to nanomechanical testing.

In mechanical tests performed within SEM and TEM there is a variety of ways in which researchers have carried out the sample preparation of nanofibers to be tested. In most of the cases, a nanomanipulation tool present inside of the chamber is employed to select an individual nanowire from a substrate and then transfer it to the testing device where it is going to be integrated. Depending on the method applied for testing, the fixation of the nanowire to micromechanical devices can be made with solid carbonaceous deposit, with a layer of silver-epoxy glue, with a conductive carbon tape, or welded with electron beam-induced deposition or with platinum.

One of the pioneer methods to test the elastic properties of nanofibers within electron microscopes was first reported by Poncharal et al. in 1999 with the transmission electron microscope [2]. This method consists of exciting the nanofiber with electrostatic forces to detect its resonance frequencies. In principle, the nanofiber is assembled as a cantilever on the tip of a nanomanipulator or a special holder at a direct current voltage V_{dc} with respect to the ground. An anode tip is placed near the nanofiber with an alternate current voltage V_{ac} with respect to the ground. The nanofiber and the tip become polarized by the two voltages, producing electrical forces between them. The natural mechanical excitations of the fiber can be observed when the voltage V_{ac} match with its resonance frequency and the elastic modulus E is derived from the Euler-Bernoulli beam theory (Figure 9). This method was subsequently reproduced by other researchers in the TEM [4, 6, 43], and in the SEM as well [44-48]. The advantage of this *in situ* test within the TEM is the possibility of observing the bended microstructure of the fiber upon excitation and to be able to track down structural defects. This

is especially favorable for multi-walled carbon nanotubes, as the onset of deformation patterns, such as rippling, may negatively affect the elasticity [2, 11].

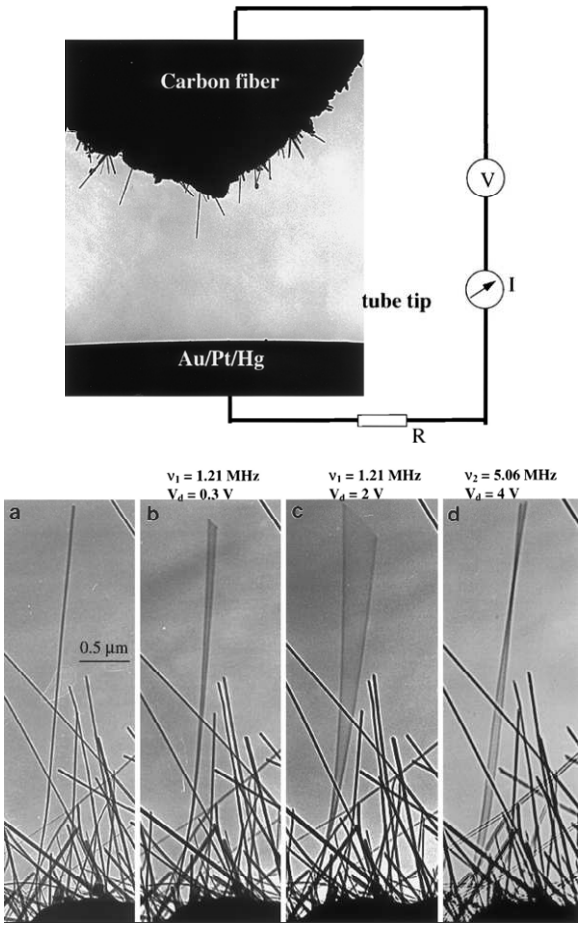

Figure 9: TEM images of the experimental setup and testing of CNTs via electrostatic deflections. The upper figure shows a scheme of the electrode and counter electrode on opposite sides with an applied voltage. Below, there is a series of images of one CNT being tested: (a) at stationary mode; (b, c) at the first mode of resonance and (d) at the second mode of resonance [43].

Other common methods to measure the elasticity modulus of nanofibers employ microelectromechanical systems (MEMS). These devices are composed of microfabricated load sensors and actuation mechanisms to perform mechanical tests in nanomaterials with good precision. Normally, they are adopted to perform tensile tests of doubly clamped nanowires and can be integrated into a SEM and a TEM [46, 49-51]. The MEMS stage used during *in situ* testing can present a thermal, an electrostatic or a piezoelectric actuator on one side, where the load originates and on the other side there is a differential capacitive load sensor that measures the applied force (Figure 10). The extremities of the specimen are clamped on each side across a gap that separates both parts of the MEMS. The test occurs by applying a force through the actuator and acquiring a series of images of the fiber elongation, which will be then analyzed to extract the fiber strain. In more advanced MEMS, a displacement sensor is built on the MEMS chip enabling the displacement to be electronically acquired [52]. The mechanical

behavior of the nanowire is represented by the stress vs. strain curved computed from the force-displacement data recorded during the tests and the cross-sectional area of the nanowire.

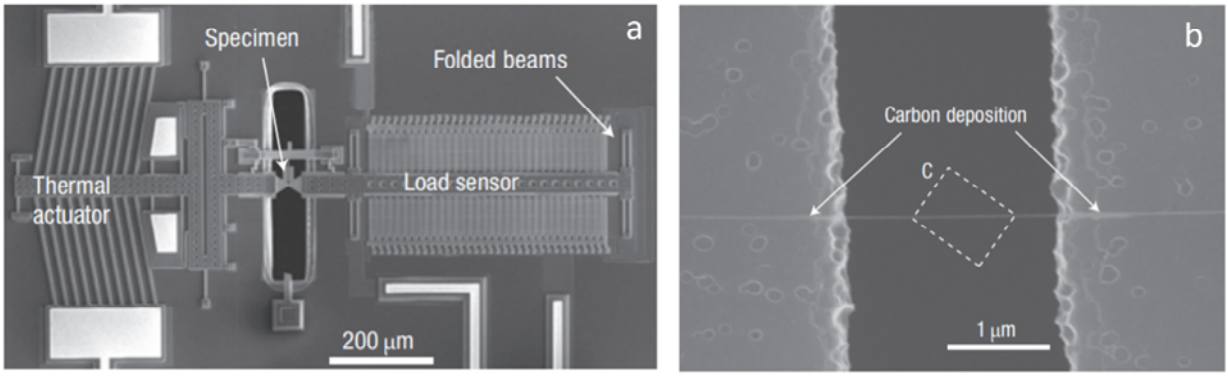

Figure 10: (a) SEM image of a MEMS with thermal actuator used to test carbon nanotubes; (b) a high magnification SEM image of a MWCNT suspended in the gap between the actuator (left side) and the load sensor of the MEMS [53].

A variation of the MEMS operates with a "push-to-pull" technique, where an external quantitative nanoindenter actuates the micromechanical device (Figure 11). A compression load is applied by the tip of an external nanoindenter onto the mobile part of the device, causing an expansion of the central gap where an individual nanowire is clamped and ultimately converting the compressive force into tensile force. The corresponding stress vs. strain curve is calculated from the force data recorded by the nanoindenter and the displacement obtained via image acquisition during the tests [49, 54, 55].

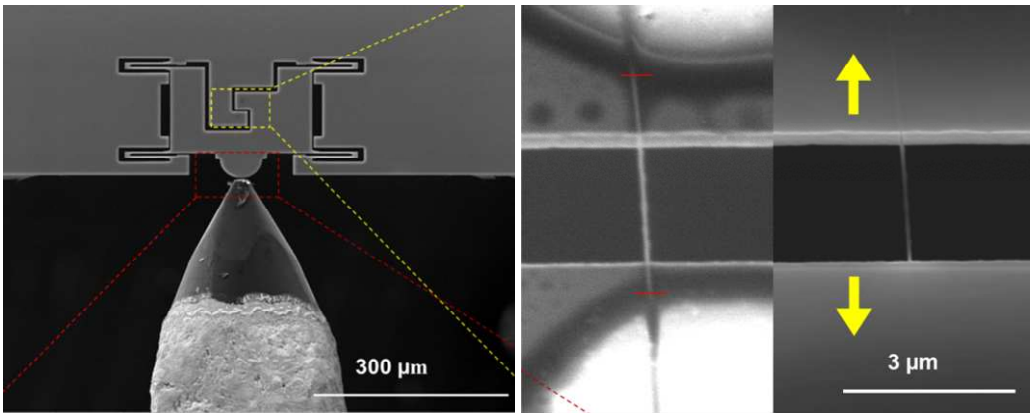

Figure 11: SEM image of a "push-to-pull" micromechanical device used to test nanowires with the view of the nanoindenter in the lower part of the image, and a close-up of the specimen under tension at the central part of the device (right) [55].

Another possibility to test nanofibers and nanowires within SEM and TEM is by integrating AFM cantilevers or nanomanipulation tools with the immediate detailed observation of the samples upon testing, done with the acquisition of electron microscopy images. In this scenario, both tensile and bending tests can take place according to the desired

experimental setup. For the realization of simple bending tests, usually one extremity of a nanowire is fixed on a tip of a nanomanipulator and the free end receives the bending load through a cantilever tip or through another microscopic tool that is connected to a force sensing instrument [56, 57]. The increase of the bending force exerted by the microscopic loading tool on the nanowire is recorded and the displacement is obtained through the image correlation analysis of the specimen while deflected (Figure 12). With the slope of the force vs. displacement curve the spring constant k is derived and next the Young's modulus E is calculated according with the Equation 2.66. A disadvantage of this method is the inaccuracy of the exact position at which the tip is exerting the force, and difficulty to evaluate if the tip is acting fully perpendicular to the fiber, or if it is slipping to the side upon application of the force.

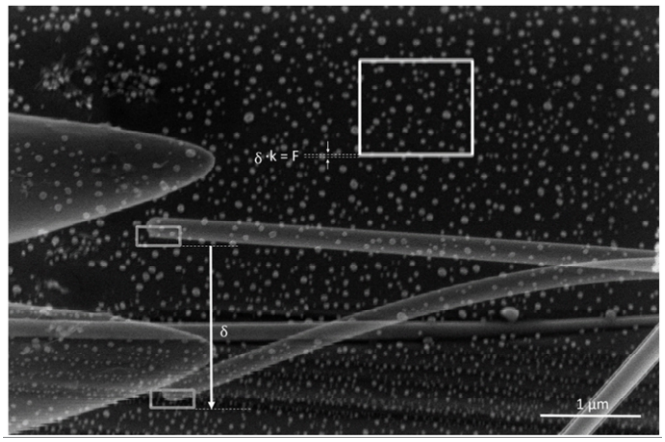

Figure 12: SEM image of a molybdenum dioxide (MoO_2) nanowire being deflected by a tungsten tip and the image correlation to obtain the resulting displacement δ [57].

A three-point-bending test can also be done by clamping the nanowire on both extremities to a fixed substrate and exerting a force through a nanoindenter tip at the middle length of the nanowire, as reported by Ma et al. [58]. In this case, the Young's modulus is calculated using Equation 2.66.

Tensile tests can be performed in SEM using two AFM cantilevers with different stiffness placed in opposite sides of one another, with the nanowire fixed at the tip of each cantilever [5, 59]. The tensile test occurs when the stiffer cantilever moves upward creating tension in the nanowire and in the softer cantilever, which consequently bends upwards (Figure 13). The resulting force acting on the nanowire is determined by recording images of the deflection of the softer cantilever and using its spring constant k. The change in the length of the nanowire is measured as well. This way, the resulting stress-strain curve is obtained.

A study published by Zhang et al. presented the comparison of the Young's modulus obtained for SiC nanowires submitted to tensile tests and resonance frequency detection in a scanning electron microscope. For the tensile tests, the nanowires were clamped using a nanomanipulation tool on the tip of two opposite AFM cantilevers, as described in the

previous paragraph. For the resonance frequency detection, the nanowires were individually clamped on the tip of an AFM cantilever, and two types of excitation tests were performed separately. One was the electrical excitation, where a counter electrode approached the AFM probe and an electric field was established with the onset of an alternative current signal. Once the frequency of the *ac* signal matched the natural frequency of the nanowire, its vibration amplitude was observed in the SEM. In the other test, the *ac* current was applied to a piezoelectric device, which provided a mechanical excitation to the AFM probe attached. The nanowire attached to the AFM tip vibrated at resonance once the frequency of the piezo matched its natural frequency. For both the resonance tests, the Young's modulus was derived from the Euler-Bernoulli beam theory. At the end, the authors showed that the average Young's modulus obtained from the three different experimental setups were very approximate, reinforcing the reliability of the techniques employed [60].

Although tensile tests in nanowires are relatively fast, in the range of a couple of minutes, this type of technique in SEMs with AFM cantilevers is very time demanding and has a very complex setup. This approach combines SEM with nanomanipulators, with AFM cantilevers, with TEM. There is the need to use nanomanipulators to fix the nanowires on the cantilever tips, the two AFM cantilevers are employed to perform the tensile tests and, the SEM monitors the change in position and shape of the parts involved, and yet there is a last step to verify with accuracy the dimensions and the microstructural changes in the TEM, when desired.

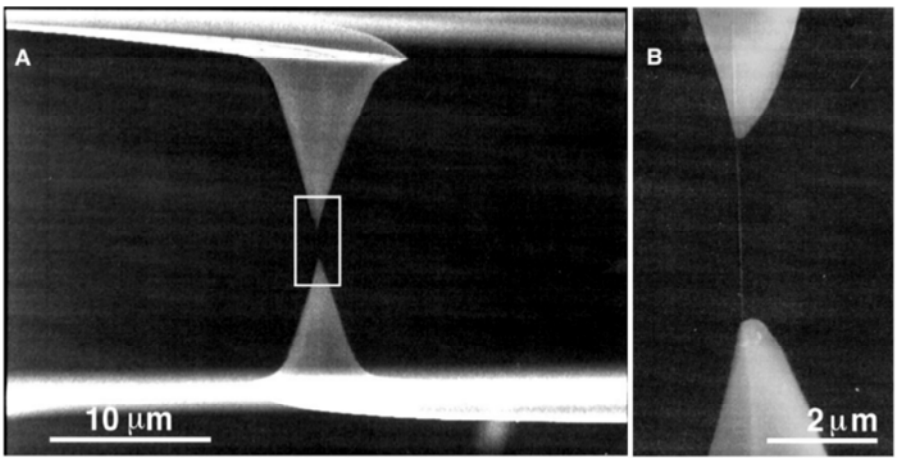

Figure 13: SEM images of a single MWCNTs being tested with AFM cantilevers. In (a) a lower magnification view of the two cantilevers setup and in (b) a closer look of the nanotube clamping on each tip [5].

Even though the *in situ* nanomechanical tests within TEMs compared to SEMs have the advantage of observing and measuring the microstructure of the samples with very high resolution, there are a few drawbacks in employing this type of microscope. Due to the very complex design and configuration of the TEM, its chamber has very limited room, restricting the use of especial sample holders with the purpose of executing mechanical tests in nanofibers and nanowires. As a matter of fact, TEMs in general admit only miniature components to

access the chamber. The SEM, on the other hand, allows enough space for more robust devices that present dimensions in the range of some millimeters, which makes it possible to be fabricated without nanomanipulation tools. Both TEM and a nanomanipulation tool increase considerably the costs of setting up a nanomechanical testing laboratory. Furthermore, TEM requires very high-skilled operational abilities. In the short future, any experimental setup that is configured to perform tests in nanofibers and nanowires with high reproducibility will take a lead in characterizing nanomaterials for industrial applications.

The methods that use resonance detection to determine the Young's modulus of nanofibers need a good signal-to-noise ratio, since they rely on imaging. To be able to achieve that, and to identify vibrations smaller than the noise amplitude, a lock-in technique is required. Additionally, these methods demand experiments with long time intervals to find the exact frequency, if ever, because for every change in the frequency, the image has to be checked. The long exposure of the specimen can cause degradation and overheating, which changes the resonance frequencies. In the method proposed in this work, the frequencies are scanned, and a straightforward protocol of the sweep in the form of amplitude and phase are obtained. This way, the long exposure of the fiber is avoided, relatively short time intervals experiments are carried out, and potentially multiple fibers can be tested simultaneously.

2.4.3 Other techniques

Another technique to characterize the elastic properties of nanofibers and nanowires is the laser Doppler vibrometry (LDV). In this technique a laser beam of the laser Doppler vibrometer is focused on an oscillating object and the frequency and amplitude of this object is extracted from the Doppler shift of the reflected laser beam frequency [10, 61-63]. The object of study can be excited thermally, by electrostatic forces, or by the laser Doppler vibrometer itself. Thus, in the case of cantilevered nanofibers, the laser Doppler vibrometry records the resonance vibration spectra of their flexural modes and the corresponding Young's modulus is obtained using the Euler-Bernoulli beam theory (Equation 2.62). However, it is necessary to analyze the samples in the scanning electron microscope in order to extract the length and diameter, needed for the calculation of the Young's modulus. This technique presents a relatively simple experimental setup, but it has to be used in combination with the SEM to assess the morphology of the nanofiber, acquire its dimensions, and it has the disadvantage of not allowing the observation of the sample during the excitation tests.

Nanoindentation employs a process similar to the tests in the AFM to measure the elastic modulus, except that the nanowire is laid on a flat substrate and the force is being applied through a sharp nanoindenter perpendicular to the nanowire, penetrating its surface. The nanowire has to be strongly clamped on both extremities to avoid shifting in the fixation point during the loading. The elastic modulus is obtained by recording a force versus displacement curve and applying the data analysis method developed by Oliver et al. [64]. Although nanoindentation is a straightforward method with simple sample preparation requirements, it has been reported that the substrate can influence the response of the nanowire to the applied load, due to the short distance between the point of loading and the contact of nanowire to the

substrate. The space restrictions that impair the transfer of load throughout the entire cross-section of the nanowires result in elastic modulus smaller than the material truly has [65-67]. It can be noticed that a standard test protocol is needed, in order to improve the reliability of the results acquired via nanoindentation method.

3. Materials

3.1 Carbon Nanotubes

Carbon nanotubes are a relatively new class of materials that led the nanotechnology revolution with its discovery a few decades ago. The unique combination of their properties strongly attracted the engineering and scientific community due to the vast field of potential applications for them. The ability of carbon nanotubes to have an unprecedented aspect ratio exhibiting a tubular nanometric structure with up to centimeters long renders these materials remarkable possibilities. For instance, the high mechanical strength together with high electrical and thermal conductivity enables the creation of enhanced composites where both mechanical performance and high conductivity are desired. From the structural applications point of view, CNTs are of great interest in the aerospace industry and in sports equipment. In electronics, carbon nanotubes present exceptional field electron-emission characteristics, which combined with their high melting point, make them good candidates for electron guns in cathode ray tube. Other applications in electronics are integrating lithium-ion batteries, or as electrodes in supercapacitors and fuel cells, and as building blocks in electric circuits. Researchers have presented the use of this material in medicine as well, as a potential support for the reproduction of neurons [68].

The development of such materials was prompted by the discovery of a new allotrope of carbon called fullerene, in 1985. A fullerene was first identified in the form of a C_{60} molecule, which consists of sixty atoms of carbon linked by single and double bonds, arranged in a closed hollow cage (Figure 14a). A couple of years later in 1991, Iijima reported in *Nature* the growth of a fullerene into a cylindrical graphitic structure with opened extremities, which became then widely known as carbon nanotubes [69]. They were formed from an arc-discharge synthesis method and were described as a "finite carbon structure consisting of needle-like tubes". These microtubes structures with one graphitic sheet (or graphene) were denominated single-walled carbon nanotubes, and the multiple coaxial tubes of graphitic sheets were denominated as multi-walled carbon nanotubes.

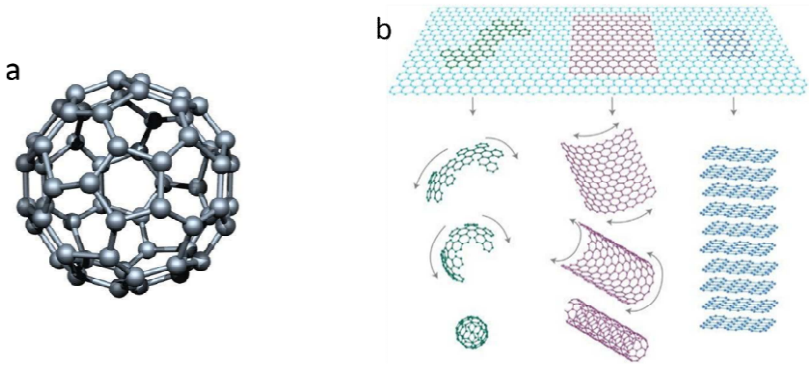

Figure 14: (a) model of the fullerene C_{60} molecular structure [70]; (b) Carbon allotropes: a fullerene on the left, a single-wall nanotube at the center, and a graphene sheet on the right [71].

The arrangement of the graphene lattice that is transformed into a nanotube varies according to the translation angle formed by the covalent bonds between the carbon atoms. This feature is called chirality and is defined by the so-called chiral vector ($\vec{C}_h$) described by the formula $C_h = na_1 + ma_2$. Depending on the value of the angle θ between the vectors C_h and a_1, the chirality of the nanotube can be armchair, zigzag, or chiral type (Figure 15). In addition, the possible variations of the chiral vector and the integers (n, m) reflect on the electronic structure of carbon nanotubes, making them either semiconducting or metallic.

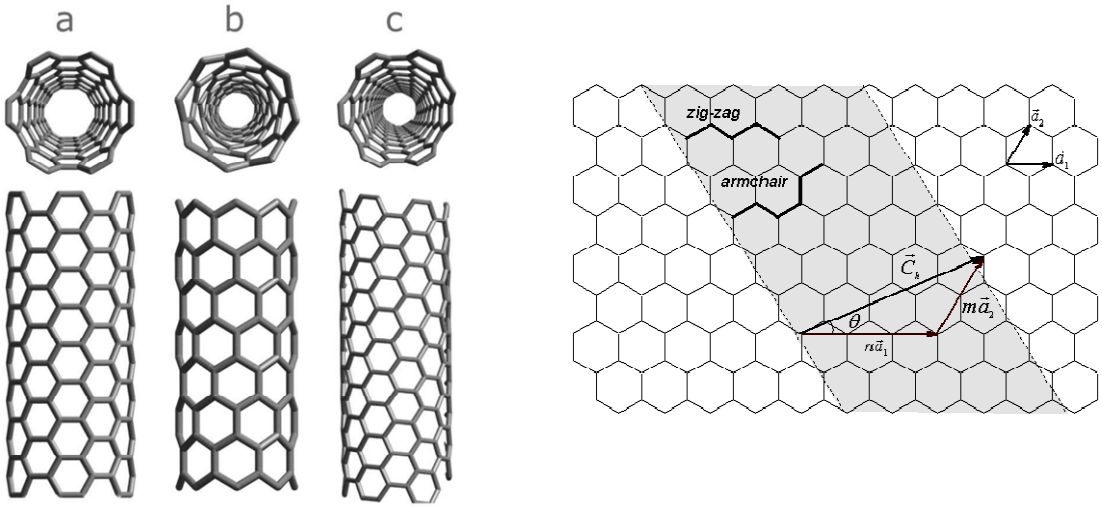

Figure 15: scheme showing the three different types of carbon nanotubes according to the chirality: (a) armchair; (b) zigzag; (c) chiral; and the representation of the chiral vector on a graphene sheet (right) [72].

3.1.1 Synthesis of Carbon Nanotubes through catalytic chemical vapor deposition

The three major methods to synthesize carbon nanotubes are arc-discharge, laser ablation and catalytic chemical vapor deposition (CCVD). The CCVD has important advantages compared to the other two methods, such as the synthesis at relatively low temperature and ambient pressure and the possibility of large-scale production. The crystallinity of MWCNTs produced by CCVD is inferior to CNTs produced by arc-discharge or laser ablation, however, in purity and yield, the method has a better outcome, and the control of the final architecture of the nanofibers is better achieved with the CCVD synthesis. This method allows the CNTs to grow in different forms, varying the diameter from thin to thick, or grouping the fibers in aligned or tangled configurations. Since it is the method through which the MWCNTs used in this work were produced, in the next paragraphs, the CCVD will be emphasized and described in detail.

In the catalytic chemical vapor deposition, a tubular reactor at atmospheric pressure with temperatures between 600 °C and 1200 °C is filled with a hydrocarbon vapor in the presence of a metal catalyst (Figure 16). The catalyst is important to permit that the hydrocarbon decomposes at a temperature below its original decomposition temperature. During the process, the hydrocarbon vapor is thermally split into hydrogen sub-products and carbon. The hydrogen species are carried away and the carbon dissolves into the metal nanoparticles. Next, when the carbon reaches its solubility limit, it starts to precipitate and crystallizes in the form of energetically stable cylindrical networks that will grow forming the nanotubes. The hydrocarbon decomposition is an exothermic reaction, that releases heat to the system and thus to the metal catalyst exposed zone. Meanwhile, the crystallization of the carbon atoms on the metal nanoparticles is an endothermic process that absorbs the heat from the catalyst metal. In this way, a heat gradient is created inside the metal and keeps the entire reaction cycle going. The most common CNT precursors are carbon monoxide, methane, ethylene, acetylene, benzene and xylene, and the most used catalysts are nanoparticles of iron, cobalt and nickel.

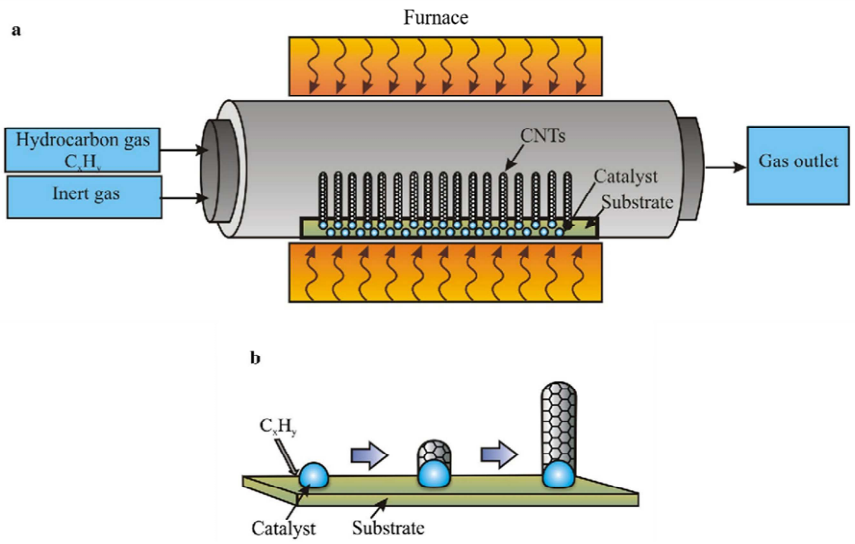

Figure 16: Schematic model of a catalytic chemical vapor deposition process showing in (a) the tubular reactor in which the chemical processes occur and in (b) the growth mechanism of a CNT [73].

The formation of single- or multi-walled CNTs depends on the size of the catalyst particle. If the particle is in the order of a few nanometers, it is more likely that SWCNTs will be formed. For bigger catalyst particles of a few tens of nanometers, the formation of MWCNTs is favored. The temperature also plays a role in the formation of each type of nanotubes, as lower temperatures (600 °C – 900 °C) yield MWCNTs, and higher temperatures (900 °C – 1200 °C) result in the synthesis of SWCNTs. This is one of the reasons why MWCNTs are more suitable for industrial production. Furthermore, the synthesis of single-walled CNTs leaves a metal residue of 20-30% by weight [74], while the synthesis of multi-walled CNTs lead to 1-10% by weight of impurities [75], which can be eliminated by purification in an argon/hydrogen plasma stream with transit times in the plasma between 7 and 15 ms [76].

3.1.2 Elastic behavior of MWCNTs

Since their discovery, many researchers have studied the mechanical properties of carbon nanotubes with the assistance of various microscopy instruments such as AFM, SEM, TEM, and laser Doppler vibrometry (LDV), in combination with tensile tests, force vs. displacement tests, and resonance frequency detection. The first reported experimental investigation to obtain the Young's modulus of multi-walled carbon nanotubes was made by Treacy et al. in 1996 [77]. In this work, the nanotubes were anchored and excited in a TEM. Upon measuring the resonance frequencies of the thermally induced oscillations, the Young's modulus for each nanotube was derived. Remarkably high values of Young's modulus up to 4.15 TPa were found, however for the group of eleven nanotubes tested, individual values ranged from 0.4 to 4.15 GPa, reflecting the inhomogeneity of the samples or the difficulty of accuracy in the parameters, such as the measurement of the nanotube's dimensions.

Among the works that describe the investigation of the Young's modulus E of carbon nanotubes by measuring their resonance frequencies, Poncharal et al. introduced a technique to detect the resonance frequencies of electrically excited MWCNTs in the transmission electron microscope (TEM). By applying an alternating voltage to a CNT fixed to an electrode, the fiber became electrically charged and started to oscillate towards or against a second electrode. In this way, the resonance frequencies were directly obtained and consequently the bending behavior of the nanotubes analyzed [2]. Young's modulus values from 100 to 1000 GPa were found for MWCNTs synthesized by arc-discharge with diameters ranging from 8 to 40 nm. An important remark made by these authors was the acknowledgement of a decrease of E with the increase of the nanotubes thickness, which was associated with a rippling effect of the inner walls by the compression under bending. In similar studies, it was observed that thinner MWCNTs tend to exhibit larger modulus values (1000 GPa), whereas thicker nanotubes exhibited considerably smaller modulus values (200 GPa) [2, 4, 6], confirming what was proposed in [2]. Using the same technique mentioned above, other authors reported investigations of the mechanical properties of single-walled and multi-walled carbon nanotubes synthesized by the catalytic chemical vapor deposition. Gao et al. found dynamic Young's modulus for MWCNTs with diameters between 30 and 70 nm considerably smaller

(30 GPa) than the values described by Poncharal et al. [4]. In this case, the nanotubes were thicker than the ones studied by Poncharal et al., and the synthesis method was different. Other studies also showed reduced values of Young's modulus (~28 GPa) for MWCNTs with around 45 nm of diameter [10, 11]. Lower Young's modulus values were observed for MWCNTs synthesized by CCVD, tested with distinguished techniques and in various instruments, as can be seen in Table 2. The authors associated the low modulus values to the significant presence of defects in the nanotubes structure, the misalignment of the planes and lower degrees of crystallinity for MWCNTs originating from CCVD. An exception of high elasticity for MWCNTs originated from CCVD was seen in the work of Yamamoto et al. [78]. In their investigation, a group of nanotubes were submitted to a series of annealing treatments with the purpose of removing structural defects and enhancing the degree of crystallization. As a result, the treated nanotubes presented very high E_b, comparable to the CNTs produced by arc-discharge.

Although multi-walled carbon nanotubes produced by CCVD have been showing elastic properties below the levels announced for these materials, it is crucial to deepen the understanding of their mechanical properties, since such materials are most relevant for industrial applications.

Table 2: Previous studies of the Young's modulus of MWCNTs with different diameters, produced by the most common synthesis methods as reported by other authors. The Young's (E_Y) and the Young's modulus (E) values are approximated to the values given in the literature. "F vs. δ" stands for force-versus-deflection testing.

MWCNTs Synthesis	D (nm)	E (GPa)	Testing Method	Detection	Ref.
Arc discharge	> 30	E = 200	resonance detection	TEM	[4]
Arc discharge	< 10	E = 300	resonance detection	AFM	[8]
Arc discharge	5 - 40	E = 140 - 780	bending test	**FEG - SEM	[11]
Arc discharge	12.5	E = 800	bending test	TEM	[79]
Arc discharge	5 - 10	E = 810	bending test	AFM	[3]
Arc discharge	13 - 36	E = 270 - 950	tensile test	SEM	[5]
Arc discharge	< 25	E = 400 - 1060	resonance detection	TEM	[77]
Arc discharge	2 – 50	E = 990 - 1105	tensile test	TEM	[53]
Arc discharge	10	E = 620 - 1200	tensile test	SEM	[9]
Arc discharge	< 8	E = 1200	resonance detection	TEM	[2]
Arc discharge	26 – 76	E = 1280	bending test	AFM	[41]
Arc discharge	5 – 25	E = 400 - 4150	resonance detection	TEM	[77]
*CCVD	30	E = 27	bending test	AFM	[3]
CCVD	30 - 70	E = 20 - 30	resonance detection	TEM	[4, 6]
CCVD	160 - 180	E = 20 - 60	resonance detection	***LDV	[10]
CCVD	5 - 20	E = 40 - 80	bending test	**FEG - SEM	[11]
CCVD	10 - 80	E = 10 - 100	bending test	AFM	[7]
CCVD	20 – 50	E = 350	bending test	AFM	[38]
CCVD	10 – 25	E = 6 – 700	bending test	AFM	[39]
CCVD	33 – 124	E = 50 - 1360	tensile test	SEM	[78]

**CCVD – catalytic chemical vapor deposition; **FEG – Field emission gun; ***Laser Doppler vibrometry*

3.1.3 Multi-walled carbon nanotubes studied

In this project large diameter individual multi-walled carbon nanotubes type NM-401 were used (Figure 17). The samples were provided by the European Joint Research Center (JRC) Repository for Representative Test Nanomaterials together with information about the characterization of the nanotubes. According to the JRC, the NM-401 MWCNTs present an average outer diameter of 64 ± 24 nm, a small inner diameter of maximum 10 nm and a high degree of graphitization. For the mean diameter of 64 ± 24 nm a D_i smaller than 10 nm would contributes less than 3% to the difference term $(D^2 - D_i^2)$ [80]. The contribution of the inner diameter to Equation 2.62 was therefore neglected. The density of these nanotubes was assumed to be $(1.8 \pm 0.1) \cdot 10^3$ kg/m^3 [81]. This type of MWCNTs has been extensively used for toxicological tests and became a reference in this field of research. For this reason, it has been selected to be tested in this work.

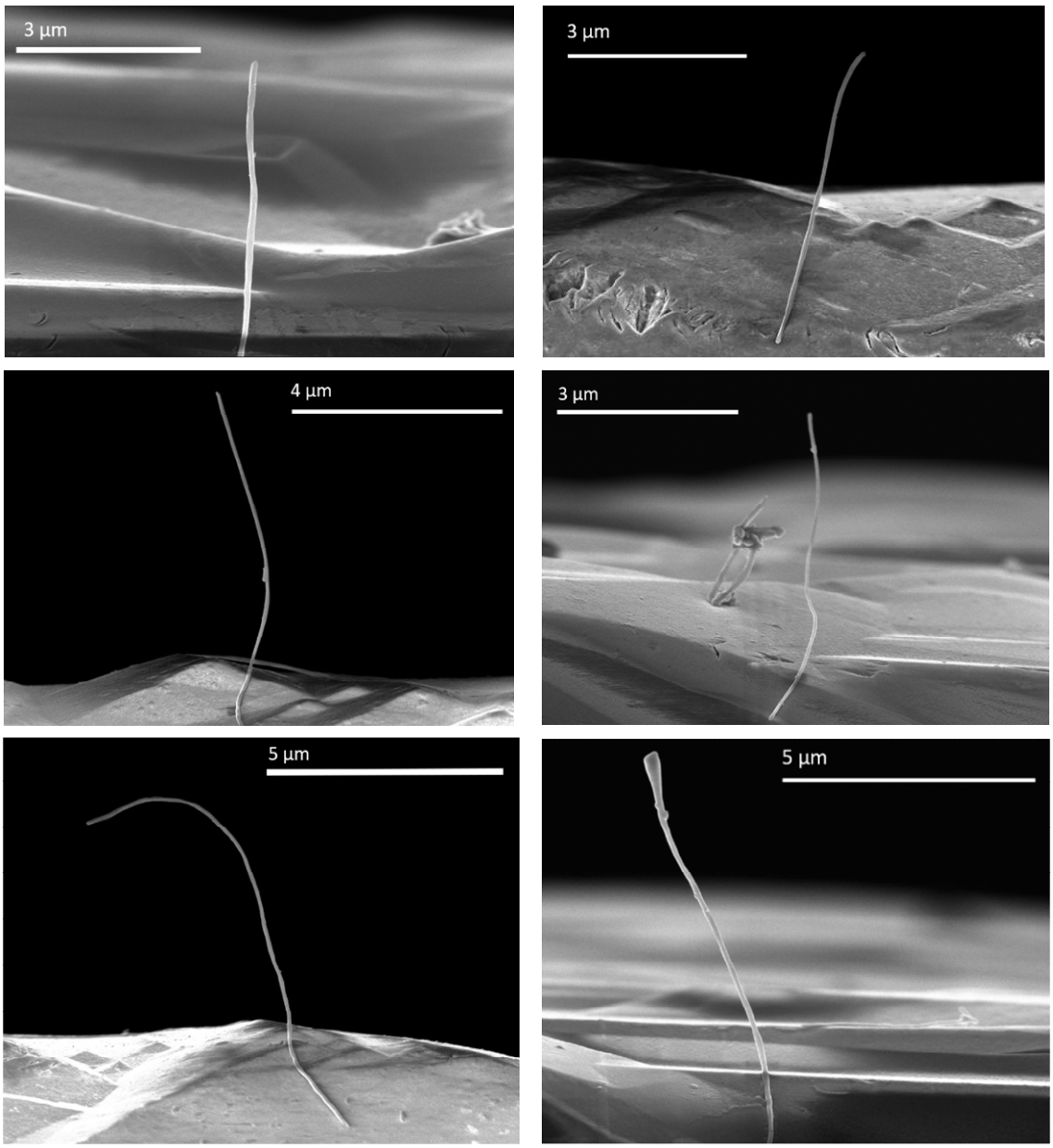

Figure 17: High resolution SEM images of a set of the NM-401 MWCNTs samples used in this project. The nanotubes in these images are fixed on a PEDOT:PSS film standing free on piezoelectric quartz crystal units. High resolution SEM Hitachi SU8230 from BAuA.

3.2 Silicon Carbide Nanowires

Another type of nanofibers with great potential to be incorporated into the industry and into objects of everyday life are the silicon carbide nanowires. These nanowires present high thermal conductivity, good semiconducting characteristics, chemical stability, and radiation resistance. Apart from these features, SiC NWs have remarkable mechanical properties, such as high stiffness and elevated strength. Due to their superior properties these NWs can potentially be applied in distinct areas. In electronics, it can potentially be used in sensors, flat screen displays, in microwave tubes, as these material shows improvement on the electron

field emission by tailoring the band gap of the NWs. They are good candidates for that, as they are chemically and thermally stable, and present favorable mechanical behavior, allowing them to withstand harsh environments [82]. Another application for these nanowires is integrating microelectromechanical systems (MEMS), since they can operate as nanoresonators for high frequencies with large Q factors, combined with the endurance to severe temperatures [83]. Furthermore, SiC NWs become hydrophobic and increase the water barrier when grown aligned, being very suitable for the use in self-cleaning coating films, which could be applied as protection on glasses or metallic surfaces [84]. Regarding their remarkable mechanical properties, SiC NWs exhibit high Young's modulus and tensile strength, which makes them appropriate to be used as reinforcement in ceramic or polymeric matrixes, improving the mechanical behavior of the whole composite [85]. In addition to improving the mechanical properties of composites, these nanowires are able to enhance their electrical response as well [86].

The lattice structure of bulk SiC is composed by four atoms of silicon strongly bonded to one atom of carbon in a tetrahedral geometry. Its crystal structure, however, can vary considerably, as it presents polymorphism. The polytypes of SiC are classified according to the arrangement of stacking layers, which are denominated by the letters A, B and C in a sequence (Figure 18). The NWs used in this work have the polytype 3C – SiC, which corresponds to the sequence ABC and is also denominated β-SiC. This polytype is isotropic and is the only cubic crystalline structure of SiC.

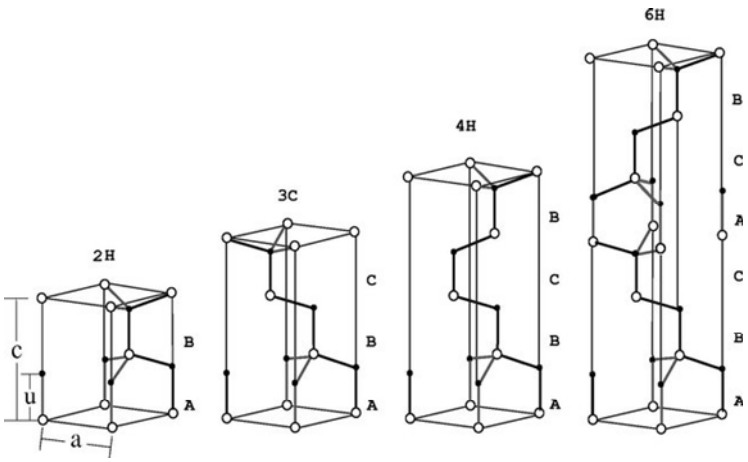

Figure 18: examples of polytypes of SiC [87].

SiC NWs also present several kinds of morphology configurations, as can be seen in Figure 19. Each type of configuration is obtained by varying the parameters of the synthesis, such as cooling temperature, pressure, catalyst material, precursor material, and carrier gas. The morphologies observed in the SiC NWs from this work were the cylinder nanowire (Figure 19a), the bamboo-like (Figure 19d) and the twinned type (Figure 19e). However, the resonance frequencies were detected only with the twinned and nanowire shapes.

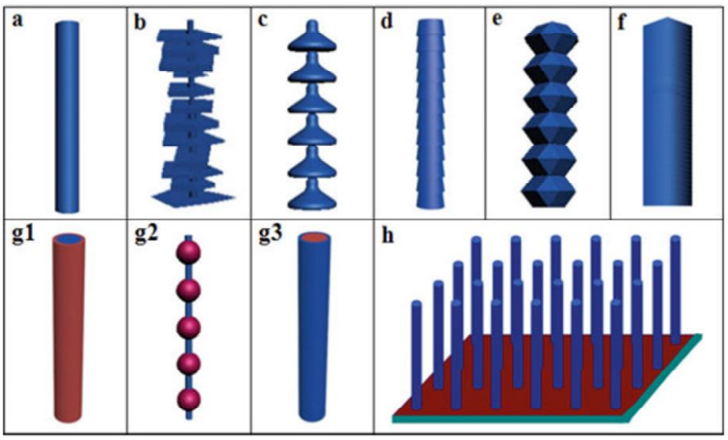

Figure 19: some examples of the most common morphologies: (a) Typical nanowire, (b) hierarchical, beaded nanochains, (d) bamboo-like, (e) twin, (f) bicrystalline, (g1) SiC core-based nanocables, (g2) nanochains, (g3) SiC shell-based nanocables, (h) nanoarrays [88].

The most common synthesis route to produce SiC NWs is the chemical vapor deposition (CVD), described in section 3.1.1, with the remark that in this case also a source of Si has to be added as a precursor. The main mechanisms applied for the growth of the nanowires are often referred to as vapor-liquid-solid (VLS) or vapor-solid (VS), which allow the fabrication of large amounts of nanowires. The VLS mechanism makes use of a metal catalyst, similar to the growth of CNTs. During this process, the precursor species in the gas phase form a liquid eutectic mixture with the catalyst, until the system is supersaturated and nucleation occurs, followed by the formation of the solid phase. At the end of the growth, metal nanoparticles from the catalyst are attached on the tip of the nanowire or become incorporated into the growth. In the VS mechanism, no catalyst is used, and the growth of the nanowires is governed by a direct condensation of the vapor into the solid phase. In this mechanism, the nanowire has no impurities from the catalyst and a uniform growth and the desired morphology can be achieved by altering the temperature of the reaction [89].

The SiC NWs used in this work were obtained from ASC Material, LLC (Pasadena, California, US) with a range of diameters from 100 to 400 nm, lengths varying from 7 to 45 μm and a density of $3.21 \cdot 10^3$ kg/m^3. These nanowires were synthesized by chemical vapor deposition, which for SiC NWs is referred to as VSL mechanism of growth. Figure 20 shows images of different types of SiC nanofibers observed within the samples.

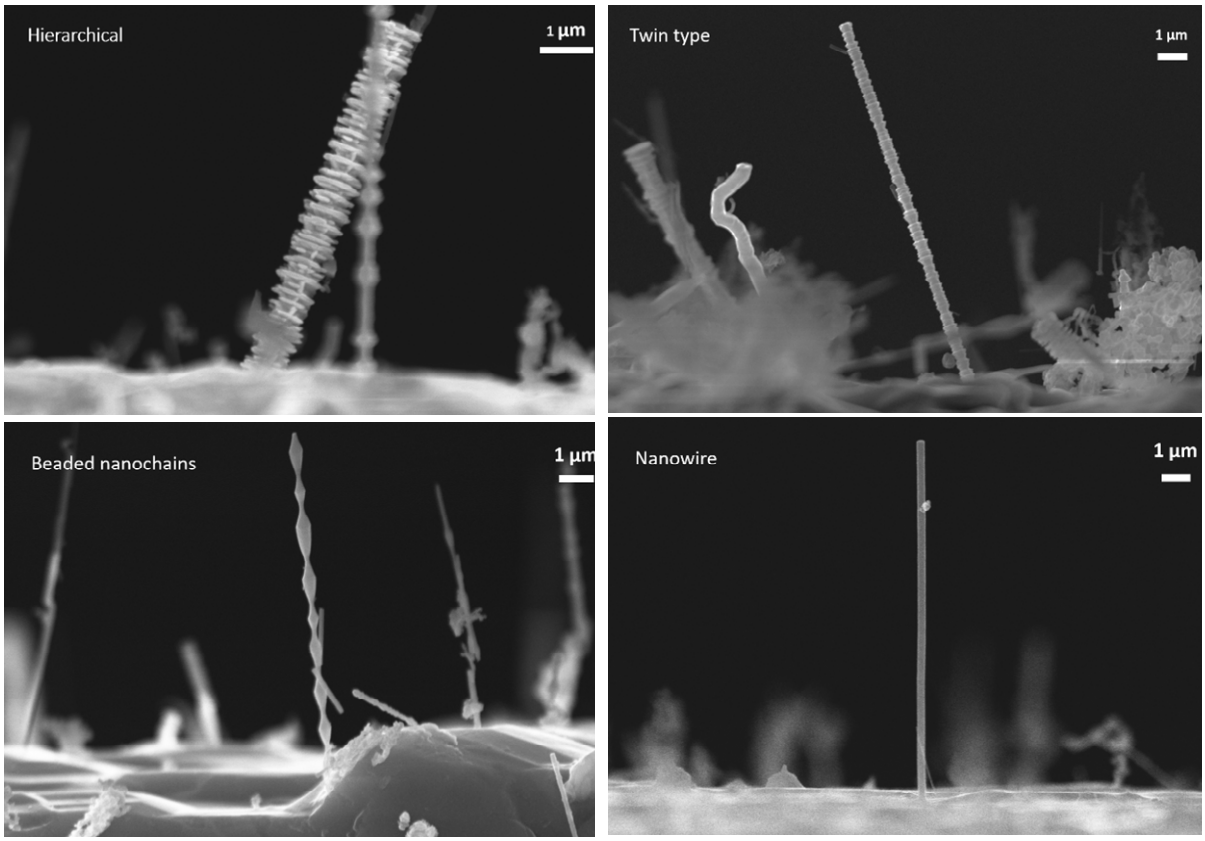

Figure 20: SEM images of different morphologies of SiC nanofibers observed during the qualitative analysis of the samples prepared for the resonance detection tests [90].

3.2.1 Elastic properties of SiC NWs

In the last years, many works have been focusing on the mechanical properties of SiC NWs, as this material shows promising structural behavior. To investigate the elastic properties of these nanowires, researchers have been using techniques such as tensile and bending tests, nanoindentation and resonance frequency detection. These tests are normally performed in situ with atomic force microscopy, scanning electron microscopy or transmission electron microscopy, integrated with the nanomanipulation tool that provides the loading or the excitation source, depending on the principle applied. The values of Young's modulus of SiC NWs encountered by the researchers in the last years vary from 60 to 1270 GPa. This large disparity is related to the different allotropic states or crystallinity levels of the samples tested, which not always has been clarified in the reported works. In addition, the presence of stacking faults in nanowires of the same crystalline structure can strongly affect the elastic response, as reported by Cheng et al. [49]. Table 3 presents a summary of the Young's modulus values and the techniques used in previous research that investigated the elastic properties of SiC NWs.

Table 3: Previous results of Young's modulus of SiC NWs and the testing methods used to characterize the mechanical properties

SiC NWs Synthesis	D (nm)	E (GPa)	Testing Method	Detection	Ref.
CVD	102 – 350	E = 60 – 160	tensile test	SEM	[60]
CVD	148 - 596	E = 23.5 – 169	resonance detection	SEM	[60]
Not mentioned	200	E = 203	tensile test	SEM	[46]
CVD	40 – 200	E = 250	tensile test	TEM	[50]
CVD	270	E = 470	resonance detection	SEM	[44]
CVD	215 – 400	E = 540 – 576	nanoindentation	SEM/*SPM	[47]
CVD	20 - 23	E = 610 – 660	bending test	AFM	[41]
CVD	17 - 143	E = 230 – 750	resonance detection	SEM/**FEM	[45]
CVD	17 – 45	E = 166 – 1270	tensile test	SEM	[49]

**Scanning probe microscopy; **Field emission microscopy*

3.3 Piezoelectric Actuators

To excite the nanofibers during the in situ SEM experiments, mass-produced tuning fork quartz crystal units of type CA-301 with 18 pF capacity and resonance frequency of 12 MHz ± 30 ppm (Seiko Epson Corporation, provided by Mouser Electronics Inc., Munich, Germany) were used. Thin electrodes plates adhered onto the quartz surface produce the electric field on both sides of the quartz, allowing this device to be used as piezoelectric actuator with a high quality factor. For the resonance detection experiments, these units were mostly operated well below the specified resonance of 12 MHz, since the nanofibers tested presented natural frequencies lower than this value. Their cylindrical steel enclosure of 3 mm diameter and 9 mm length was carefully carved on a lathe and removed manually to lay bare the rod-shaped quartz crystal (Figure 21).

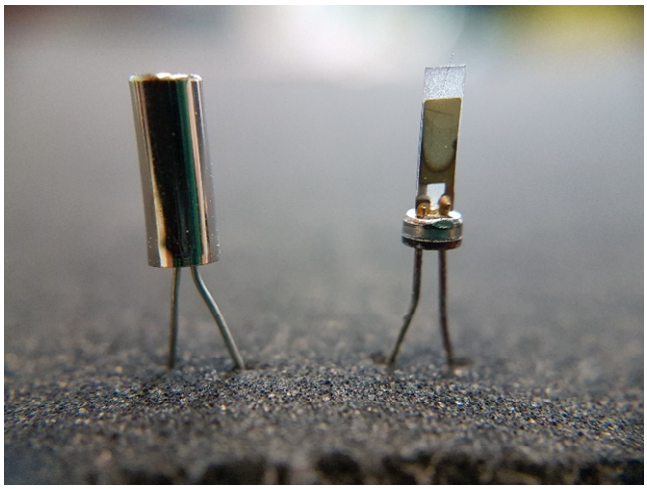

Figure 21: a tuning fork quartz crystal unit as purchased (right) and after the removal of the metallic cover. These piezoelectric quartz units were used as actuators for the excitation of the fibers. The fibers were fixed standing free on the tip of these units, and the ones standing out on the edges could be analyzed.

After the sample preparation described next in Section 4.1, the electrical wires of the piezo quartz (tuning fork crystal units) were soldered to a coaxial SubMiniature version B connector (SMB—straight jack for PCB mounting, Figure 22). For the in-situ experiments, the quartz was mounted on the scanning electron microscope (SEM) stage and connected to a Belling-Lee connector/SubMiniature version B (BNC/SMB) vacuum chamber feedthrough. Reliable detection of fiber resonances required a driving voltage amplitude of about 10 V for the piezo crystal.

The SMB connector (golden connector soldered to the wires of the piezo quartz in Figure 22) was carefully adjusted in a way that the quartz surface where the nanofibers were standing free (black mark on the tip of the quartz) would be facing upwards in front of a non-metallic background. This was important to ensure a good contrast for the nanofibers to stand out from the surroundings, improving the image quality and decreasing the signal-to-noise ratio.

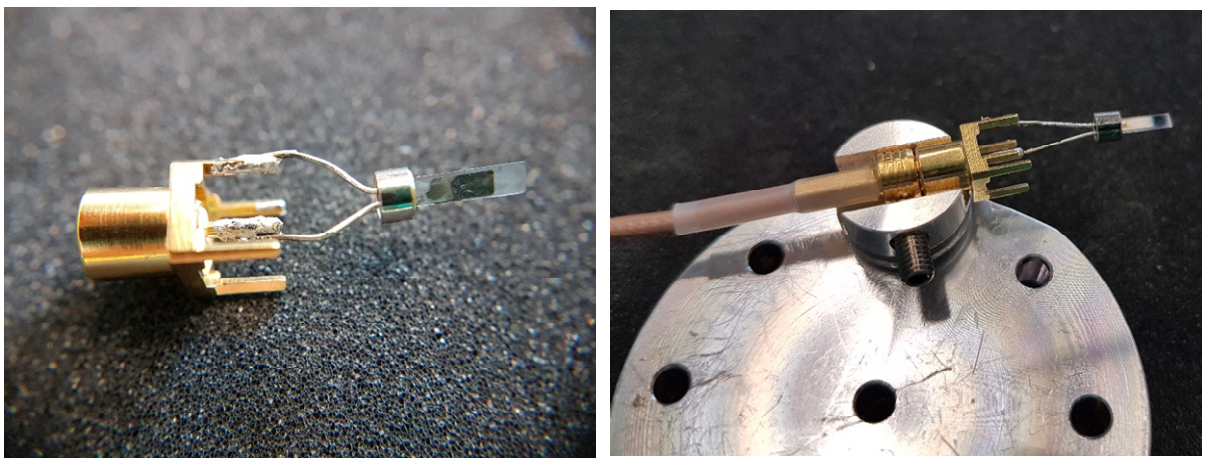

Figure 22. A closer look of the piezo quartz unit soldered to the SMB connector (left); the complete configuration of the piezo quartz containing multi-walled carbon nanotubes: the piezo is connected to a SMB adaptor and to the vacuum chamber electric feedthrough. This setup was then fixed on an aluminum stub and mounted on the SEM stage for the experiments (right).

4. Methods

4.1 Preparation of Free-Standing Nanofibers

4.1.1 Fixation of nanofibers using PEDOT:PSS polymer

To accomplish the fixation of nanofibers by the base on the surface of an oscillatory and conductive device, the following procedure was applied: the tip of a piezoelectric quartz crystal unit was first metallized at one side using a Leica EM ACE600 sputter coater (Leica Microsysteme Vertrieb GmbH, Wetzlar, Germany) through a mask that selectively prevented metal deposition on the electrical contact area of the quartz. This way, the upper quartz-driving metal electrode was extended towards the tip of the quartz rod. Up to 17 quartz units were placed in a special 3D-printed mask and first coated with 10 nm of iridium, followed by 30 nm of gold. The iridium has the function of promoting a better adhesion of gold on quartz. Subsequent adhesion tests were performed with a light scratching metallic tool, and an adhesive tape. No damage occurred on the film, neither the gold layer was removed. Thus, the resulting thin film coating showed to be effective.

The tip of the gold-coated quartz was then dip-coated in an ethanol solution with 50 mM of a thiol (9-Mercapto-1-nonanol, Sigma-Aldrich Chemie GmbH, Taufkirchen, Germany) for 48 h and rinsed with ethanol afterwards. The thiol formed self-assembled monolayers (SAM) on clean gold surfaces, creating stable gold-thiol bonds with one end of the molecule. The polar hydroxyl group at the other end of the molecule improved the wettability of gold and served as adhesion-promoting layer for a subsequent PEDOT:PSS (poly(3,4-ethylenedioxythiophene)) polymer coating. The polymer was applied by dip-coating the quartz tip for 10 s in an aqueous PEDOT:PSS suspension (3.0%-4.0% in H_2O, Sigma-Aldrich). The suspension was soft and sticky in wet state but dried to a solid conductive polymer within a few 10 min at room temperature. The polymer served first to electrostatically embed and then to immobilize the ends of nanofibers and to connect them electrically to ground potential. This prevented the charging of the nanofibers during SEM and DySEM analysis.

The nanofiber deposition procedure followed dip-coating after a brief initial PEDOT:PSS drying period of 5 min. These 5 min were not sufficient to let the coating dry completely but left it in a viscous state suitable for the nanofiber penetration upon fiber deposition. Impaction of the viscous polymer film with fibers that were vertically oriented with respect to the quartz surface was achieved by electrostatic precipitation of nanofiber-containing aerosols. Subsequent PEDOT:PSS suspension drying led to the immobilization of immersed fiber ends. Figure 23 presents the resulting piezo quartz units with the nanofibers deposited on the tip.

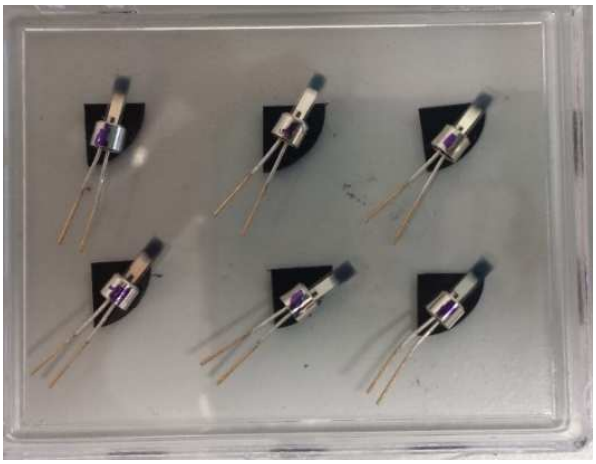

Figure 23: Examples of the piezo quartz units presenting the nanofibers at the tip (black spot).

The setup used for aerosol preparation and precipitation is shown in Figure 24. It consisted of three parts: an aerosol generation chamber, a sedimentation chamber and a nanoparticle aerosol sampler (NAS) of type TSI 3089 (TSI GmbH, Aachen, Germany)[91]. The aerosol generation chamber was filled with a mixture of glass beads (Swarcoflex glass beads, diameter 400–600 μm, roundness ≥ 80%, SWARCO M. Swarovski GmbH, Germany) and nanofiber powder with 2 mass percent of fibers. The aerosol chamber was mounted on a laboratory vortex shaker MS 3 digital (IKA ®-Werke GmbH and CO. KG, Staufen, Germany) operated at 2000 rpm. Actuated by the vibration, the glass beads performed a milling process upon collision with nanofibers agglomerates. The break-up of the nanofiber's agglomerates generated an aerosol containing also individual fibers that was carried by an airflow of 2 slm. Larger agglomerates and glass bead debris settled in the intermediate sedimentation chamber before the aerosol entered the NAS inlet. Inside the NAS, an electric potential difference of 10 kV between inlet and NAS electrode generated a field strength of 1.2 kV/cm. It attracted and accelerated charged aerosol particles in the airflow towards the conductive, semi-dried PEDOT:PSS layer of the quartz crystal on the NAS electrode. The anisotropic morphology of fibers in combination with natural and during milling triboelectrically induced charges on the fiber led to their alignment along the applied electric field. This way, the nanofibers were impacted fiber-end onwards into the polymer layer. After layer drying, the fibers were immobilized mostly in erected orientation, as required for resonance measurement, cf. Figure 25.

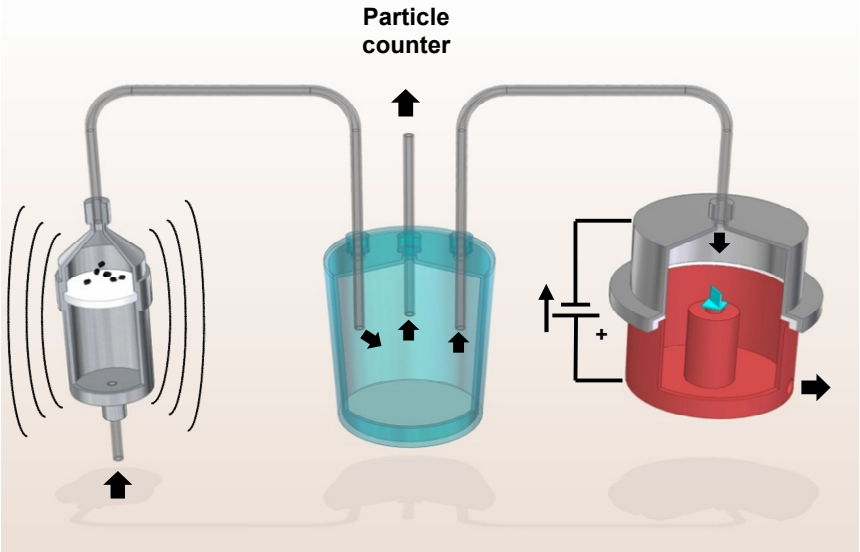

Figure 24. Schematic of the electrostatic nanofiber aerosol precipitation setup: Aerosol generation chamber supplied with carrier gas (left); sedimentation chamber (center); electrostatic precipitator (right). Image extracted from the article [92].

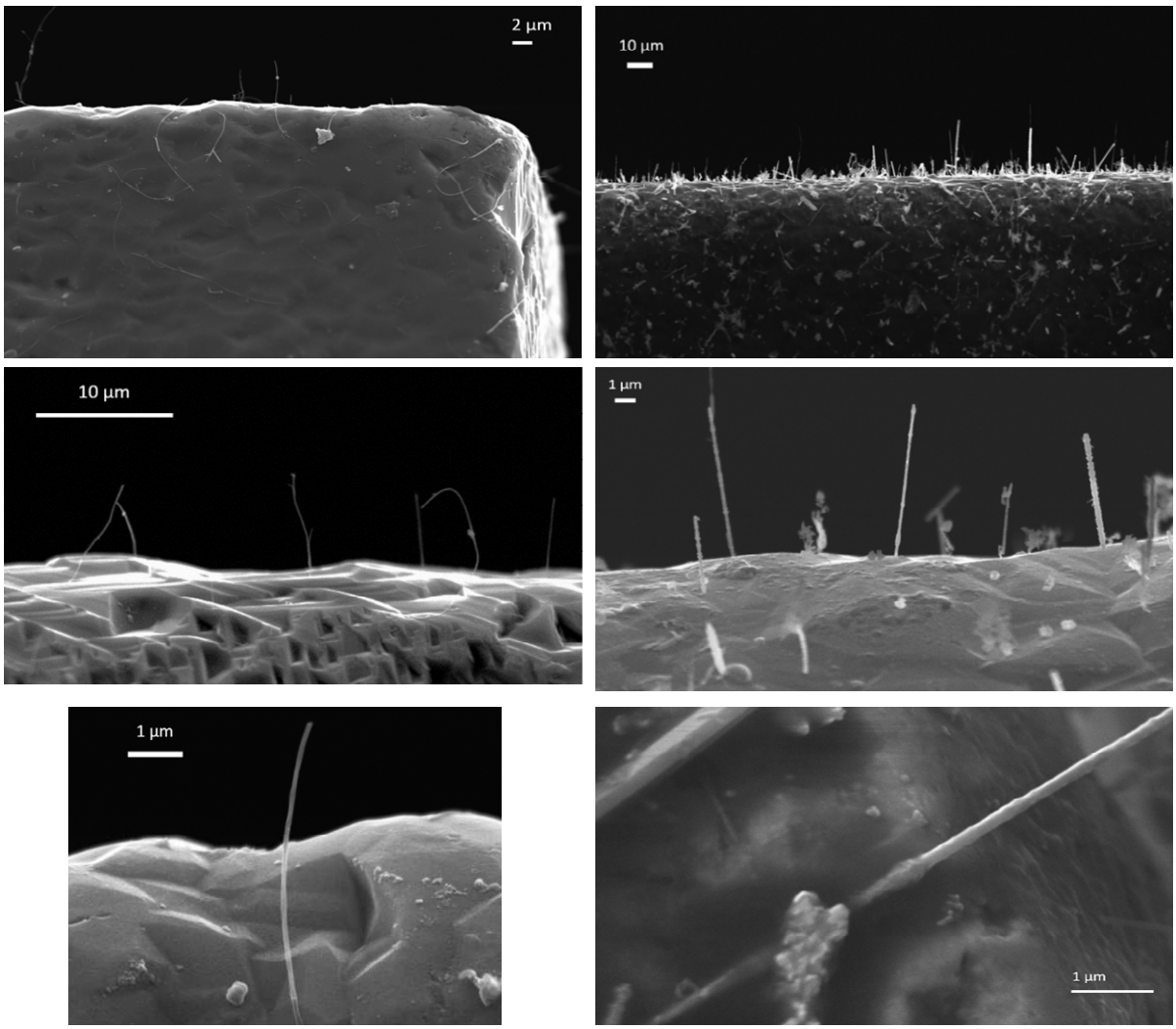

Figure 25. SEM images of the configuration of the nanofibers standing free on the edges of the piezos, fixed by the PEDOT:PSS polymer film: (left column) MWCNTs used in this work, and (right column) silicon carbide nanowires tested.

4.1.2 Fixation of nanofibers using the focused ion beam scanning microscope

In the initial phase of the project, an attempt to individually select the nanofibers and place them on the piezo quartz substrate was made using a focused ion beam deposition in cooperation with the Center for Electron Microscopy (ZELMI – Technische Universität Berlin). The goal here was to test an alternative method of clamping the nanofibers on the piezo to compare the quality of the samples with the ones obtained through adhesion with PEDOT:PSS. In the focused ion beam scanning electron microscope (FEI/Thermofischer HELIOS NanoLab 600 with dual beam Gallium ions), the device containing a microscopic needle collected a single MWCNTs from a field of nanotubes of the same kind that were placed on a metallic substrate and then carried it by electrostatic forces to a pre-determined position on the piezo. Next, the CNT was fixed at the base on the desired location by electron beam-induced deposition of Pt, in a process similar to soldering. At the end of the operation, the length and the exact location of the fiber were well known, and the fiber clamping was made in a controlled manner. In this way, the fiber could potentially be used as a reference for the initial tests. A sequence of images illustrating the step-by-step of the FIB procedure performed for the MWCNTs is shown in Figure 26.

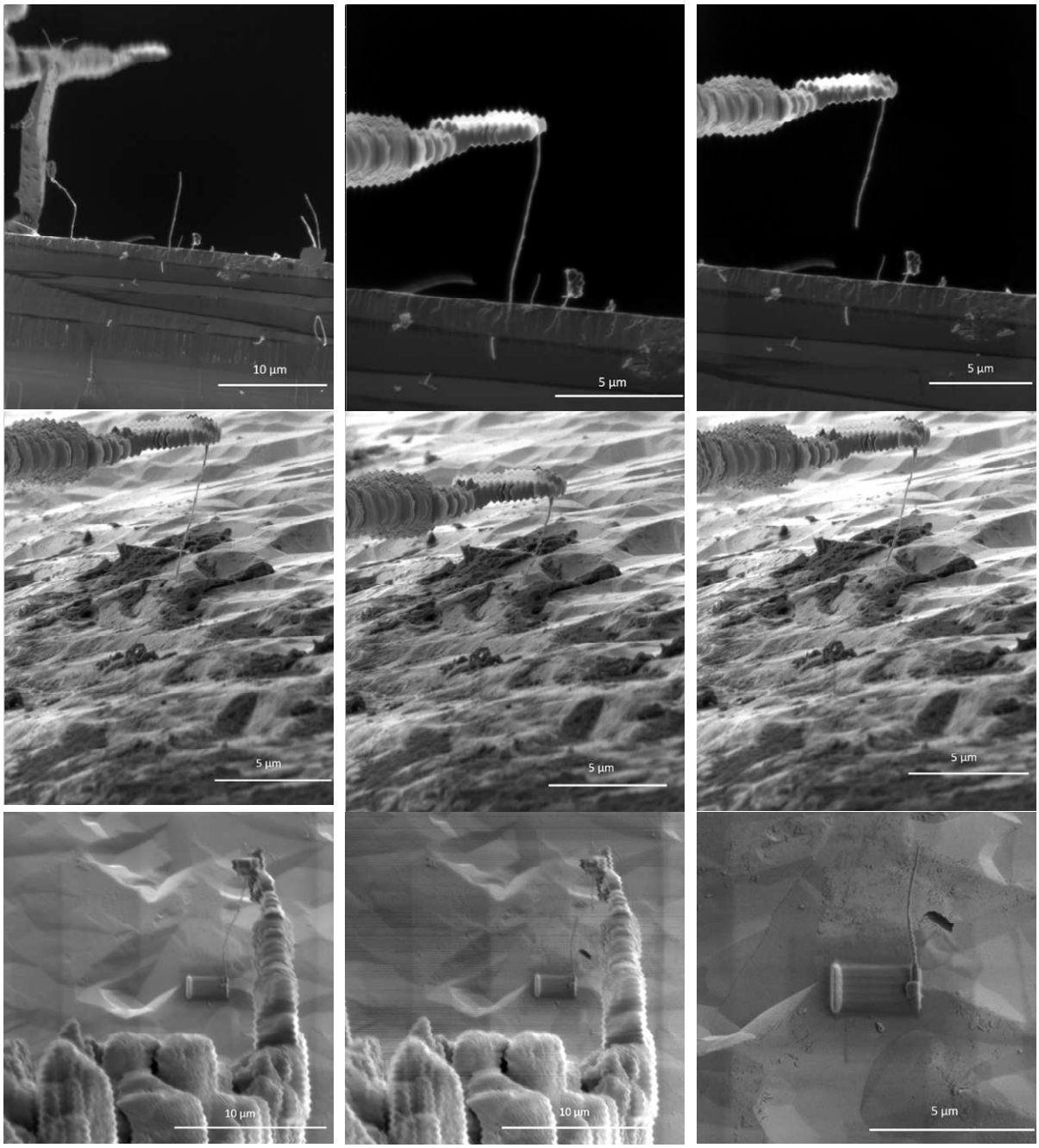

Figure 26: sequence of FIB-SEM images showing the step-by-step of the attempt to select one single CNT to be fixed onto a piezo via Pt deposition; in the first row, a long and straight MWCNT is collected from a substrate with many others MWCNTs. The nanotube attaches to the microscopic needle though electrostatic forces; in the second row, the needle brings the nanotube to the piezo and places it in a pre-defined position, where the Pt deposition will next occur; in the third row, a block of solidified Pt is formed at the basis of the nanotube, fixing it on the piezo. Next, after the needle releases the CNT, it is possible to notice an accumulated mass of Pt from the base until the middle length of the fiber.

At the end of the operation however, the material used for the deposition and fixation of the fiber on the piezo solidified beyond the bottom area and was incorporated onto the surface of the nanotube along its length rather than only at the base. This way, the overall mass of the nanotube was altered, changing consequently its average density. Thus, the Euler-Bernoulli equation could no longer be applied to this fiber upon detection of resonances, invalidating

the nanotube for the tests. Besides that, the fixation of CNTs with FIB required a much longer period of time to clamp one single CNT, while the method described previously with PEDOT:PSS produces multiple piezos with many CNTs in a faster way in a single batch. Since it was not possible to restrict the amount of Pt that solidifies at the base of the nanotube, nor impede that certain mass of Pt reaches higher areas of the fiber, the preparation of free-standing fibers using the FIB technology was discarded and the method with PEDOT:PSS was then applied during the entire course of the project.

4.2 The Dynamic Scanning Electron Microscopy technique

The Dynamic Scanning Electron Microscopy Technique (DySEM) was developed by Schröter et al. [26, 27, 93] and it was first applied to atomic force microscopy cantilevers presenting high contrast circular shaped structures on its surface. By using this configuration, the basic principle was to convert the physical information contained in mechanical signals, such as a shift in the frequency, or in the amplitude and phase into data about the mechanical properties of a material, like bending behavior for example. This technique also enables the control and detection of a change in a system variable, such as mass, by monitoring the frequency of an oscillating device. This is particularly important to acquire reliable information about the dynamics of micro- and nano-electromechanical systems (MEMS/NEMS), whose functionality depends on resonance frequencies and are widely used as sensors in the chemical industry. In addition, the sensitivity of sensoring systems can be significantly improved by optimization of the vibrating structures. With the aid of the Euler-Bernoulli beam theory, this technique can potentially be extended to describe the bending properties of nanometric oscillating beams, with known density and that are electrically conductive materials.

The DySEM technique comprises of four main devices: a scanning electron microscope, a piezoelectric drive, a function generator and a lock-in amplifier (LIA). The scanning electron microscope has a high voltage electron beam gun that launches accelerated electrons on the surface of the object to be analyzed. The interaction of electrons with the sample generates a variety of signals, such as secondary electrons. These electrons are collected with the aid of a detector during the scanning along the surface of the sample, forming an image mixing the information of the morphology and the topography of the sample. The piezoelectric holder placed inside of the SEM is driven by an external function generator, which provides sinusoidal excitation over a range of frequencies inducing vibration. Combining simultaneously the imaging and the search of the resonance modes of the specimen by scanning the frequency requires one more device to complete the DySEM operation cycle. This device is the lock-in amplifier, which is synchronized to the sinusoidal voltage and though is able to detect those components of the secondary electrons detector signal of the vibrating fiber. As a result, the trio frequency, amplitude and phase can be recorded. In other words, the lock-in amplifier is responsible for demodulating the analog signal from the secondary electrons detector, strongly suppressing the noise and other non-synchronous signal components. The signal-to-noise ratio and sensitivity depends on the chosen integration time.

4.2.1 Electron microscopy imaging and lock-in amplifier analysis

For the dynamic imaging during the experiments on the course of this work, mainly a tungsten thermionic emitter SEM of type EVO MA 10 (Carl Zeiss Microscopy GmbH, Jena, Germany) from BAM was used. This SEM was satisfactory for the entire SiC NWs investigation, but for a better assessment of the multi-walled carbon nanotubes, an ultra-high-resolution SEM of type SU8230 with in-lens detector (Hitachi High-Tech Europe GmbH, Krefeld, Germany) was also employed. A SEM must provide sufficient resolution to image the fiber under excitation and to measure its shape and diameter. For accurate diameter measurement, the achievable pixel resolution of both SEMs was better than 1/10 of the fiber diameter. It reached 3 nm for the Zeiss and 1 nm for the Hitachi instrument. It is essential that the vacuum chambers of the SEM provided a BNC/SMB electrical feedthrough to input the piezo driving voltage supplied by a lock-in amplifier. The SEM also must permit to connect to the analogue output signal of the secondary electrons (SE) detector (type Everhart-Thornley) to the LIA using a signal splitter. In this work, a HF2LI 50 MHz with a built-in oscilloscope lock-in-amplifier (Zurich Instruments AG, Zurich, Switzerland) was used for the signal modulation.

The morphology of nanofibers was assessed in detail with a transmission electron microscope (TEM) of type JEM-2200FS (JEOL Ltd., Akishima, Japan) equipped with an in-column energy filter (Omega-type). Zero-loss conventional bright field imaging (BF-TEM) was conducted at acceleration voltages of 80 and 200 kV, with an energy window of 35 eV. To analyze the same samples that had been tested standing free on the top edges of the quartz crystals, the piezo unit had to be adapted to the size-restricted sample holder of the TEM.

The used CA- 301 resonator crystal is used in integrated circuits as a clock generator, for this it is operated either in the fundamental mode or the third mode. The corresponding frequencies are never reached in our application (12 MHz, ~ 50MHz) and on the contrary they would possibly be harmful for piezo and fiber bonding. Because of higher current consumption in the resonance, it would come to a temperature rise, which is only badly dissipated in the vacuum of the SEM. The piezoelectric material itself, as far as it can be deduced from data sheets of the vendors, moves around some picometers per volt of excitation voltage, in this work for example, around 10-20 pm for the 10 V used. The resonances not used for operation as a clock are determined by the geometry of the blank, less by the material itself. Not operating the piezo in resonance has several advantages. First, power consumption would increase greatly for a deflection that is not needed. In doing so, the piezo would become warm and would lead to thermal drift in the SEM, at the very least. In addition, the resonant modes of operation are very small in frequency and fibers already bonded might have to be rebuilt if the resonances of the piezo and the fiber do not match. This approach accommodates an important idea derived from the method itself: for the determination of bending stiffness, knowledge of the excitation amplitude is as unimportant as knowledge of the response amplitude. Only the frequency counts.

Reliable detection of fiber resonance modes by image signal analysis requires sufficiently high signal-to-noise ratios. This was achievable for fibers standing free on an edge of the quartz imaged in front of a dark background. For fast and sensitive frequency sweeps with the LIA,

necessary for reaching frequencies as high as 5 MHz, only the tip of a fiber was imaged with a reduced frame image mode presenting an average scan line time of 35 ms. That permitted SEM frame rates above 30 Hz. The SE detector output signal of these image frames was submitted to the LIA analysis. A schematic diagram of the experimental setup is shown in Figure 27.

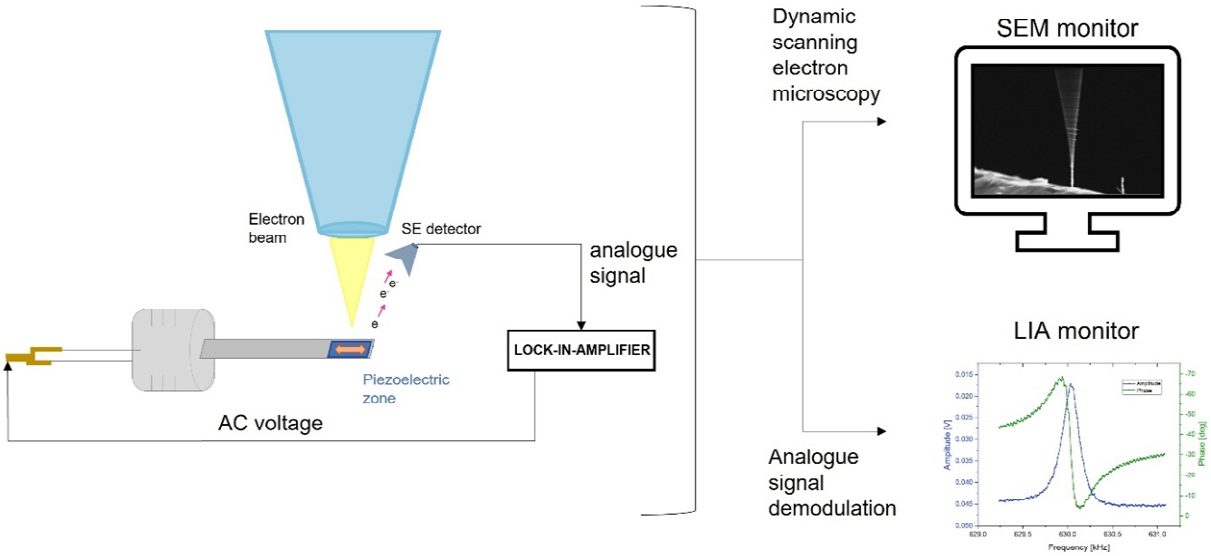

Figure 27: . Experimental setup of the dynamic scanning electron microscopy (DySEM) technique used to measure the resonance frequencies of nanofibers.

4.2.2 Estimation of resonance frequencies and Young's modulus

In order to provide supplementary data regarding the behavior of the nanotubes, which were the first samples to be tested, a theoretical approach was implemented. Prior to the experimental search of the fiber's resonance with the DySEM, the selection of the frequency range to use in the first experiments was estimated by our project partners from BAuA with the help of two-dimensional parameter plots. The values of resonance frequencies were estimated for the first and second mode of a MWCNT with a fixed length of 10 μm, having the Young's modulus and the diameter as variables (Figure 28a and b). For the other category, the frequency values were dependent on the length and diameter of a MWCNT with a fixed Young's modulus of 60 GPa (Figure 28c and d). The resonance frequency range was illustrated with a color spectrum.

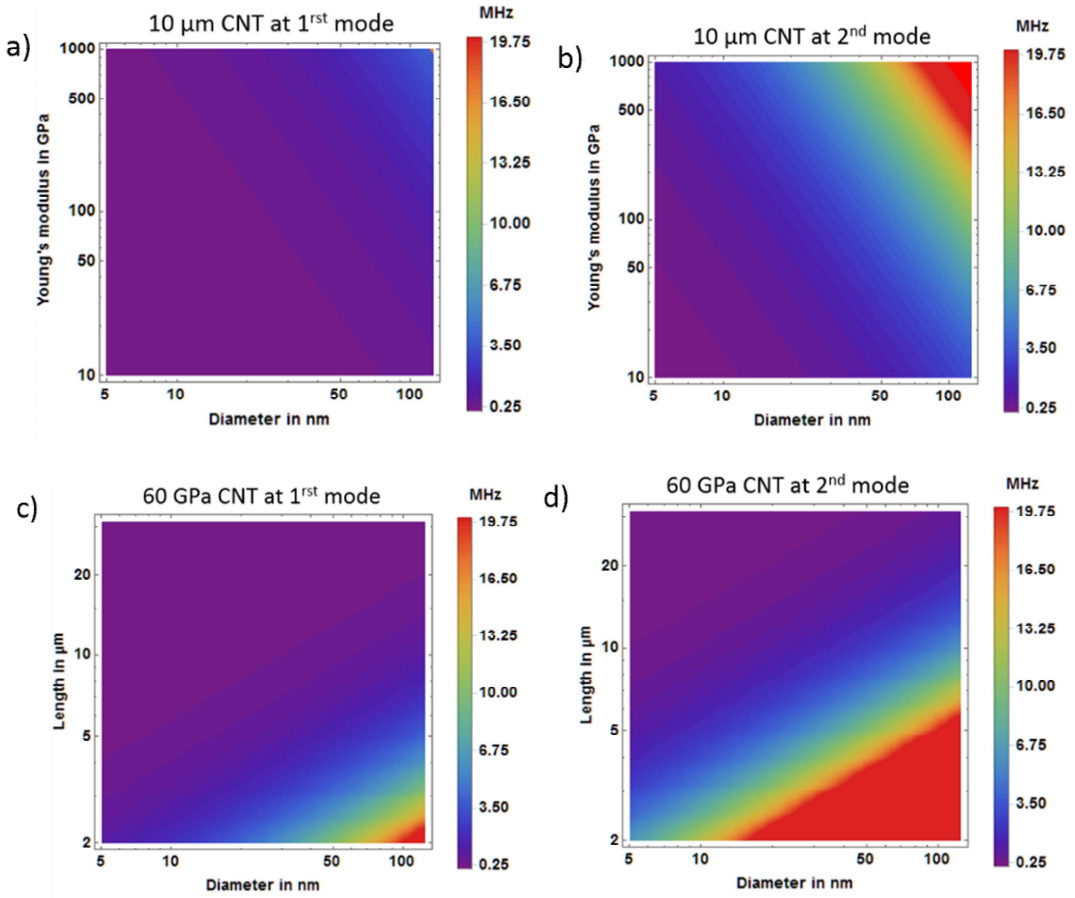

Figure 28. Examples of the theoretical estimations for the resonance frequency ranges of the carbon nanotubes. The color spectrum shows the range of resonance frequencies and Young's modulus E_Y for carbon nanotubes (CNTs) 10 µm long at: (a) first and (b) second modes; and resonance frequency ranges for CNTs with a predefined Young's modulus of 160 GPa at: (c) first and (d) second modes (d). Image extracted from the paper [92, 94].

With the aid of such study, the time used in the initial experiments was significantly optimized. Since most of the evaluated MWCNTs presented an average length of around 10 µm with diameters above 50 nm, a piezoelectric crystal with a resonance frequency of 12 MHz could be operated mostly below its resonance for detecting the resonance modes of the nanofibers. For a free-standing fiber in the SEM focus, the length and thickness were roughly determined to estimate the range at which the frequency of its first mode was located. For this first estimation, a modulus of 60 GPa was assumed. For the resonance search, frequency sweeps were performed from lower to higher frequencies around this frequency, having a low resolution of data points. Once the signal of the first resonance mode was identified by the LIA analysis, the number of data points of the frequency sweep was increased to enhance the precision of the detected resonance. Next, the dimensions of the fiber were verified, followed by the calculation of the Young's modulus using Equation 2.63. To estimate the resonance frequency for further modes, the calculated modulus was used directly in Equation 2.62 in order to estimate the resonance frequencies for further modes. For a perfect linear elastic beam, the Young's modulus is constant. Another possible measure to obtain the further mode is by using the ratio $\nu_2/\nu_1 = 6.27$. Finally, the frequency sweeping range was adjusted and refined. This procedure was then conducted to each individual freestanding fiber fixed at the edges of the driving piezo.

4.2.3 Error estimation

The measurement error of the fiber length (L) within the SEM depends on the pixel resolution but will be dominated by the geometric length determination error for a fiber of arbitrary orientation in three-dimensional space from two orthogonal SEM views (projections).

If we consider independent individual errors, the error ΔE_m of the Young's modulus E approximated for small inner diameters D_i in Equation 2.63 can be written as the quadratic mean of relative errors, as follows:

$$\Delta E_m = \underbrace{\frac{64\pi^2}{k_m^4} \cdot \frac{L^4\, \rho\, \nu_m^2}{D^2}}_{E_m} \cdot \sqrt{\left|\frac{\Delta\rho}{\rho}\right|^2 + \left|2\,\frac{\Delta\nu_m}{\nu_m}\right|^2 + \left|2\,\frac{\Delta \mathrm{D}}{D}\right|^2 + \left|4\,\frac{\Delta \mathrm{L}}{L}\right|^2} \tag{4.1}$$

For the flexural rigidity, the error ΔR can be similarly calculated as:

$$\Delta R = \underbrace{\frac{2\pi^3}{k_m^4} \cdot L^4\, \rho\, \nu_m^2\, D^2}_{R} \cdot \sqrt{\left|\frac{\Delta\rho}{\rho}\right|^2 + \left|2\,\frac{\Delta\nu_m}{\nu_m}\right|^2 + \left|2\,\frac{\Delta \mathrm{D}}{D}\right|^2 + \left|4\,\frac{\Delta \mathrm{L}}{L}\right|^2} \tag{4.2}$$

5. Results and Discussion

5.1 Fiber clamping

For fiber length measurement and interpretation of resonance frequencies, it was important to localize the immobilization point of a fiber where it penetrates the PEDOT:PSS layer. For fibers at rest, the footing point was not always easy identifiable by SEM inspection. Fiber resonances helped to track the fiber down to the immobilization point, where no displacement must be observable. For high accuracy measurements, improper clamping to the piezo actuator must be ruled out. Shaky movements of only loosely attached fibers do not allow interpretation in the Euler–Bernoulli framework. A good indication of the stability of the clamping is the constancy of the measured vibration response, which was present in all cases.

The electrical conductivity of the PEDOT:PSS polymer was found to be sufficient for electrostatic precipitation and SEM imaging. It showed good wetting behavior for CNTs [95], as is required for embedding and mechanical fixing the fiber base. The rigidity of the PEDOT:PSS film supposedly affects the damping of fiber oscillations, resulting in reduced amplitudes by dissipation for a soft polymer. Mechanical properties of PEDOT:PSS were still satisfactory when dried. With 1.7 GPa, PEDOT:PSS reached only about 50% of the stiffness of commercial epoxides [96, 97]. The mechanical loss tan δ (the ratio between the loss modulus E'' and the storage modulus E' for polymers) of PEDOT:PSS – which is also a measure for

damping - for low frequencies at room temperature is 0.06, before the polymer is completely dried under ambient conditions. Assuming that adsorbed water is removed in vacuum, tan δ will drop to 0.03 [98]. The highest loss factor of tan δ = 0.14 was observed at 65 °C and can be considered as the worst case under wet conditions. Heating the surface and the fiber during beam exposure could remove water and lower tan δ further to a value of 0.04, which is not high, but still the intrinsic loss in the polymer contributes to the damping in the system. The effect of the clamping conditions on the natural frequencies detected upon the excitation experiments is discussed in Section 5.5.

Using a more rigid metallic material to fix the fibers on the piezo would reduce the dissipation of the mechanical vibration. For this reason, an attempt to test the resonance frequency of a carbon fiber (Tenax®-E HTS45, produced by Tojo Tenax; specification in Table 4) was made using a 12 MHz piezo with a layer of Field's metal. The Field's metal is an alloy composed of bismuth:indium:tin (32.5:51:16.5 wt%) with a melting point of 61 °C, and Young's modulus of ~ 10 GPa [99, 100]. This way, it worked as a conductive film that remained sufficient viscous in a relatively low temperature, enabling the attachment of the fibers before it solidifies. Once solid, it would provide a stiffer clamping than the PEDOT:PSS polymer. The high electrical and thermal conductivity together with high mechanical stiffness of alloys could be beneficial for imaging fiber oscillations with SEM. The carbon fiber was selected for this trial, as it can be handled macroscopically and with simple personal protective equipment, differently than with nanotubes., which requires special chamber configurations and cannot be individually selected in a macroscale operation setup. A similar test was performed with gallium as well (melting point at 29 °C), however it was noticed that at ambient conditions the film was still viscous and remained viscous during the DySEM analysis, not being suitable for the resonance detections.

Table 4: Specification of the carbon fibers Tenax®-E HTS45

d	7 μm
ρ	1770 kg/m3
E	240 GPa

For the fixation of a carbon fiber, the Field's metal was heated over 62 °C with hot air and then applied on a piezo surface. While it was still viscous, a carbon fiber was carefully placed on the Field's metal surface having most of its length projected outside of the piezo over the edge. Next, the piezo was let at rest for 5 hours under ambient conditions in order for the metal to solidify entirely. After the complete solidification, the piezo with the carbon fiber was subjected to the excitation tests. The first and the second mode of the carbon fiber were detected, and the results are shown in Table 5. The point at which the fiber connected to the solidified metal film is shown in detail in Figure 29 (a) and (b). The vibration of the fiber at the first mode is shown in Figure 29 (c).

Table 5: Experimental (v_{exp}) and theoretical (v_{th}) values of the resonance frequency measurements of one carbon fiber on a Field's metal film. The theoretical values were calculated using ρ and E from the fiber specification and the diameter (D_{exp}) and length (L) were measured during the experiment. The Young's modulus found experimentally is described as E_{exp}. The error in the Young's modulus was calculated as 15.4%.

D_{exp} (μm)	L (mm)	ν_{exp1} (kHz)	ν_{th1} (kHz)	ν_{exp2} (kHz)	ν_{th2} (kHz)	E_{exp1} (GPa)	E_{exp2} (GPa)	E_{esp} (GPa)
6.365	1.511	3.817	4.541	23.462	28.460	167 ± 44	163 ± 7	240

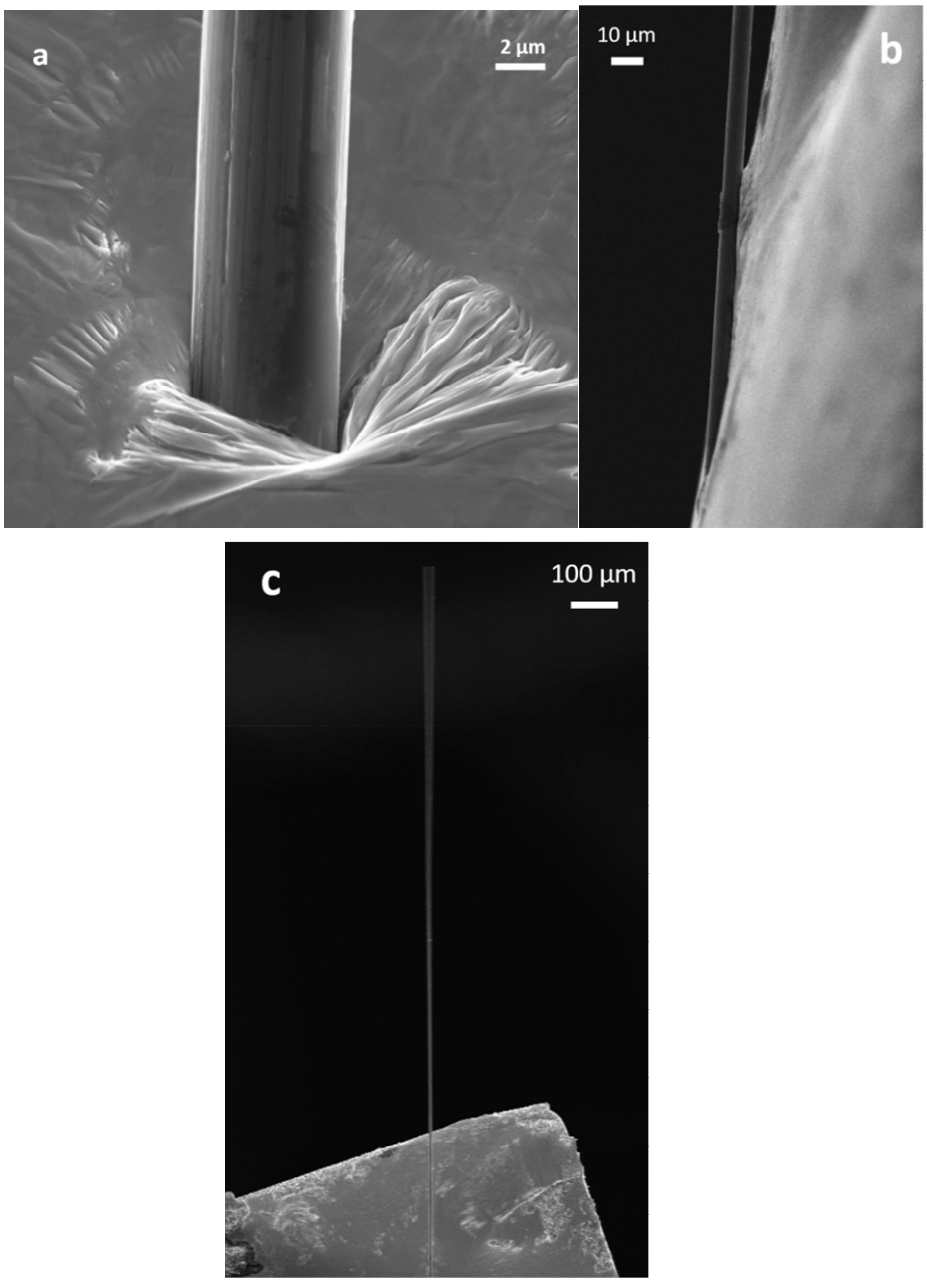

Figure 29: SEM images of a carbon fiber fixed on a solidified Field's metal film. Image (a) shows a detailed front view of the connection of the base of the fiber to the alloy, and image (b) shows a side view of the base of the fiber, where it is possible to notice the exact point at which the fiber is embedded in the film. In image (c), the carbon fiber is vibrating at the first mode of resonance.

The values of experimental Young's modulus found at first and second modes are similar, which shows that the carbon fiber acted like a beam with a linear mechanical behavior. However, the differences between the experimental and the theoretical values of *E* are related to errors in the projected length of the fiber, the presence of impurities along its length, which changes the mass and the density of the fiber, the quality of the fixation point, and especially the high amount of mass from the Field's metal deposited on the piezo, which impairs the amplitude of vibration of the piezo and implies in dissipation of energy. For a more accurate measurement of the fiber length and a deeper evaluation of the condition of the fixation point, the piezo was tilted ninety degrees from horizontal to vertical position and a better view of the exact first contact point was obtained (Figure 29b). As can be seen in Figure 29a and b, the base of the fiber is not fully covered by the metal and this leads to vibration damping, because of free areas where the vibration can dissipate right on the base of the fiber. In addition to the damping, an effect that can occur is a softer stiffness compared to "rigid" clamping. A stronger clamping is achieved when the fiber has its base completely embedded in the metal film.

From this experiment, it was concluded that Field's metal could be used as an alternative to the PEDOT:PSS and to the gallium, for fixing nanofibers on the piezo in an atmosphere above 60 °C, as long as only a thin film of metal covers the piezo. The Field's metal has a low melting point, it solidifies rapidly at ambient conditions, and it has good wettability on the piezoelectric quartz. As the fibers to be tested are in nanometric scale, a small contact point on the film would result in a desirable strong clamping for the excitation measurements. In addition, a controlled deposition of a thin layer of the metal on the surface of the piezo would be sufficient for the fibers to attach and would not cause much counterweight on the amplitude of vibration of the piezo.

5.2 MWCNTs

5.2.1 Determination of the dimensions of the nanotubes

The commercial NM-401 used in this work are characterized in the technical report as straight-wall MWCNT material. However, all of the nanotubes samples investigated showed a bended and slightly curved morphology, rather than rigid and straight configurations, as can be seen in Figure 17 from Section 3.1.1 and in Figure 30 below.

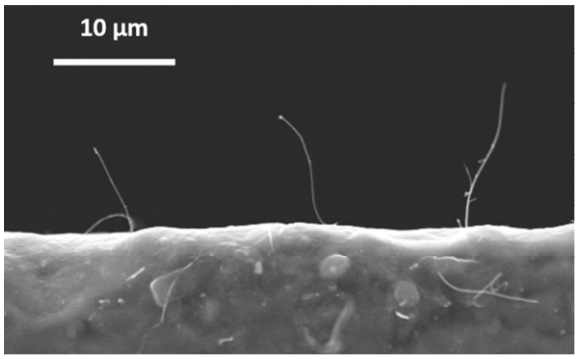

Figure 30: MWCNTs type NM-401 used in this work standing on the edge of a piezo fixed by the PEDOT:PSS polymer film. Image published in [92]

This made it a challenge to obtain accurate dimensions by SEM metrology, especially of the length L. Since the calculation of the Young's modulus E from Equation 2.63 depends on the 4th power of the length, it is crucial to determine this value as exact as possible to minimize errors of the Young's modulus in Equation 2.63. For this task, an ultra-high-resolution SEM SU8230 with in-lens detector was used. However, the images obtained only showed the apparent fiber length in a two-dimensional projection. For a curved fiber oriented in three-dimensional space, a second, orthogonal view was required to determine the true fiber length. The two orthogonal projections were obtained by tilting the sample holder in approximately ninety degrees so that the fiber could be imaged from the side. Figure 31 (a – f) shows examples of the two orthogonal projections for three different MWCNTs. The highest length acquired from the two projections was then selected as the fiber "official" length.

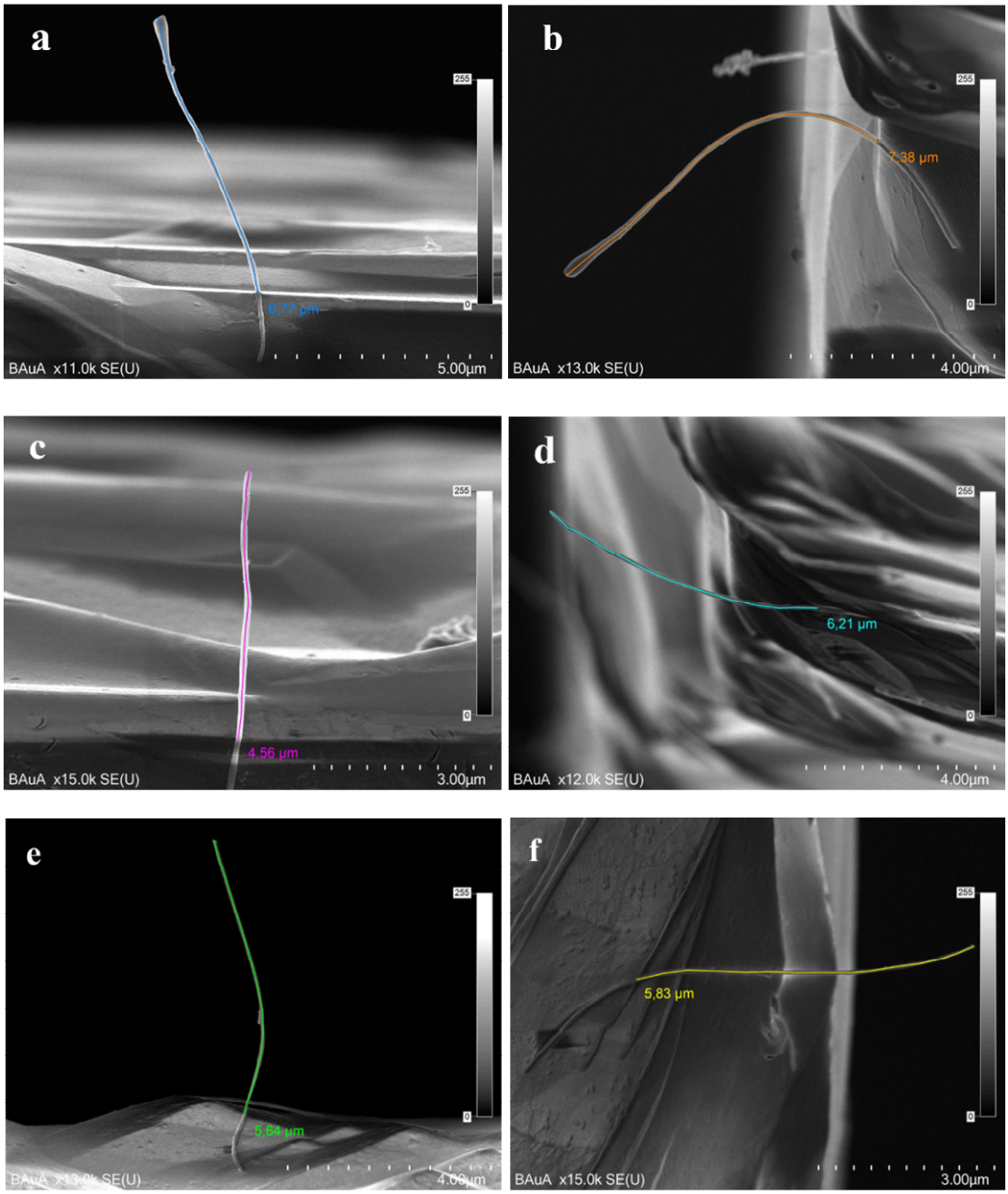

Figure 31. High resolution SEM images of the length determined from two different projections of the three different MWCNT: (a) the front view gives a value of 6.77 µm and (b) the side view shows a visibly higher length of 7.38 µm; (c) the front view image shows 4.56 µm of length and (d) the side view presents the same fiber with 6.21 µm of length; (e) the front view length is 5.64 µm and (f) the side view length is 5.83 µm. The SEM images were obtained at BAuA with a High resolution SEM Hitachi SU8230 and the in-image measurements were performed with the software Olympus IMS at ZELMI – TU Berlin. Images a and b were published in [92]

The measurements of the MWCNTs diameter were made on the course of the experiments with the ultra-high-resolution SEM SU8030 (Hitachi), using the fiber width measurement tool from the SEM software. The diameters were determined from the mean value of four selected points along the length of the nanotubes, since their thickness was irregular (Figure 32). The accuracy of these measurements is as important as the accuracy in determining correct values of the length because the flexural rigidity (R) is directly dependent on the diameter to the 4th power (Equation 2.64). In addition, the diameter value impacts on the Young's modulus, as

well. Therefore, imprecise measurements of the diameters would impact considerably on the reliability of the rigidity data collected.

The MWCNTs presented an average diameter of 98 nm, while the NM-401 from the European JRC were characterized with an average diameter between 70 and 80 nm. Thicker nanotubes are obtained when the catalytic chemical vapor deposition is made at higher temperatures (from 750 °C on), as described by Kumar and Ando [101]. However, since we did not have access to the technical details through which our samples were produced, it is not possible to confirm why the MWCNTs tested were considerably thicker than the NM-401 specified.

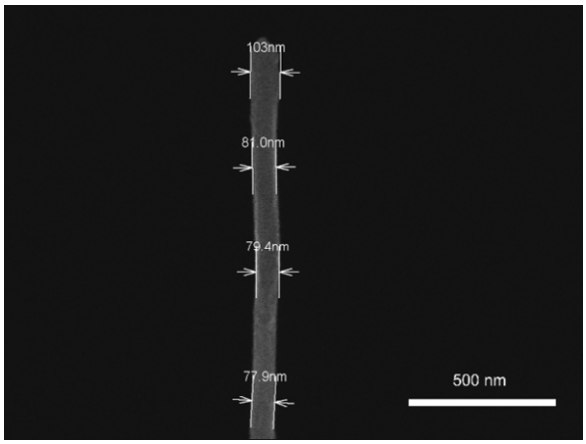

Figure 32. SEM image of a MWCNT showing the thickness collected at four different points of the fiber for the determination of the average diameter (SEM Hitachi, SU8030).

5.2.2 Young's modulus measurements of MWCNTs

The resonance frequencies for a set of MWCNTs were successfully detected using the dynamic scanning electron microscopy technique and the corresponding Young's modulus were determined via the Euler-Bernoulli formula. These nanotubes presented assorted E from 15 to 161 GPa with an average error of 13% (Figure 34a). The values of resonance frequencies, the dimensions of the nanotubes and the Young's modulus obtained with the experiments are presented in Table 6. For half of the nanotubes tested, both first and second modes of resonance were detected. For the other half, only the resonance at first mode was identified. For these cases, most likely the resonances of the nanotubes deviate slightly from the theoretical values and in order to identify further modes it would be necessary to perform experiments with longer periods of time. Images showing the vibration of MWCNTs at the first and at the second mode of resonance are shown in Figure 33.

Table 6: Young's modulus of MWCNTs produced by chemical vapor deposition. E_1 is the Young's modulus determined from the first mode and E_2 is the bending determined from the second mode, according to Equation 2.63. The estimated experimental errors are ± 3 nm for D, ± 200 nm for L and ± 1 kHz for ν_1 and ν_2. We neglect the inner diameter D_i for its contribution is very small for the MWCNTs studied here due to the 4th power dependence in the second moment of area: $(D_i/D)^4 \ll 1$. The theoretical ratio between the non-dimensional resonance frequencies β_2^2/β_1^2 equals $\nu_2/\nu_1 = 6.267$ (see Section 2.2.1). E specifies the weighted average of E_1 and E_2.

MWCNT	*D (nm)*	*L (μm)*	ν_1 *(MHz)*	ν_2 *(MHz)*	ν_2/ν_1	E_1 *(GPa)*	E_2 *(GPa)*	*E (GPa)*
1	85	6.00	1.563	-	-	40 ± 6	-	40 ± 6
2	89	6.42	2.862	-	-	161 ± 25	-	161 ± 25
3	90	14.09	0.583	3.434	5.89	152 ± 16	135 ± 14	143 ± 15
4	91	17.99	0.198	1.298	6.56	46 ± 4	50 ± 5	48 ± 5
5	95	10.78	0.867	4.699	5.42	103 ± 12	77 ± 9	90 ± 10
6	96	14.17	0.404	-	-	66 ± 7	-	66 ± 7
7	97	5.89	2.422	14.521	6.00	69 ± 11	63 ± 10	66 ± 11
8	100	7.38	0.750	4.755	6.34	15 ± 2	16 ± 2	15.5 ± 2
9	107	8.76	1.287	-	-	79 ± 10	-	79 ± 10
10	127	8.24	1.655	-	-	73 ± 9	-	73 ± 9

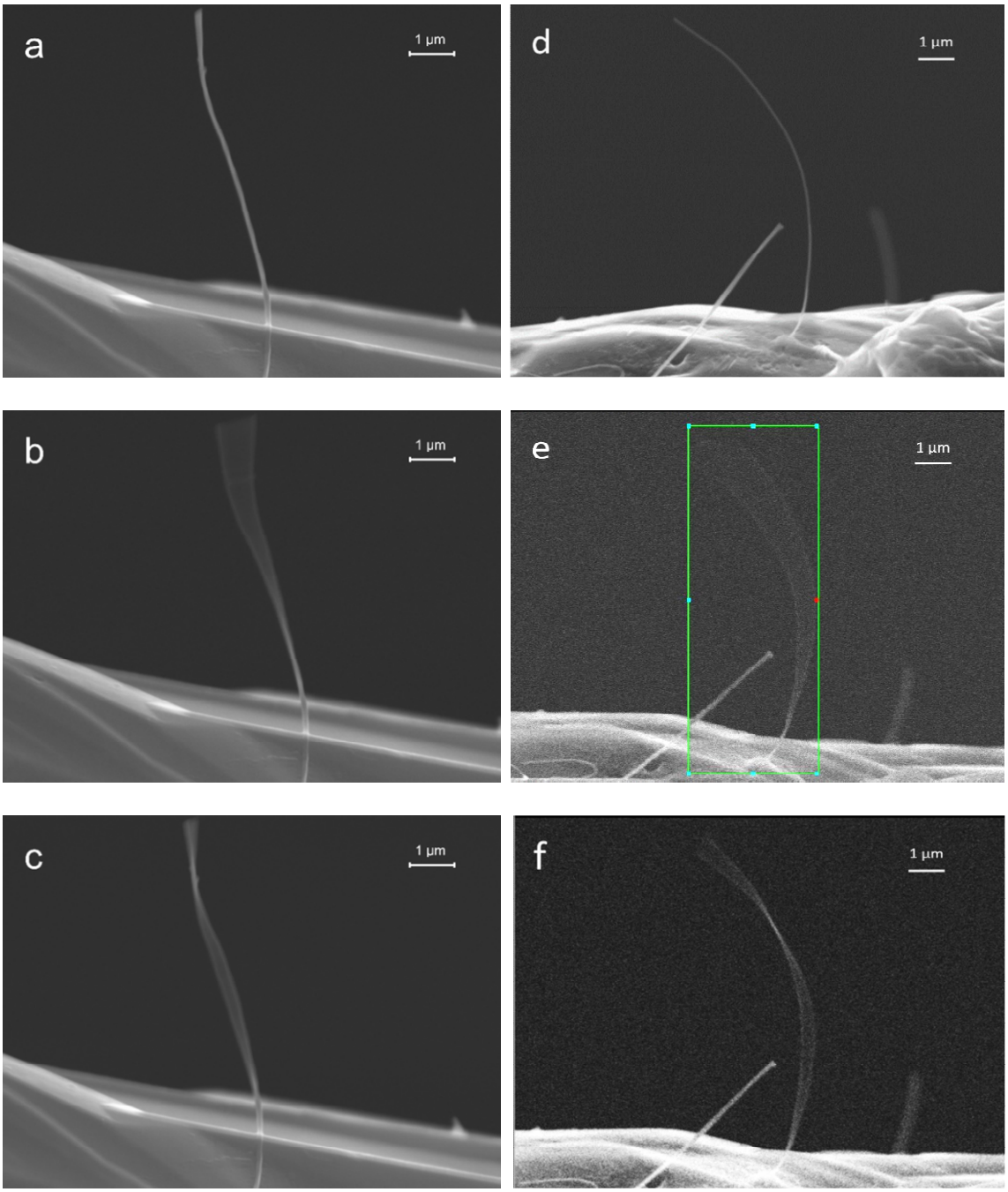

Figure 33: DySEM images of two different MWCNTs under excitation, one nanotube is shown on the left column and the other on the right column; (a, d) the nanotubes are at stationary mode; (b, e) the nanotubes are vibrating at the first mode and (c, f) the nanotubes are vibrating at the second mode. Images from the left column were published in [92]

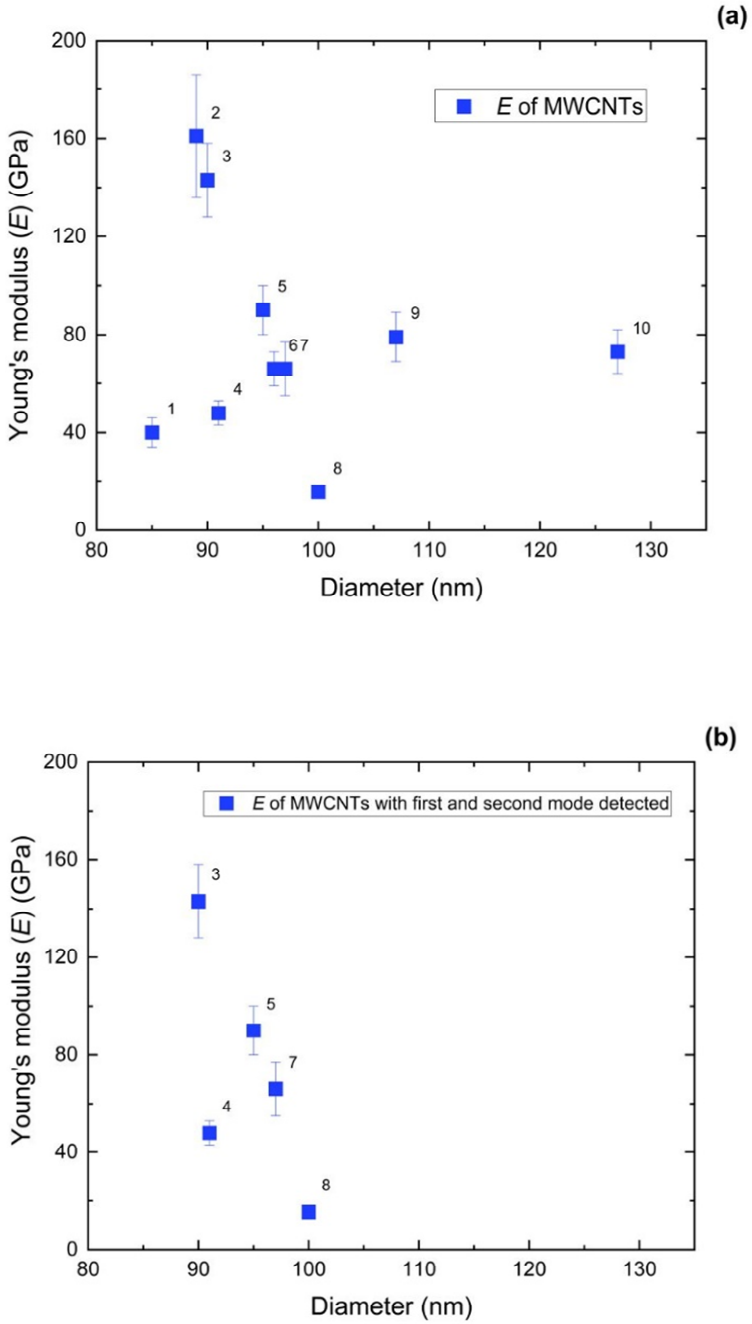

Figure 34: Graphs of the Young's modulus values *E* vs. diameter *D* for the NM-401 MWCNTs tested in this work. Graph (a) shows all the results presented in Table 6, and Graph (b) highlight the nanotubes that exhibited resonance at first and at second mode of vibration.

For the nanotubes tested in this work no correlation between the dimensions of the nanotube and the value of the Young's modulus was observed, since for the thinnest nanotubes, a variation of low and high modulus were obtained and the same occurred for the shortest ones. The assorted and relatively low values of Young's modulus have been observed by other authors that investigated MWCNTs produced by catalytic chemical vapor deposition as well. In previous studies, differences in Young's modulus values for the same batch of nanotubes have been related to several structural and morphological characteristics including

structural inhomogeneity such as the presence of defects, curved vs. straight fiber shape, non-uniform mass distribution and irregular nanotube dimensions [2, 3, 7, 10, 11, 102, 103]. These characteristics were observed for the nanotubes tested here and can be seen in detail in the transmission electron microscope images (Section 5.2.4). The remarkable high values of Young's modulus that made carbon nanotubes very popular have been reported for straight uniform nanotubes produced by arc-discharge and mainly with diameters smaller than 50 nm **(**Table 2**)**. Besides presenting regular shape characteristics, the nanotubes produced by arc-discharge have a higher degree of crystallization, granting more rigidity to these tubes.

In [6], Wang et al. found a remarkably low Young's modulus of 2.2 GPa for a MWCNT that, although it was produced by arc-discharge, exhibited volume defects along its body, impairing considerably its stiffness. In [104], the authors showed that volume defects and attached masses affect the Young's modulus less or more, depending on the position of them on the nanotube length and also argue that curly shapes also contribute to the decrease of the stiffness. Jackman et al. [11], compared the Young's modulus of MWCNTs produced by arc-discharge and CCVD and associated the distinct bending behaviors of the two types of nanotubes to the difference in crystallinity, which is higher for arc-discharge produced MWCNTs.

5.2.3 Influence of an extra mass on the detected resonance frequencies

Most of the nanotubes investigated presented highly evident attributes of heterogeneity, such as the MWCNT of Figure 35. Discarding these fibers was not taken into consideration, due to the limited number of samples to test. As discussed above, the heterogeneity on the morphology of the fibers, and the presence of defects lead to a high scatter and especially low values of E. The non-uniformity of mass distribution along their bodies and accumulations of extra masses at particular positions along the fiber length are considered critical for applying the continuum mechanics theory of Euler–Bernoulli. As Equation 2.59 is based on a perfect uniform and straight beam, it is important to analyze the consequences of imperfections of the shape on the resonance frequencies and consequently on the Young's modulus (Figure 35). Therefore, a finite elements simulation of a hypothetical fiber was performed by our partners at BAuA to evaluate how the presence of a spherical mass would influence the vibration behavior of a nanofiber similar to a carbon nanotube.

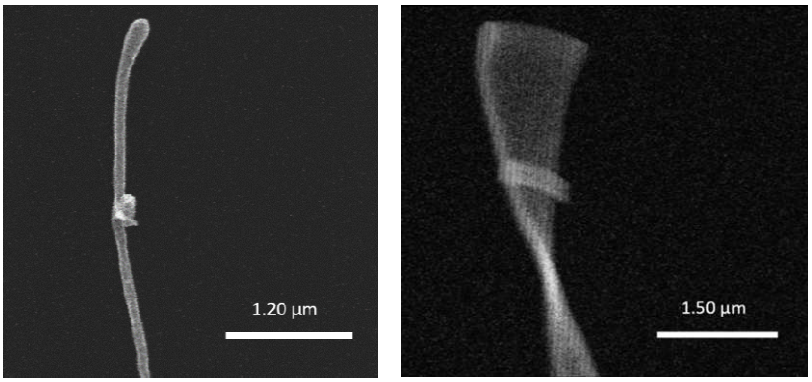

Figure 35: A SEM image of a MWCNT from the group of nanotubes tested, which presents a volume defect in a region proximate to a vibration node. This nanotube is vibrating at the second mode of resonance.

For such simulation, a carbon nanotube 1 µm long and 75 nm thick was considered. The Young's modulus was fixed at 60 GPa and the attached matter was simulated in at half the length and at the tip of the tube (Figure 36b, and Figure 36c, respectively).

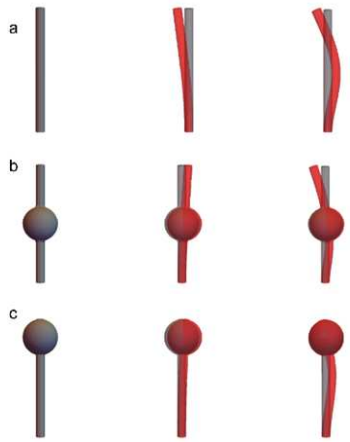

Figure 36: The red fiber represents the nanotube under excitation. The first column is at null excitation, the second column refers to the first mode and the last column to the second mode. (a) a perfect straight and uniform carbon nanotube; (b) with a spherical mass at half the length of the nanotube's body; (c) and at the tip. The simulation showed that an extra mass located at the center of the tube has a smaller impact on the resonance frequencies than a mass at the tip. Image created by Dr. Asmus Meyer-Plath from BAuA and published in [92].

The simulation showed that the vibration behavior of a nanotube is strongly affected by an extra mass present along its length. At the first mode of excitation, the resonance frequency is reduced in ~62% for a mass at the tip and in ~29% for a mass in the middle . This is attributed to the fact that the influence of extra masses depends on the dynamic shape of the vibrating fibers, which again depends on the type of excited mode. The resonance frequency at the second mode is less affected by the extra mass, with deviations of ~1% and ~27%, for the mass in the center and on the tip, respectively (Table 7). This is an important reason why it is necessary to identify further modes. This phenomenon occurs because most of the energy in the system is transferred to the tip during the excitation at the first mode, therefore, a mass deposited in the region close to the tip will significantly impair the natural excitation. For the

excitation at second mode, the extra mass attached at the center is possibly close to a region of almost null amplitude of vibration, such as for example approximate to a node. For this reason, the resonance is altered by only 0.8%.

Table 7: Values of resonance frequencies at first and second mode obtained from finite elements simulation for a CNT. The second column shows the frequencies of a pristine CNT; the third column presents the resonances of a CNT with an extra mass in the middle length; and the last column shows the resonances for a CNT with a mass at the tip. The percentage values refer to the frequencies of the pristine CNT.

Eigenmode	No Extra Mass	Mass in the Middle	Mass on the Tip
1st mode	64 MHz	45.6 MHz (−28.8%)	24.6 MHz (−61.6%)
2nd mode	394 MHz	391 MHz (−0.8%)	288 MHz (−26.9%)

The Figure 37 below represents a simplified overview of the consequences of defects on the detected resonance frequencies. Considering a defect with a constant mass:

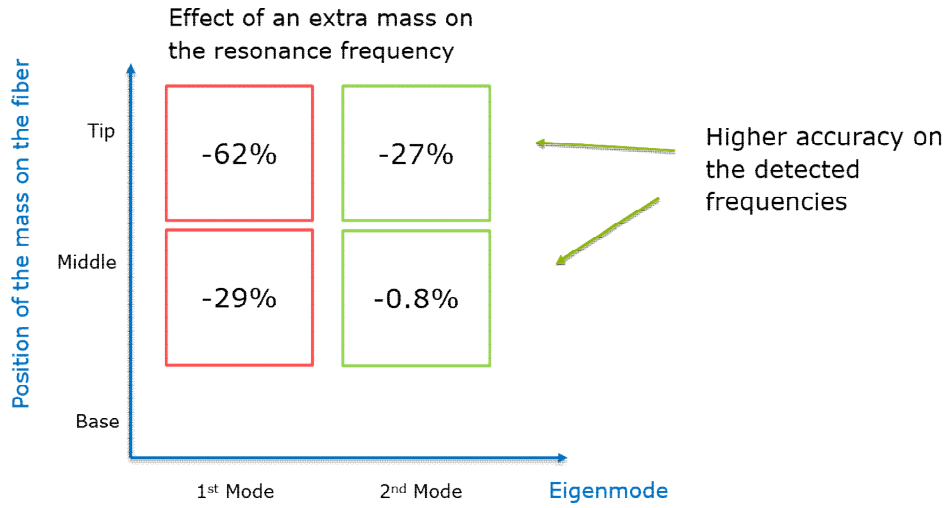

Figure 37: Graph showing the importance of the detection of further modes of vibration upon exciting nanofibers that are likely to exhibit volume defects along their length.

5.2.4 Characterization of the MWCNTs with transmission electron microscopy

In order to analyze the morphology of the nanotubes in detail, some samples of MWCNTs were observed in a transmission electron microscope (TEM) of type JEM-2200FS (JEOL Ltd., Akishima, Japan) at BAM, equipped with an in-column energy filter (Omega-type). Zero-loss conventional bright field imaging (BF-TEM) was conducted at acceleration voltages of 80 and 200 kV, with an energy window of 35 eV. To analyze the same samples that had been tested standing free on the top edges of the quartz crystals, the piezo unit had to be adapted to the size-restricted sample holder of the TEM. For that, the brittle piezo quartz crystal was carefully

cut on the bottom, in a location distant to the area where the nanotubes were fixed. This way, the ring that connects the electrical wires to the electrodes on the piezo quartz was detached and the remaining part, i.e., the tip of the piezo quartz containing the nanotubes to be analyzed, could then be placed on the TEM sample holder and characterized (Figure 38).

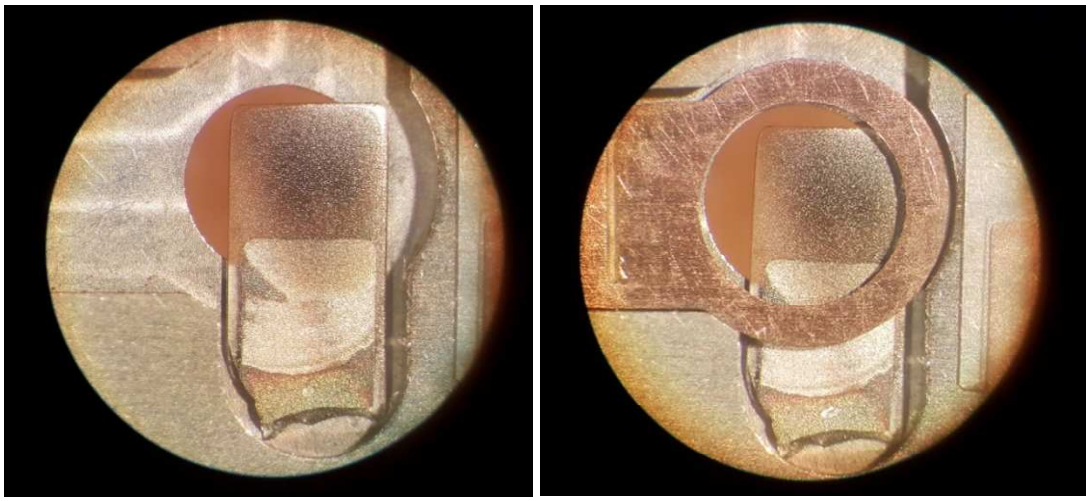

Figure 38: regular camera photographs taken through the lenses of an optical microscope showing two steps of the sample holder configuration. On the left image, the cut piezo was placed onto the TEM sample holder and on the right image, the area designated to be analyzed in the TEM is fixed with the TEM clamping tool.

The NM-401 nanotubes studied in this project are considered a benchmark material for toxicology studies. For this reason, it was important to test the samples provided by BAuA. Even though these nanotubes were tested via the method presented here and relevant data about their mechanical behavior was obtained, for the Euler-Bernoulli beam theory however, these nanotubes are not the most appropriate material to test, since their shape is not a perfect beam-like format. Nevertheless, the values of Young's modulus obtained for these nanotubes in this project are in accordance with the Young's modulus reported by other researchers for MWCNTs produced by catalytic chemical vapor deposition and tested via different types of methods (Table 2). The CCVD method renders nanotubes with non-regular diameters, less crystallinity, defects such as branching and misalignment of walls and some unknown structures, as shown in the TEM images in Figure 39. As can be seen in the bright field TEM images of different nanotubes from the same batch of the ones used in this work, our nanotubes had a wavy form (Figure 39a), presented defects such as branching (Figure 39b, c and d) and a disturbed structure (indicated by the dark areas in Figure 39d), and misalignment of walls (Figure 39e),. These aspects modify the rigidity of the fibers, since they generate weak points and are present in different ways from fiber to fiber, which explains the assorted values of E.

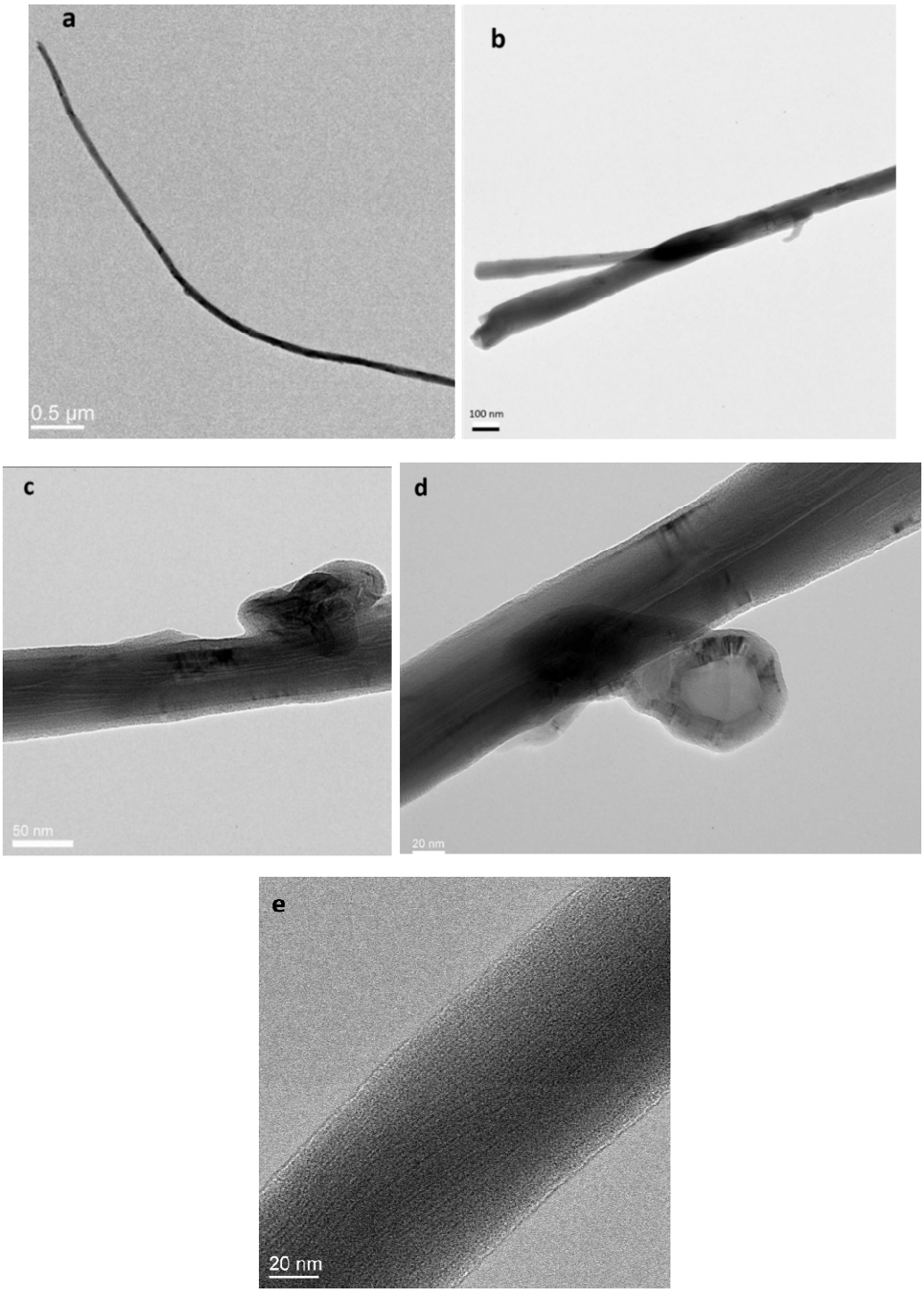

Figure 39: Examples of bright field TEM images of MWCNTs type NM-401 used in this project; (a) shows a curved nanotube; (b), (c) and (d) show some irregularities on the morphology, such as branches and non-uniformity of diameter; (e) shows the misalignment of the multiple walls.

5.2.5 Energy dissipation

In systems containing mechanical resonators, there are multiple potential sources of energy dissipation that are not always easily identified. Energy losses during the oscillation cycles in the system composed by the piezoelectric actuator, the polymer film and the CNTs would lead to the detection of damped resonance frequencies, which means that for very small amplitudes, the accuracy of the real resonance frequency value could become compromised,

and, in cases where the damping is significantly high, it could even impair the detection of resonance frequencies by the lock-in-amplifier. This occurs mainly when the vibration amplitude originated on the piezo is not fully transmitted to the nanotubes, because of several sources of energy dissipation. One is the presence of the gas pressure in the SEM chamber that, especially for nanoscale materials, increases the resistance to motion by aerodynamics effects. However, in a SEM, these effects are negligible. Another is the total mass deposited on the piezo, consisted by the layers of iridium, gold and PEDOT:PSS. The mass of the nanofibers is not taken into consideration here because of their miniscule dimensions. Other sources of energy dissipation are related to intrinsic mechanical losses of the components, as for example inner frictional processes between the walls in MWCNTs. Other factors can strongly affect the dissipation of energy in the system, such as the stiffness of the PEDOT:PSS and how much the fiber was embedded in the polymer film. Qin et al. demonstrated the effect of the clamping on the resonance frequency of a cantilevered nanowire by exciting it with different amounts of deposited material for clamping. As a result, the detected resonance frequency increased as the clamp area increased, until the clamp reached the optimum fixation condition [105]. In addition, it has been questioned in the course of the experiments, whether the damping has influence only on the vibration amplitude with which the nanofiber is excited, or if it impairs the detection of the true natural frequencies of the fiber as well. This has been very appropriately clarified in [105], where the authors showed that both the frequency and the amplitude increase when the damping is reduced in the system.

In this work, the quality factor Q was used to describe the damping related to the excitation of the nanofibers, and it was obtained experimentally during the resonance detection. The Q-factor is the ratio between the resonance frequency v_i and the full width at half maximum (FWHM) Δv from the Lorentzian fit of the frequency response function (FRF) of a single MWCNT resonance measurement [105-107]. A wide amplitude peak means that the vibration movement of the fiber was limited, not releasing most of the energy to the resonance vibration, dissipating it to other components of the system. And in this case, the quality factor is low, indicating higher energy dissipation. The higher and narrower is the peak, the greater is the quality factor because a very high amplitude of vibration was reached.

For the resonance detection of the MWCNT tested, Q = 85 (Figure 40). This value is within the range of quality factors reported by other authors for MWCNTs [2, 4, 10, 105, 108, 109]. However, for oscillatory systems, it is treated as a low performance process. This value of Q-factor might as well be associated with the position of the clamp along the fiber's length. This happens because during the oscillation cycles, the resonator might exert forces on the fixation point, which depending on the dimensions can become a source for energy loss. The ideal case to reduce damping is that the anchoring is made exactly on a vibration node. This way, the vibration is not impaired because the resonator can move freely. If the area of the fiber covered by the PEDOT:PSS film reaches higher points away from the base, it would invade a section of the fiber that takes part in the amplitude of vibration. If we would quantify the quality factor of the clamping itself as a function of the length l and the thickness t of the nanofiber, $Q_{clamping} \approx 2.17\ l^3/t^3$, as shown in [107]. For nanometric oscillators with high aspect ratio, $Q_{clamping}$ becomes exceptionally high, showing that the energy losses arising on the anchoring point between the nanotube and the substrate can be for some cases negligible.

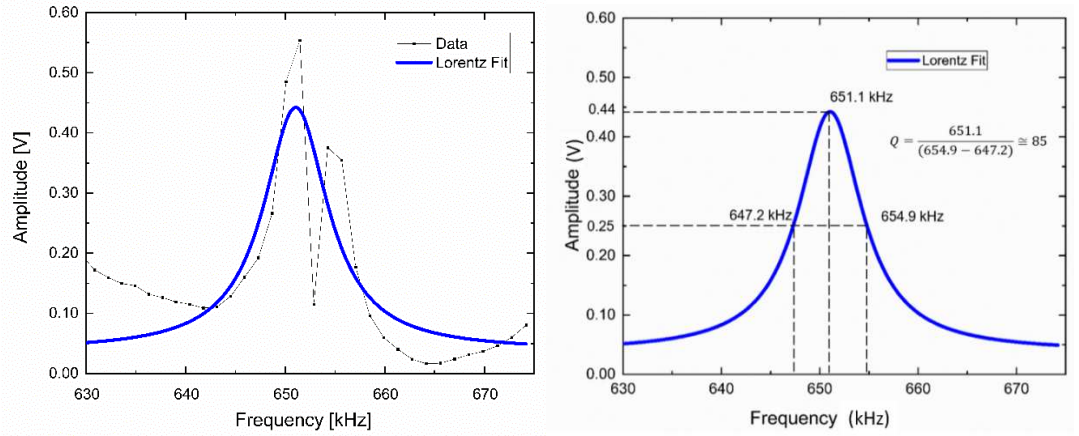

Figure 40: resonance frequency curve of a MWCNT: (left) Lorentzian fit of amplitude vs. frequency for the resonance frequency of a MWCNTs with D = 102 nm, L = 12 μm, E_1 = 82.1 ±16.4 and ν_1 = 651.1 kHz, where Q = $\frac{\nu_1}{\Delta\nu}$ = 85; (right) demonstration of the quality factor derivation Applied voltage of 10 V.

Analyzing the data points shown in the graph of amplitude vs. frequency from Figure 40 left, two peaks of resonance were observed. These peaks can be associated to two hypothetical causes: one is the existence of real and very close resonance frequencies in different directions, and the other is the hypothesis that the peaks were created as a result of noise and interference effects. To verify the existence of approximate resonance frequencies in two distinguished directions, more carbon nanotubes would need to be tested. However, these double peeks were not often observed in the group of nanotubes tested, and due to the poor variety of the samples and limitations on the resolution of the microscope, a deeper investigation on this matter was not possible on the course of this project. Therefore, here the presence of interference and noise were taken into consideration and for this reason the Lorentzian interpolation was applied.

Estimating the damping in an Euler-Bernoulli continuum system is a very complicated task. Thus, to be able to theoretically evaluate how a Q-factor of 85 affects the detected resonance frequency of a nanofiber, a simplified model is applied. In this model, the fiber is considered as a mass on a translational spring placed in a viscous fluid, as shown in Figure 41. In this approach, the whole model is reduced to a damped single-degree-of-freedom (SDOF) oscillator and only the first mode needs to be analyzed.

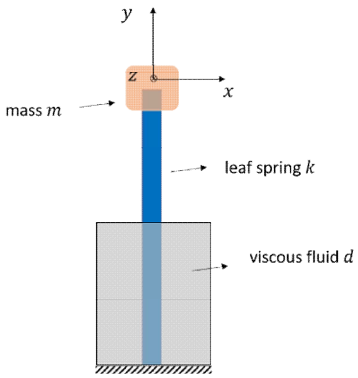

Figure 41: simplified model of the oscillating fiber as a single-degree-of-freedom system.

Here, the damped natural frequency ω_d can be described as

$$\omega_d \equiv \omega_0\sqrt{1-\zeta^2} \tag{5.1}$$

where ω_0 is the undamped natural frequency and ζ is the damping ratio, which is described as

$$\zeta \equiv \frac{1}{2Q} \tag{5.2}$$

Thus, Equation (5.1) can be rewritten as:

$$\omega_d \equiv \omega_0\sqrt{1-\left(\frac{1}{2Q}\right)^2} \tag{5.3}$$

If $Q = 85$, the equation above becomes

$$\omega_d \equiv \omega_0\sqrt{1-\left(\frac{1}{170}\right)^2} \tag{5.4}$$

Since the term to the square in Equation 5.4 is very small , the damped frequency practically equals the undamped natural frequency, thus for the MWCNT tested, according to this theoretical approach the energy dissipation is minimal. The reason for such a low energy loss system is likely associated with the nanoscale dimensions of the oscillator and the high vacuum present in the SEM chamber (below 10^{-2} Pa).

5.2.6 The compatibility of the MWCNTs with the Euler-Bernoulli beam theory

In many works reported by other researchers, carbon nanotubes present very high Young's modulus. However, it has been shown in this work that thicker multi-walled carbon nanotubes originated from the catalytic chemical vapor deposition are less resistant than very thin MWCNTs produced by arc-discharge. Apart from the structural and morphological characteristics that arise in the synthesis method, the high diameters of the MWCNTs analyzed here also play a key role in the mechanical response of these fibers, possibly contributing for the low modulus observed. This is explained by the onset of deformation patterns, such as rippling and buckling, which negatively affect the mechanical behavior of the fiber, leading to a decrease in the Young's modulus. These deformation patterns emerge when the fiber is under vibration at high amplitudes. However, during the resonance detection tests, it was not possible to control the onset of such deformation, due to the SEM resolution limitations. To search for changes on the microstructure of the nanotubes, it is necessary to use a very high magnification to observe closely the configurations of the walls during the vibration motion. Poncharal et al. used a TEM to detect the emergence of ripples in MWCNTs with diameters greater than 12 nm, which presented significant lower modulus (100 GPa) in comparison to thinner nanotubes from their study (1 TPa) [2]. In [11], the authors demonstrated that rippling caused a reduction of 50% on the Young's modulus of MWCNTs produced by CVD.

Further studies have deepened the knowledge regarding rippling and buckling as the scientific community observed the negative effects of such deformations on the Young's modulus of CNTs [41, 110, 111]. It was observed that buckling occurs with different morphologies under bending and both deformations invalidate the use of classical linear theories to describe the mechanics of nanotubes [112]. To investigate in detail the performance of nanotubes after the onset of rippling and buckling, many authors have applied computational models and have proposed non-linear theories as a more appropriate way to describe this behavior. Using molecular dynamics, Sumpter and Noid published a work reporting nonlinear resonance in carbon nanotubes [113], and other authors confirmed through numerical simulations the hypothesis that an increase of diameter leads to a decrease in E_b, due to the emergence of rippling. Additionally, it was shown that the appearance of ripples specifically at the inner radius during bending leads to a non-linear regime [114, 115]. In [112], the authors complemented the Euler–Bernoulli beam theory with additional models and emphasized that non-linear regime is inevitable for CNTs under bending. They showed, without accounting for the effects of deformation patterns, that the nanotubes could present complex nonlinear dynamics behaviors such as hysteresis, hardening and softening on the fundamental and second modes.

Nevertheless, in practical experiments many authors were able to present coherent results using a linear elasticity theory to describe the mechanical properties of the MWCNTs studied. In [8], the authors applied the linear elasticity theory for MWCNTs with maximum diameters of 20 nm and obtained experimental resonance frequency values very close to the theoretical ones. They concluded that buckling had little effect on the resonances of their MWCNTs. In [6, 56], the authors reported a linear bending behavior for MWCNTs even after the acknowledgement of rippling and buckling deformations. In [104] however, the authors

suggested an adjustment to the Euler–Bernoulli theory by adding more parameters to β to account for the effects of defects on the nanotubes body.

In the present investigation, for part of the nanotubes tested mostly only the first mode of resonance was detected, thus it was not possible to precisely infer whether they were governed by a linear or nonlinear regime . It could be the case that the second mode for such nanotubes was distant from the theoretical value and the pursuit for further modes would require more time-consuming experiments with higher spatial resolution and very slow frequency scans. Although the detection of nonlinearity is possible by varying the amplitude of excitation, for these cases, this procedure was not very effective due to signal instabilities caused by lower image contrast of the nanotube during excitation at high magnifications, above fifty thousand times, for example. Thus, the carbon nanotubes were excited mostly at 10 V, the maximum amplitude of excitation provided by the lock-in-amplifier. Another possible reason for the identification of only fundamental modes may be a weak contact between the base of the tube and the PEDOT:PSS film, which would not withstand vibrations in higher frequencies, due to more energy losses. However, for the cases where the nanotubes presented both first and second modes (Figure 33), one can evaluate their behavior by comparing the ratio $\boldsymbol{\nu_2/\nu_1}$ obtained experimentally with the theoretical value of 6.27 for perfect straight cantilevered beams. MWCNTs 4, 7 and 8 from Table 6 have $\boldsymbol{\nu_2/\nu_1}$ ratios proximate to the theoretical one and close values of Young's modulus at the first and at the second modes, indicating that these fibers vibrated in a linear regime. Here it might be the case that the beam model is acceptable, as our MWCNTs have a high aspect ratio and the resonance frequencies and amplitudes of the vibration are low [104]. In addition, it is possible that during the excitation frequency of the MWCNTs, the force necessary to produce bending deformation at the resonance frequencies is not high enough to produce rippling or buckling. Since the bending moment is proportional to the second moment of area I_a (Equation 2.23) and the latter is proportional to the diameter (D) of the tube $I_a \approx (\pi/64) \times D^4$, a stronger force would be required to bend thicker nanotubes to the point of causing rippling.

Nonetheless, the Euler-Bernoulli beam theory is a principle that describes the bending vibration of a straight, high aspect ratio beam, and as presented in previous sections of this work, the MWCNTs investigated here have a significant curvilinear morphology. For this reason, it is important to acknowledge other principles of continuous systems vibration that could characterize the bending behavior of curved beams accordingly.

5.2.7 Vibration of Curved Beams

The Euler-Bernoulli beam theory is a very consolidated principle that has been used to investigate the elastic properties of many types of nanofibers and was used to evaluate the Young's modulus of the MWCNTs tested in this project as well. These nanotubes have indeed a high aspect ratio, which is a pre-requisite for this theory, however their curvilinear morphology generates mechanical responses that may deviate from the Euler-Bernoulli concept, calling for the necessity to analyze their vibration behavior through other formulation principles. Such principles are developed specifically for curved beams and arches under

vibration and might give a better assessment of the dynamics and the deformation response of such systems.

The vibration of curved beams theory takes into consideration a curved beam with a constant radius of curvature R, an angle of bending θ and a thickness h, as presented in Figure 42. The equilibrium diagram originates in its middle surface, defined by the polar coordinate s, where

$$s = R\theta \tag{5.5}$$

and the tangential and radial displacements of the middle surface are designated as u and w, respectively [116].

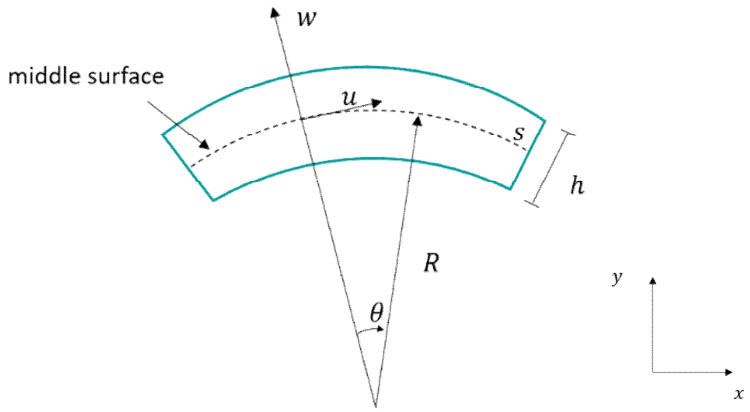

Figure 42: curved beam geometry and coordinates.

For an in-plane vibration, the middle surface strain ϵ_0 and the curvature change κ are described by

$$\epsilon_0 = \frac{\partial u}{\partial s} + \frac{w}{R}, \qquad \kappa = -\frac{\partial^2 w}{\partial s^2} + \frac{1}{R}\frac{\partial u}{\partial s} \tag{5.6}$$

Moreover, the free-body diagram of a differential element d_s of the curved beam from Figure 42 is represented as

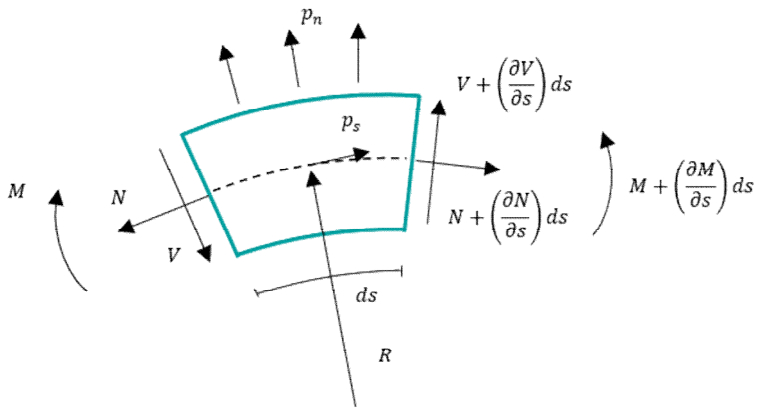

Figure 43: a free-body diagram of a small element of the curved beam

where p_s and p_n are the components in the tangential and radial directions, respectively, V is the shear force resultant, N is the resultant axial force and M is the rotary inertia. From the free-body diagram, the resulting equations of motion can be written as:

$$\frac{\partial N}{\partial s} + \frac{V}{R} + p_s = \rho A \frac{\partial^2 u}{\partial t^2} \tag{5.7}$$

$$-\frac{N}{R} + \frac{\partial V}{\partial s} + p_n = \rho A \frac{\partial^2 w}{\partial t^2} \tag{5.8}$$

$$\frac{\partial M}{\partial s} - V = 0 \tag{5.9}$$

where ρ is the density and A is its cross sectional area of the beam. It can be seen in Equation 5.9 that the rotary inertia is neglected in this case. Substituting this equation into Equations 5.7 and 5.8, gives:

$$\frac{\partial N}{\partial s} + \frac{1}{R}\frac{\partial M}{\partial s} + p_s = \rho A \frac{\partial^2 u}{\partial t^2} \tag{5.10}$$

$$-\frac{N}{R} + \frac{\partial^2 M}{\partial s^2} + p_n = \rho A \frac{\partial^2 w}{\partial t^2} \tag{5.11}$$

Now, the formulation approach developed by Baxy and Sarkar will be applied here in order to present an approximate solution for the natural frequencies of non-rotating curved beams [117].

Knowing that the harmonic time dependence of the transverse displacement[1] is $w(s,t) = W(s)e^{i\tilde{\omega}t}$, the governing equation of motion for the curved beam can be described as:

$$\frac{EI}{\rho A}\left(\frac{d^4W}{ds^4} + \frac{2}{R^2}\frac{d^2W}{ds^2} + \frac{W}{R^4}\right) - \tilde{\omega}^2 W = 0 \tag{5.12}$$

where E is the Young's modulus, I is the moment of inertia, ρ is the beam density, A is the cross-sectional area of the beam, and $\tilde{\omega}$ is the transversal natural frequency of the curved beam.

The corresponding equation for the Euler-Bernoulli beam is obtained from Equation 2.44, which in terms of the transverse displacement W and the polar coordinate s can be rewritten as:

$$\frac{EI}{\rho A}\left(\frac{d^4W}{ds^4}\right) - \omega^2 W = 0 \tag{5.13}$$

Comparing the Equations 5.12 and 5.13, it can be noticed that the curved beam equation presents two additional terms that account for the shape effect, described by the curvature R. this means that E for a curved beam tends to be smaller and the curvature contributes to a stiffening effect.

The boundary conditions for a fixed-free beam implicate in null displacement and null slope at the clamped end ($s = 0$), and null moment and shear force at the tip of the beam ($s = l$), as used for the Euler-Bernoulli beam theory in Section 2.2. Here, it is represented in terms of $W(s)$ as follows:

$$W(0) = 0, \quad \frac{dW(0)}{ds} = 0 \tag{5.14}$$

$$\frac{d^2W(l)}{ds^2} + \frac{W(l)}{R^2} = 0, \quad \frac{d^3W(l)}{ds^3} + \frac{1}{R^2}\frac{dW(l)}{ds} = 0 \tag{5.15}$$

[1] According to the authors of this paper, this solution of the equation of motion of a curved beam in terms of the transverse displacement was based on the formulation proposed by Werner Soedel [118. Soedel, W., *Vibrations of Shells and Plates*. 3rd Edition ed. 2004, Boca Raton: CRC Press.

For macroscale beams with small curvature, $1/R \to 0$, thus Equation 5.12 and 5.15 approximate to the Euler-Bernoulli theory. However, in the case of nanofibers, the curvature is much smaller than 1 and for this reason the term with R cannot be neglected.

Now, the equation of motion in terms of $W(\theta)$ is

$$\frac{EI}{\rho AR^4}\left(\frac{d^4W}{d\theta^4} + 2\frac{d^2W}{d\theta^2} + W\right) - \widetilde{\omega}^2 W = 0 \tag{5.16}$$

Simplifying $\sqrt{\frac{EI}{\rho AR^4}} = \Phi$, the equation above can be rewritten as

$$\frac{d^4W}{d\theta^4} + 2\frac{d^2W}{d\theta^2} + \left(1 - \frac{\widetilde{\omega}^2}{\Phi^2}\right)W = 0 \tag{5.17}$$

and the general solution for the equation above is

$$W(\theta) = A\cos(\delta\theta) + B\sin(\delta\theta) + C\cosh(\psi\theta) + D\sinh(\psi\theta) \tag{5.18}$$

where A, B, C and D are constants related to the boundary conditions and $\delta = \sqrt{\frac{\widetilde{\omega}}{\Phi} + 1}$ and $\psi = \sqrt{\frac{\widetilde{\omega}}{\Phi} - 1}$.

Applying the boundary conditions described above and solving the matrix for the constants A, B, C and D, the final equation for the determination of natural frequencies and the mode shapes $W(s)$ can be written as follows:

$$1 + \cos\left(\frac{\delta l}{R}\right)\cosh\left(\frac{\psi l}{R}\right) + \frac{1}{\delta\psi}\sin\left(\frac{\delta l}{R}\right)\sinh\left(\frac{\psi l}{R}\right) = 0 \tag{5.19}$$

$$W(s) = \cos\left(\frac{\delta s}{R}\right) - \cosh\left(\frac{\psi s}{R}\right) - C_c\left(\psi\sin\left(\frac{\delta s}{R}\right) - \delta\sinh\left(\frac{\psi s}{R}\right)\right) \tag{5.20}$$

where

$$C_c = \frac{\cos\left(\frac{\delta l}{R}\right) + \cosh\left(\frac{\psi l}{R}\right)}{\psi\sin\left(\frac{\delta l}{R}\right) + \delta\sinh\left(\frac{\psi l}{R}\right)} \tag{5.21}$$

Next, to propose an approximate solution, the curvature parameter $\epsilon_c = (l/R)^2 = \theta^2$ (remembering that $s/R = \theta$) is considered small, and as a consequence of this, the natural frequencies of a curved beam are obtained as a disturbance over the natural frequencies of a straight beam. Thus, the natural frequencies for a curved beam can be formulated as:

$$\widetilde{\omega}_j^2 = \omega_j^2 + \epsilon_c \widetilde{\Lambda}_j^2 \tag{5.22}$$

where ω_j is the natural frequencies for the analogous straight beam and $\widetilde{\Lambda}_j$ accounts for the curvature. Applying a non-dimensional term in each component of the equation above leads to

$$\tilde{\beta}_j^4 = \beta_j^4 + \epsilon_c \tilde{\lambda}_j^4 \tag{5.23}$$

where $\tilde{\beta}_j^4$ and β_j^4 are the non-dimensional natural frequencies for a curved and a straight beam, respectively. Upon extensive mathematical resolution $\tilde{\lambda}_j^4$ was obtained and can be described as

$$\tilde{\lambda}_j^4 = \frac{A_1 + A_2 k}{A_3 + A_4 k} \tag{5.24}$$

where $k = \frac{Al^2}{I}$ (A is the cross-sectional area, l is the beam length and I is the moment of inertia) and the values of the coefficients A_1 to A_4 for the first to the fourth mode of vibration are listed in the table below, according to Baxy and Sarkar [117]:

Table 8: values of coefficients A_1 to A_4 to insert into Equation 5.24

	Vibration mode			
Coefficient	**First**	**Second**	**Third**	**Fourth**
$\boldsymbol{A_1}$	0.7365	176.7	2107.06	9785.06
$\boldsymbol{A_2}$	-0.5017	112.2	352.71	736.41
$\boldsymbol{A_3}$	1.215	85.59	260.89	538.59
$\boldsymbol{A_4}$	-1	-1	-1	-1

5.2.8 Determination of the Young's modulus using the curved beams theory

Now, to compare the Young's modulus obtained via Euler-Bernoulli beam theory with the curved beam theory, the MWCNT number 8 from Table 6 was used. This nanotube is a good representation of a slender beam with a regular intrinsic curvature (see Figure 31b). Although, the radius of curvature is not constant for the entire length of this nanotube, which is a criterion for the application of this approach. Nonetheless, the following case is presented, as an example of an alternative analysis for curved nanofibers with constant radius.

To calculate the natural frequency of a curved beam at the first mode of vibration $\tilde{\beta}_1^4$ (Equation 5.23), the curvature parameter $\epsilon_c = (l/R)^2$ needed to be calculated. Thus, a post processing step was required, where the fiber was analyzed, and a fictitious circumference was drawn on the fiber in order to extract a radius value from the pronounced arc along the body of the nanotube. The image below illustrates this post processing:

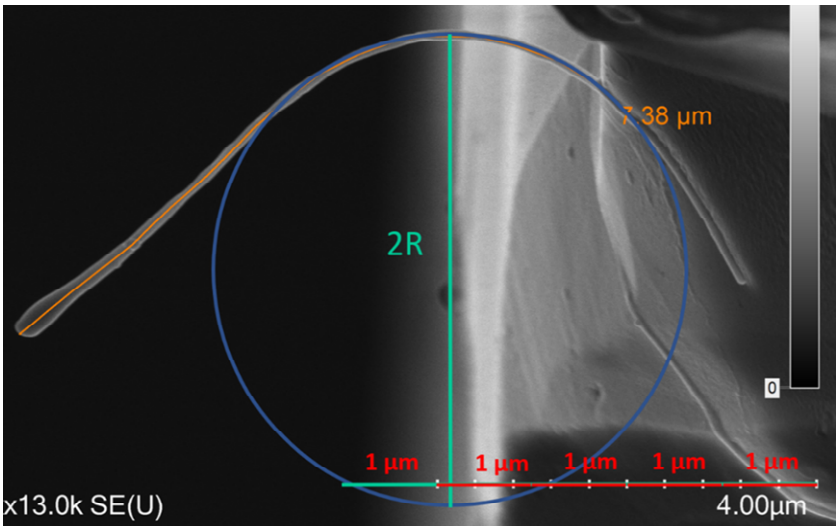

Figure 44: example of a post processing performed on a SEM image of MWCNT 8, where a circumference is drawn over the fiber and the radius is an approximate value obtained based on the scale bar.

In this image, the radius was obtained by using the scale bar as a reference measurement. The diameter was placed on top of the scale bar to be compared with the 4.00 µm defined during the experiment. In this way, it was noticed that the diameter was a fraction longer than 4.00 µm. Next, the extra portion of the diameter length was reproduced in color red and placed on top of the scale bar. This extra portion was observed to be approximately 1 µm. This way, a value of 5 µm was defined for the diameter and 2.5 µm for the radius. This measurement would be better performed in situ during the experimental tests within the SEM, along with the length measurements. A circumference would be drawn over the curvature of the nanotube and the diameter can be directly measured with the microscope metrics tools. This way, the value of the diameter, and therefore the radius is more accurate.

For a beam with a large radius R, the value of ϵ_c would tend to zero and the formulation presented here would correspond to the Euler-Bernoulli principle for straight beams.

Therefore, for this approach to be applied, the radius must be small and constant. For the nanotube in question, the curvature parameter ϵ_c equals 8.71, which is above zero and significant enough to affect the rigidity properties of the fiber.

After $\tilde{\beta}_1^4$ was obtained, the Young's modulus E could be derived using Equation 2.63 and replacing β_1^4 by $\tilde{\beta}_1^4$. For the MWCNT 8, the Young's modulus found was 11 GPa, which is 27% smaller than the Young's modulus derived via the Euler-Bernoulli beam theory (Table 6). In this case, the difference between the Young's modulus extracted from the Euler-Bernoulli principle and the curved beam theory is not very dramatic because this fiber does not deviate strongly from a perfect linear beam, despite its curvature. This can be confirmed by the ratio ν_2/ν_1 obtained experimentally, which for this nanotube equals 6.34 (theoretical $\nu_2/\nu_1 = 6.27$). However, it shows the effect of stiffening caused by the curvature, and therefore there is a significant difference between the two methods to analyze the Young's modulus of vibrating beams and apparently, the curved beam theory is an adequate method proposed to describe the motion of arched beams. For nanotubes that present more than one curvature along their length, the vibration behavior is much more complex and cannot be described by the curved beam theory.

A similar method to extract the Young's modulus of curved nanofibers was proposed by Calabri et al. [119]. In their work, an approach based on the classical Rayleigh-Ritz method was implemented to derive a corrected value of Young's modulus, neglecting the effects of adverse non-ideal boundary conditions, and focusing on the effect of the intrinsic curvature of the fiber. For the corrected modulus E_{curved}, the authors obtained the expression

$$E_{curved} = E_{straight}\left(1 + \frac{L^2}{25r^2}\right) \tag{5.25}$$

where L is the length obtained from a 3D reconstruction of the nanowire (more details in Section 6.2), r is the intrinsic curvature radius, $\frac{L^2}{r^2}$ is the intrinsic curvature of the nanofiber (ϵ_c), and $\frac{1}{25}$ is a constant multiplying factor c_r defined by a numerical procedure compatible with the tested nanowires. The $E_{straight}$ was calculated using the Euler-Bernoulli beam theory, using the resonance frequencies obtained experimentally. The authors found an average difference of ~2.7% between $E_{straight}$ and the corrected E_{curved}. In the article, it was not described how the authors extracted the curvature radius from different nanowires.

5.3 Silicon Carbide Nanowires

5.3.1 Young's modulus measurements of SiC NWs

BAuA prepared the samples of SiC NWs standing free on tuning fork crystal units via the same procedure used previously to fix MWCNTs (the detailed description of the preparation of the samples can be found in Section 4.1). The quality of the first SiC NWs samples provided by BAuA was very satisfactory, containing many single nanowires fixed by the base at the

edges of the piezo, which is one of the main conditions for a successful resonance detection. When there are many non-agglomerated clean nanofibers properly positioned on the edges of the piezo units, the number of nanofibers tested increases considerably and the chances of acquiring more volume of data and therefore, more results, are higher. Another factor that contributes positively for the detection of resonance frequencies and for the applicability of the Euler-Bernoulli (E-B) beam theory is a beam-like shape nanofiber, and the SiC NWs used here had indeed a very straight and bulky configuration. Roughly 90% of the fibers selected to be tested had their resonance frequency at the first mode successfully detected.

A group of twelve SiC NWs was tested with the Dynamic Scanning Electron Microscopy technique in an EVO MA 10 SEM (Carl Zeiss Microscopy GmbH, Jena, Germany) from BAM. The results are presented in Table 9 and in Figure 45(a) and (b).

Table 9: Young's modulus of the SiC NWs tested. D is the diameter of the nanowires, L is their length, ν_m is the resonance frequency, E_1 is the Young's modulus at the first mode, E_2 is the Young's modulus at the second mode and E_3 is the Young's modulus at the third mode. The estimated experimental errors are ± 3 nm for D, ± 800 nm for L and ± 1 kHz for ν_1, ν_2, and ν_3. The average error for E is 18.6% and the error associated to each E is presented in Table 10.

SiC nanowire	D (nm)	L (μm)	ν_1 (MHz)	ν_2 (MHz)	ν_3 (MHz)	ν_2/ν_1	ν_3/ν_2	E_1 (GPa)	E_2 (GPa)	E_3 (GPa)	E (GPa)
1	104	7.36	1.847	-	-	-	-	152	-	-	152
2	104	11.1	0.948	-	-	-	-	207	-	-	207
3	116	18.0	0.346	2.541	-	7.34	-	153	210	-	181.5
4	128	31.3	0.122	0.760	-	6.23	-	143	141	-	142
5	152	9.8	1.656	-	-	-	-	182	-	-	182
6	183	18.1	0.735	-	-	-	-	294	-	-	294
7	218	19.5	0.613	3.779	-	6.16	-	186	180	-	183
8	258	44	0.166	1.064	-	6.41	-	255	266	-	260.5
9	265	54.0	0.083	0.467	1.314	5.63	2.81	137	111	112	120
10	304	27.5	0.486	2.985	-	6.14	-	240	226	-	233
11	312	31.6	0.355	2.201	-	6.20	-	211	206	-	209
12	371	29.3	0.630	-	-	-	-	340	-	-	340

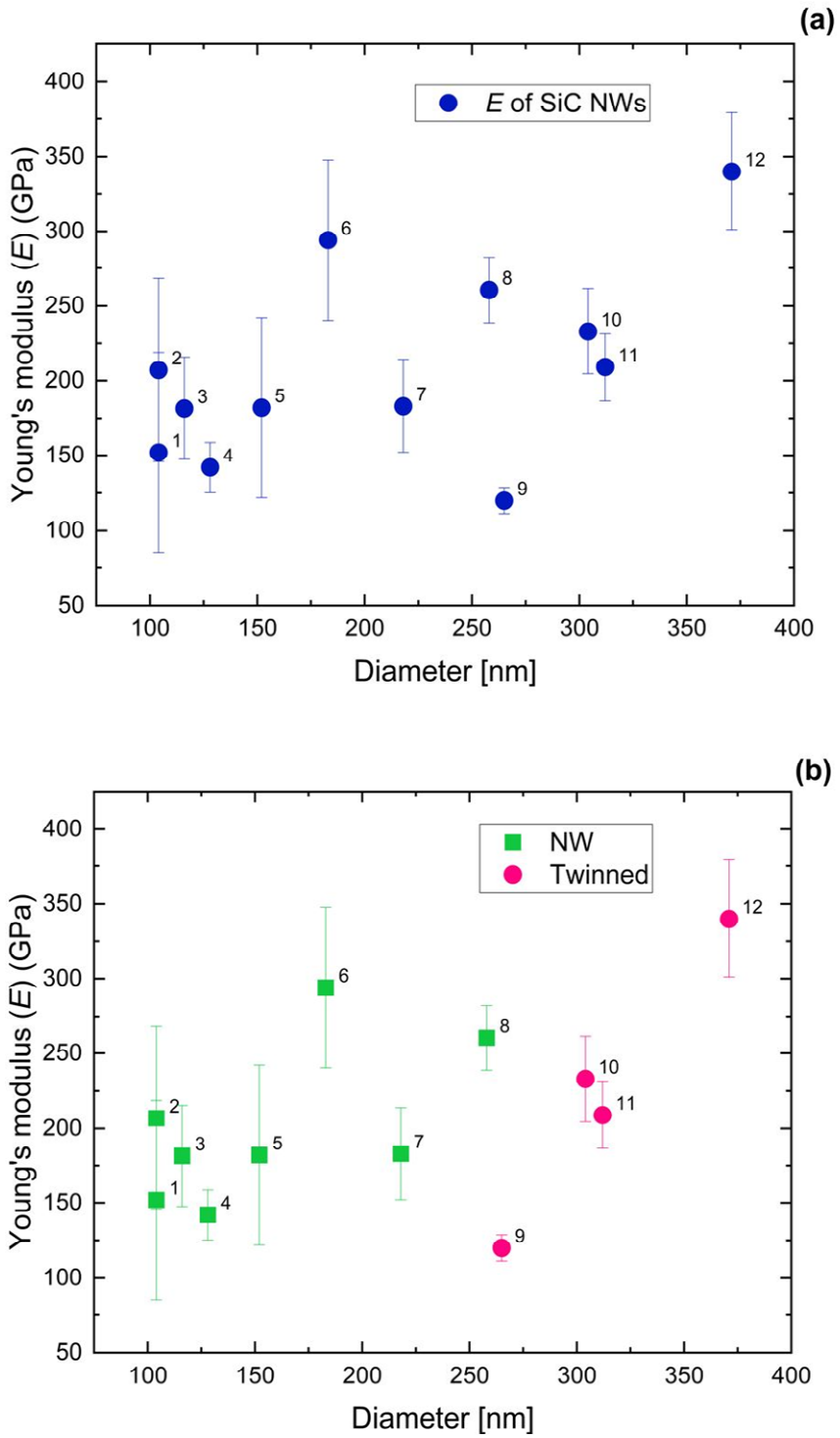

Figure 45: Graphs of the Young's modulus values *E* vs. diameter *D* for the SiC NWs tested in this work. Graph (a) shows all the results presented in Table 9, graph (b) indicates which results belong to which type of SiC morphologies: nanowire or twinned.

The SiC NWs presented *E* between 105 and 340 GPa with 18.6% of average error. These results are within the range found in the literature for thick SiC NWs (Table 3), however higher values of Young's modulus were found by other researchers for SiC NWs with considerably smaller diameters, or with morphologies different from the ones presented here. For example, in [49], Cheng et al. reported Young's Modulus around 1270 GPa for SiC NWs with diameters

of 17 nm and very low defect density. In general, SiC nanowires present several kinds of configurations that are obtained depending on the parameters of synthesis such as cooling temperature, system pressure, catalyst material, etc. And each type of structural configuration has a different mechanical response. During the experiments, two types of SiC morphologies were tested, the regular nanowires and the twinned shaped. The twinned SiC had higher diameters, but their Young's modulus were as assorted as the Young's modulus of the nanowires, exhibiting low and high values of E (number 9 and 12, respectively in Figure 45b). The SiC NWs showed scattered values of Young's modulus with no direct correlation between the modulus and the diameter nor the length. Compared to the MWCNTs tested previously, the SiC NWs are stiffer, which is reflected by the differences observed in their morphologies, as the nanowires exhibited a bulky straight shape and the nanotubes were thinner and curved, showing more flexibility.

For most of the SiC NWs the resonances at first and at second modes were detected (Figure 46). Among these, the results found experimentally were approximate to the theoretical values, which can be seen by the ratio between the frequency detected at the second mode and at the first mode ($\boldsymbol{\nu_2/\nu_1}$) of vibration. This ratio is 6.27 for perfect linear elastic beams, or 2.8 ($\boldsymbol{\nu_3/\nu_2}$) in the case where a third mode was also detected (SiC NW number 9). In these cases, the Young's modulus was calculated as the average between the modulus obtained at each mode. The nanofibers that presented only the first mode of vibration likely deviate more from the theoretical value, which makes it more difficult to predict the further modes, calling for experiments with longer periods of time. This may be a consequence of an extra mass on the body of the nanofiber since the nanofibers tested here are not impurity-free material and the variations on the thickness, making their mechanical behavior less predictable. These factors also influence the deviation of the experimental frequency from the theoretical value for $\boldsymbol{\nu_2/\nu_1}$ and for $\boldsymbol{\nu_3/\nu_2}$.

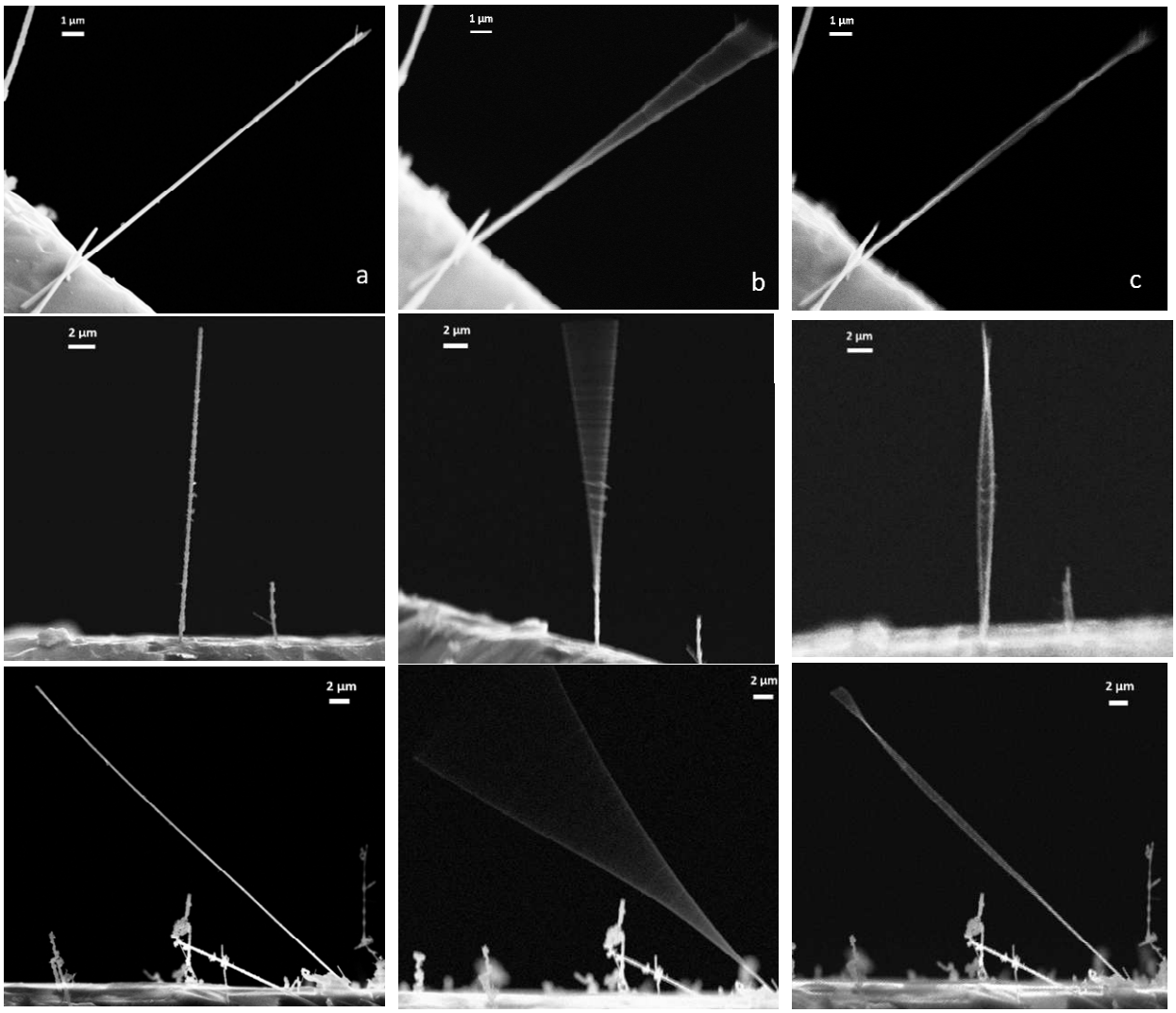

Figure 46: DySEM images of three different SiC NWs at stationary mode (column a); vibrating at first mode (column b); and vibrating at second mode (column c).

5.3.2 Length and diameter measurements of SiC nanowires

In the equation used to obtain the Young's modulus E from the Euler-Bernoulli theory (Equation 2.63) , the length (L) is to the fourth power, thus to avoid large errors in the Young's modulus value it was important to measure the lengths of the nanowires with accuracy. The length used in the E-B equation is defined from the fixation point of the nanofiber on the piezo until its tip. The nanowires tested here were very erect, which contributes for a reliable measurement of their lengths, however, to assure that the right length is being measured, the entire fiber has to be in the same horizontal plane. This can be validated by first focusing the beam on one end of the nanowire, and next observing the other extremity without changing the scanning conditions. If the entire fiber is focused, it means that the projected image is essentially the same as the real three-dimensional material, and the measured length is the correct one. However, some of the nanowires were leaning toward the back planes, or the front planes rather than being aligned with the piezo plane, producing a projected length that is altered in relation to the true length. An example of this occurrence can be found in Figure 47.

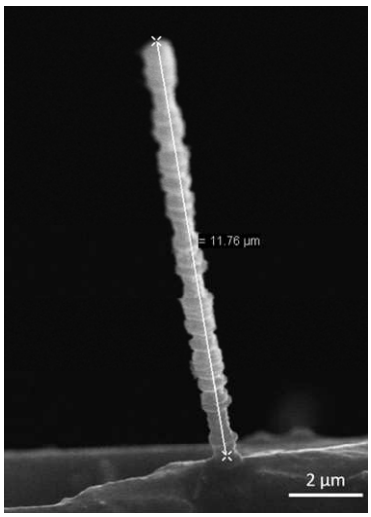

Figure 47: a SEM image of a silicon carbide twinned type illustrating how the focus can be an auxiliar tool to indicate that the length measured in the observed projection is not the true length. At the fixation point, the image of the fiber is sharp, however, it becomes unsharp at the tip, signalizing that the fiber is leaning towards other planes, and that the displayed length of 11.76 µm is smaller than the real fiber length.

For this reason, during the investigation of the SiC NWs, their length was verified twice by tilting the piezo unit in approximately 60° (Figure 48). This was the maximum tilt degree possible to be reached while still being able to identify the correct nanowire, maintaining a satisfactory background contrast. This procedure was made for the nanowires standing free at the right edge of the piezo substrate. It is worth mentioning that the majority of the experiments and the measurements of the fibers' dimensions was made with the piezo drive at the default tilt of 0°. At this angle, the fibers can be better assessed due to the high contrast of the fiber with the background. The highest value of the fiber length obtained from both 0° and 60° of piezo tilt was then chosen to be used in Equation 2.63. In special cases, where the fiber was oriented towards the background of the SEM chamber, the tilt had to be adjusted step-by-step until a sharp image of the entire fiber was acquired. Unfocused spots on the fiber length indicate that the fiber is not entirely on the same plane, thus the measurement of the length in this case would not be adequate. Examples of the length measurements of the SiC NWs with two different viewing angles are shown in Figure 49.

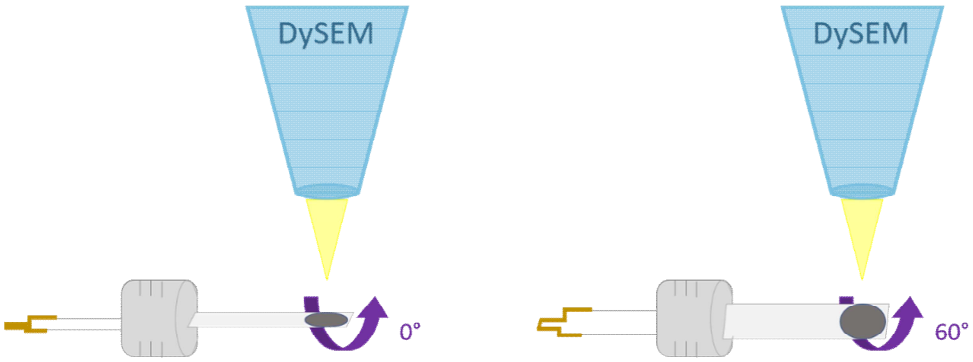

Figure 48: Diagram showing the direction of tilt of the piezoelectric device unit inside of the SEM chamber to evaluate the length from another perspective (for the nanowires on the right edge). The circular gray region indicates the area where the fibers were deposited.

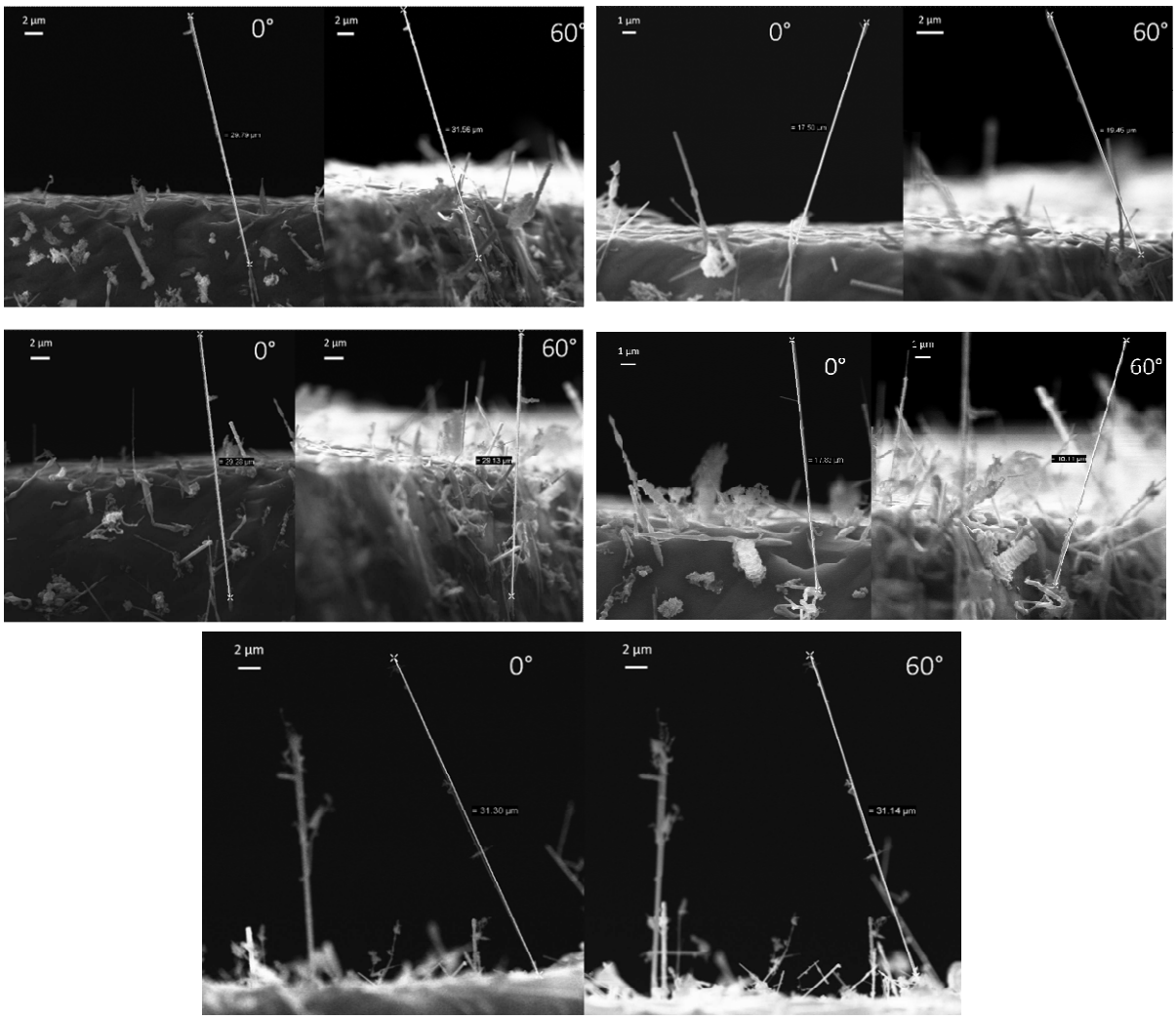

Figure 49: a series of SEM images showing the length measurement for a set of SiC NWs from two different perspectives: the images on the left column are at 0° piezo tilt and the images on the right column are at 60° piezo tilt.

Apart from the concern to define the correct length values, the diameter measurement also required an extra step, as the thickness of most of the nanowires varied along their length. Thus, to obtain an approximate value of the diameter, the thickness of a nanowire was

measured in four different points so that an average value was extracted (Figure 50). The diameter was then obtained by the averaged thickness measured, in a procedure similar to the one used for the MWCNTs.

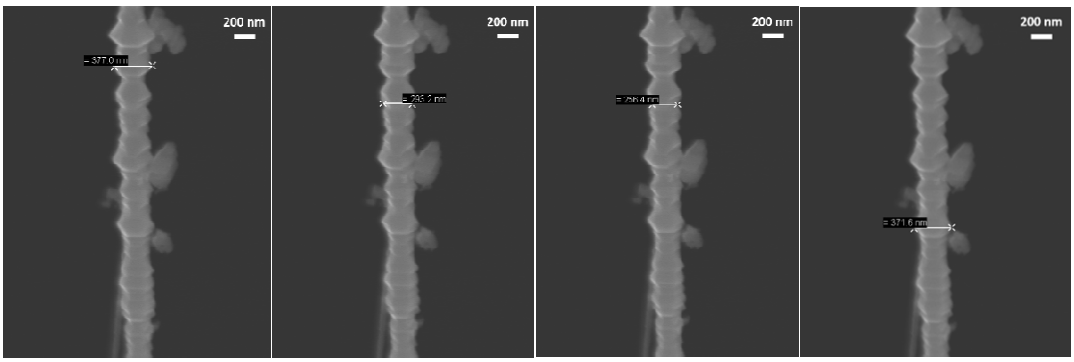

Figure 50: SEM images of the measurement of the diameter of a SiC nanowires in four different points. The diameter used in the Euler-Bernoulli formula was defined as the average of the values obtained from these SEM images. This procedure was applied to all the nanowires tested (Zeiss EVO MA 10)

5.3.3 Error estimation for the Young's modulus of SiC NWs

After performing the verification of length for half of the NWs tested by tilting the piezo in 60° from the initial position, it was observed that the difference between the length of the nanowire obtained at 0° and at 60° was in average 3.2%. To estimate a general length deviation for all the samples (considering that some fibers were not possible to be observed at 60° tilt), this value was applied to the lengths of all twelve SiC NWs tested and the result was an average length of $\pm$ 800 nm. Therefore, for a deviation on the length of 800 nm, the corresponding average error value for the Young's modulus was 18.6%. The error associated to the Young's modulus for each SiC nanowire tested is presented in Table 10. The estimated error associated with the diameter is ± 3 nm and 1 kHz for the resonance frequencies.

Table 10: Young's modulus of SiC NWs from Table 9 with the associated error values.

SiC NW	*E* (GPa)	Error (%)
1	152 ± 66.8	44.0
2	207 ± 61.2	29.6
3	181.5 ± 34.1	18.8
4	142 ± 16.7	11.7
5	182 ± 60.1	33.0
6	294 ± 53.7	18.3
7	183 ± 31	16.9
8	260.5 ± 21.7	8.3
9	120 ± 8.7	7.2
10	233 ± 28.5	12.2
11	209 ± 22.5	10.8
12	340 ± 39	11.5

5.3.4 Energy dissipation in the excitation tests of SiC NWs

Since the SiC nanowires studied here have shown to be a very adequate type of nanofiber for the mechanical excitation experiments presented, a deeper investigation on the damping existing in the system was performed. One of the parameters to be analyzed was the quality factor for some nanofibers during frequency sweeps with high resolution of data acquisition, and the effect of the nanowire thickness on the quality factor values. For that, four NWs with different diameter sizes were selected and retested. These are SiC NWs numbers 6, 7, 11 and 12 in Table 9. In order to investigate more closely the energy dissipation in the experimental setup, the resonance was detected by collecting a higher number of points with a resolution of 10 Hz (which means that a data point was computed at every 10 Hz) and at a voltage of 7 V.

To obtain the quality factor Q of the nanowires mentioned, the Lorentzian fit of the amplitude versus frequency curve of each of the nanowires was obtained (Figure 51). The detailed description of the relation between the Q- factor and the resonance frequency can be found in Section 5.2.5. The four NWs presented a relatively high value of quality factor in the range from 2800 to 5200, which is comparable to the remarkable results of Q=3500 and Q=5000 reported by Perisanu et al. [44, 45]. When excitation experiments are performed in air, one significant source of extrinsic energy dissipation is the air damping. These experiments were executed in a high vacuum chamber (below 10^{-2} Pa), thus the energy losses are attributed mostly to intrinsic characteristics, such as stacking faults and defects that could cause inner friction. Thermoelastic losses due to the transfer of heat caused by the movements of expansion and compression during the high amplitude oscillation can increase the dissipation as well. The other possible source of damping is the quality of the clamping, which was evaluated by observing closely the clamped end of the nanofiber during the oscillation period. A more detailed characterization specifically on the condition of the clamping point using other tools was not executed on the course of this project, although is suggested for future investigations. It is worth mentioning that very high values of Q-factor are crucial when the main application of the oscillator is in MEMs, and the values encountered here for the SiC NWs are very satisfactory for the extraction of resonance frequencies and ultimately the elastic modulus.

In Figure 51, the Lorentzian fit of the amplitude vs. frequency curves of the four SiC NWs are disposed from the thinner to the thicker nanowire, as it has been reported for other types nanowires that the quality factor increases proportionally with the increase of the fiber diameter [120]. In this case however, this tendency was not observed for the group of nanowires tested. As a matter of fact, the lowest value of Q-factor was observed for the nanowire with the highest diameter (371 nm; bottom right graph of Figure 51).

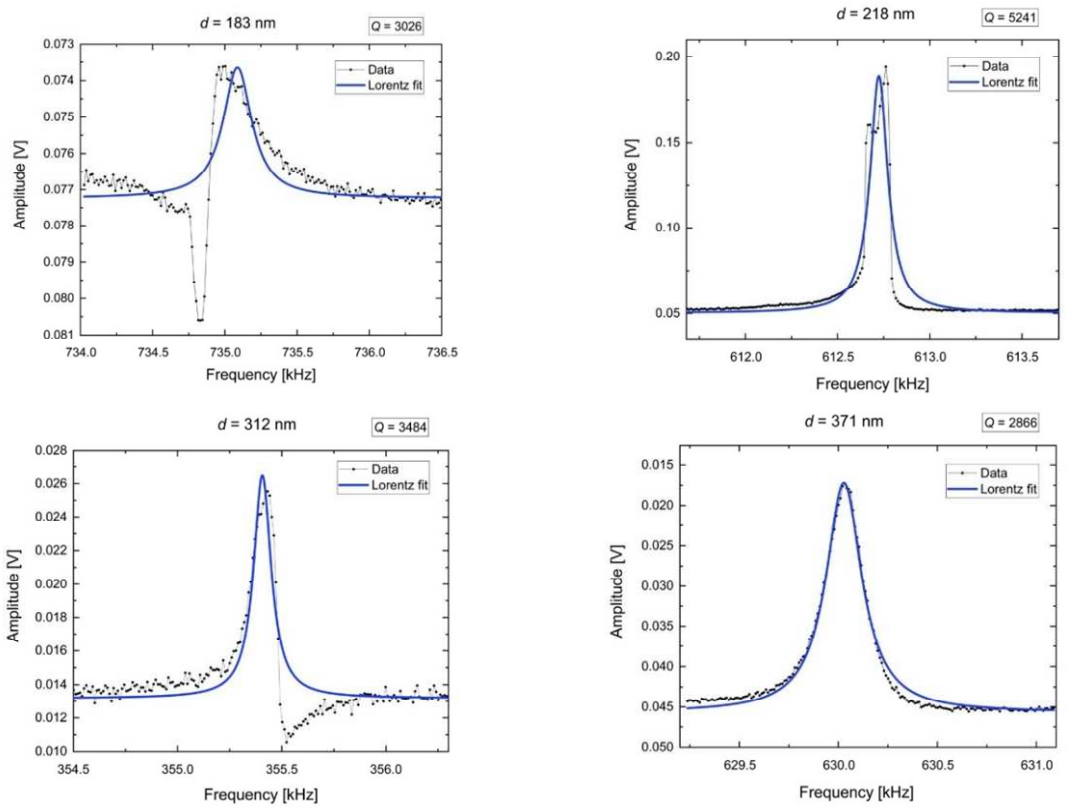

Figure 51: Lorentzian fit of amplitude vs. frequency curves and the correspondent quality factors for four SiC NWs. The letter *d* in each graph stands for the diameter of the nanowires. The disposition of the graphs in clockwise order represents the data of NWs 6, 7, 11 and 12 from Table 9 respectively.

5.4 Flexural rigidity of nanofibers

Knowing the bending stiffness of nanomaterials is surely crucial for their application as structural components, and for this reason there is a wide space for the research and development of new techniques capable of characterizing with accuracy the mechanical behavior of such materials. Especially taking into consideration that a great amount of nanometric fibers present remarkable resistance to tensile and bending stresses, making them promising candidates to integrate lightweight performance systems. Alongside with being a prerequisite to constitute consumer and industrial products, the classification of the flexural rigidity of nanofibers plays an important role also at the manufacture, due to implications on occupational health, and at the disposal phase, with the release of particles to the atmosphere. As it has been proved by researchers concerned about the impacts of biopersistent nanofibers in human lungs (Section 1.1), stiff airborne nanofibers that reach the deep airways of the respiratory system can cause serious damages to the defense cells. For this reason, in this work we have presented a promising method to extract the elastic behavior of nanofibers with the main purpose of providing information about their rigidity.

Recalling the fiber toxicology paradigm, the hazard posed by biopersistent nanofibers to defense cells called macrophages is directly dependent on the fiber's dimensions and on the flexural rigidity. To indicate approximately to which extent the macrophages are able to fight nanofibers, Broßell et al. presented the maximum compressive force that a macrophage is able

to exert on a substance to perform a successful phagocytosis [121]. By making an analogy to a slender column being compressed, resulting on its deflection, Euler's critical load f_{cr} is translated as the compressive load being applied on the fiber axis by the macrophage, and this force results in 10 nN. Thus, for the fiber to overcome this compression state, it needs to satisfy the condition:

$$f_{cr} = \frac{\pi^2 R}{(KL)^2} = \frac{\pi^2 EI}{(KL)^2} \tag{5.26}$$

where R is the flexural rigidity, L is the length of the fiber, and K is the column effective length factor, considered 1.2 for a clamped-free fiber. The critical rigidity value R_{cr} associated with the critical load is ~10^{-19} N·m^2. This means that fibers presenting a flexural rigidity lower than 10^{-19} N·m^2 are classified as flexible, and can be removed from the body during the phagocytosis. The fibers with rigidity in the order of 10^{-19} N·m^2 or higher are likely harmful and stiff enough to cause damages on the macrophages, posing hazard to defense cells of lungs.

After obtaining the Young's modulus for a group of MWCNTs and SiC nanowires, their flexural rigidity was then determined according to Equations 2.64 and 4.2. The resulting rigidity profile of the nanofibers is displayed in the graph of the flexural rigidity vs. diameter, presented in Figure 52. As it can be seen in the graph, all the nanofibers tested in this work showed values of rigidity above the critical rigidity threshold of 10^{-19} N·m^2, identified by the horizontal red line. In addition, the data points demonstrate a tendency of proportional increase of flexural rigidity with the increase of the fiber thickness, although the nanofibers studied here haven't presented a regular increase of Young's modulus with the increase of diameter. This means that in regard to the bending behavior, the diameter has clearly a remarkable impact. This exemplifies that flexural rigidity is considered a more accurate parameter to assess potential fiber hazards than diameter or Young's modulus alone.

To group the rigid and flexible fibers from this study by the diameter values though, one could define a thickness of ~ 75 nm as the threshold of safety for fibers that have an E maximum of 160 GPa, which corresponds to the type of MWCNTs used in this work. This means that the nanotubes from this batch, that are thicker than 75 nm, can be defined as rigid and harmful and the ones with diameters smaller than 75 nm are flexible and harmless, prior to any mechanical testing. The critical diameter of 75 nm was defined from the graph of flexural rigidity vs. diameter (Figure 52).

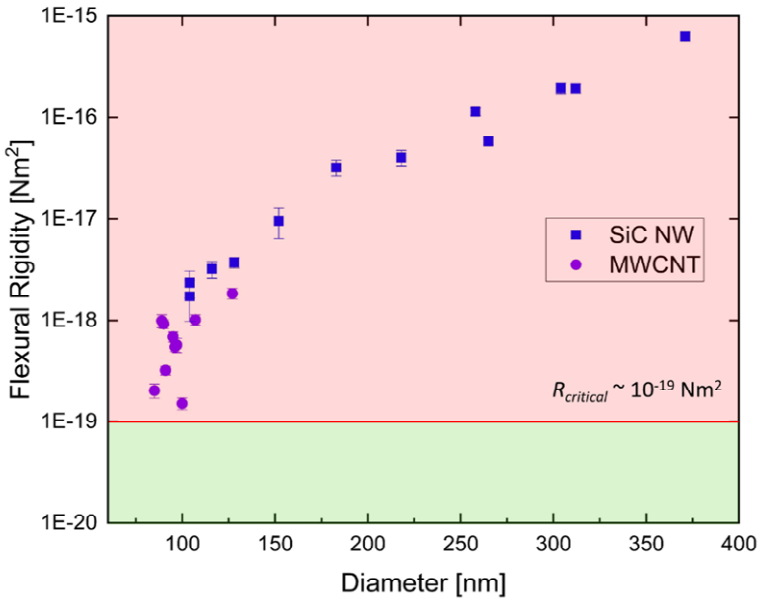

Figure 52: Plot of the rigidity data of silicon carbide nanowires and multi-walled carbon nanotubes tested in this work. The rigidity data is displayed in the logarithmic scale, highlighting the rigidity threshold of 10^{-19} Nm². All the fibers presented are potential hazard agents during phagocytosis

Analyzing closely the rigidity of the ten multi-walled carbon nanotubes in Figure 53 below, it can be noticed that the rigidity does not increase uniformly with the increase of the diameter, which can be explained by pronounced variations on the Young's modulus, combined small thickness differences among the nanotubes. However, since the flexural rigidity scales with the 4th power of the diameter, nanotubes that presented low values of Young's modulus, but had the highest diameters (MWCNTs 9 and 10) turned out to be the most rigid ones, followed by nanotubes 2 and 3, that had in fact the highest Young's modulus. In addition, the nanotubes 9 and 10 were considerably thicker than most of the other nanotubes. The tendency of increasing the rigidity with the increase of the diameter is observed when a representative group of samples is analyzed, as in the graph from Figure 52.

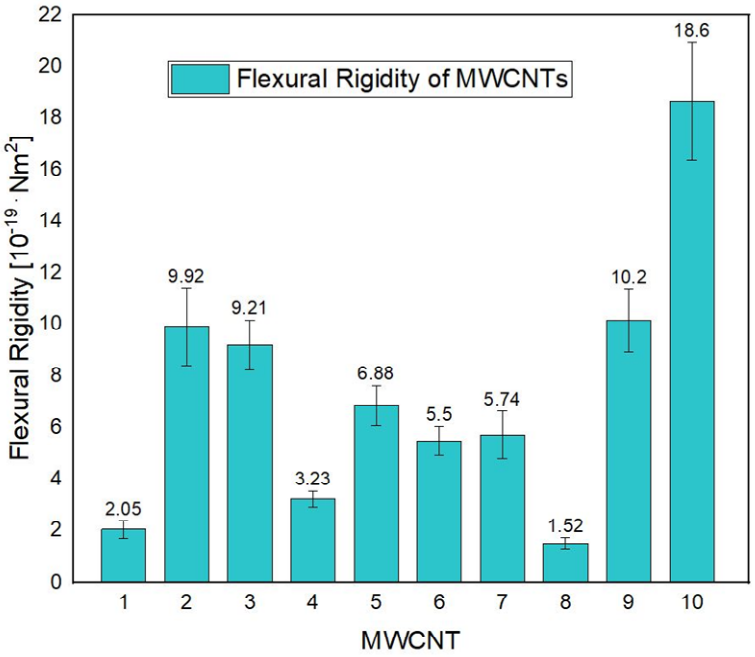

Figure 53: Graph of the flexural rigidity of the MWCNTs tested. The nanotubes are organized according to the sequence presented in Table 6, i.e., from the thinnest to the thickest nanotube.

The flexural rigidity of SiC nanowires and the associated error are shown separately as well, in the bar graph from Figure 54. The graph shows that these nanowires presented high values of rigidity, all above 10^{-19} N·m^2. These high values of rigidity are consequences of both their high thickness (between 100 and 400 nm), and the fact that most of these nanowires showed high values of Young's modulus. Although a tendency of increasing the Young's modulus with the increase of diameter was not significantly pronounced, the flexural rigidity showed to increase quasi proportionally with the diameter.

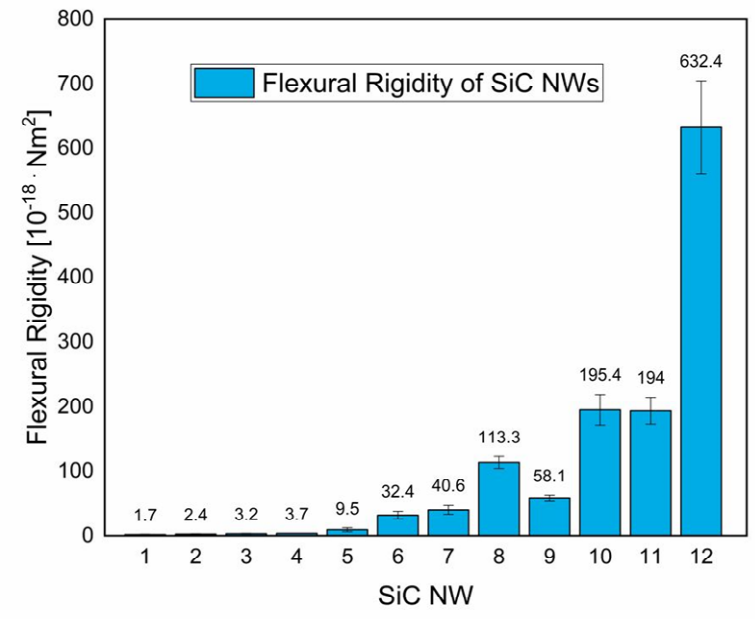

Figure 54: Graph showing the variations on the rigidity of the twelve SiC NWs tested.

Since all the SiC NWs tested have flexural rigidity values far above the threshold of 10^{-19} $N \cdot m^2$, in the order of 10^{-18} $N \cdot m^2$, it is not adequate to define a critical diameter for these fibers. Thus, the type of silicon carbide nanowires investigated in this work are defined as potentially hazardous for defense cells of the lung's tissues.

5.5 Analysis of the effect of the boundary conditions on the first natural frequencies and on the rigidity of the nanofibers studied.

In the method proposed in this work, the fixation of the nanofibers on the surface of the piezo is accomplished with the use of a PEDOT:PSS polymeric film, which works as a glue during its viscous state, and is sufficiently conductive to be submitted to the electron beam of the microscope without interfering in the scanning analysis. As it has been discussed in Section 5.1, the ideal material to be used as a clamping tool should be stiff and conductive, which are common characteristics found in metallic materials. However, the clamping material should be viscous enough at ambient temperature in order to receive and incorporate the base of the fibers in its matrix. This feature cannot be easily achieved with a metallic alloy or pure metal, as proved in Section 5.1, therefore the choice of a conductive polymer.

The use of a polymeric film that is not very stiff as clamping material may influence the natural frequencies detected, impacting on the Young's modulus obtained through the resonance method. This occurs when the clamping conditions are not optimal, meaning that it does not represent with fidelity the fixed-free boundary conditions state described in Section 2.2.1.

An example of the clamping conditions impact on the resonance frequencies of nanowires was illustrated in the work of Qin et al. . The authors investigated the Young's modulus of ZnO nanowires via the resonance method in a scanning electron microscope. In their work, the nanowires were clamped using electron-beam-induced-deposition of residual hydrocarbon. This method permits a controlled local deposition of clamping material at the base of the fiber to the substrate. In addition, the hydrocarbon is considered a stiff material with a Young's modulus ranging from 30 to 60 GPa, depending on the acceleration voltage of the electron beam [122]. The resonance frequencies of the nanowires increased proportionally with the increase of the clamp size, until reaching the true stable resonance frequencies at a certain amount of deposited clamping material, as shown in Figure 55 [105]. At this point, the system becomes indeed compatible with the fixed-free boundary conditions and Equation 2.62 can be applied.

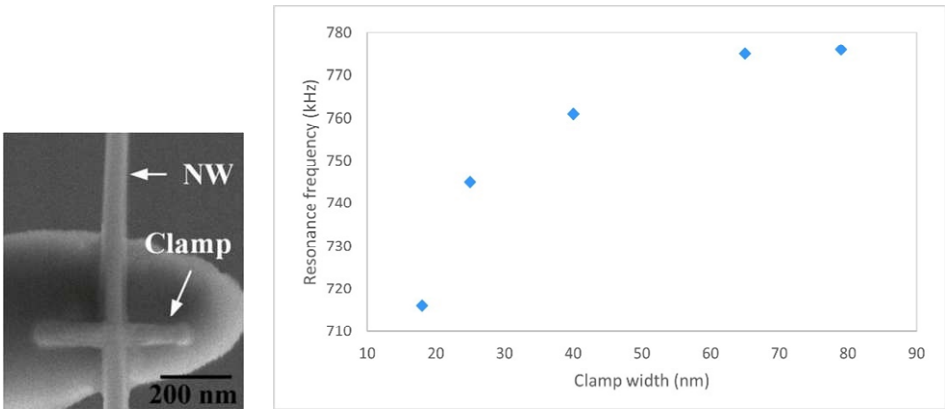

Figure 55: image of the nanowire's fixation point covered with the deposition material at the base (left); approximate data points showing the tendency of increasing the resonance frequency with higher dimensions of clamp material, until reaching a stable resonance value (at around 780 kHz) with an optimal clamp width. Image and data extracted from [105].

Analysis of the first natural frequencies and rigidity for a beam presenting a rotational spring at the base

Considering that the PEDOT:PSS is a much less stiff material (Young's modulus ~2 GPa [95, 96]), it may be the case that the fixed-free boundary condition does not apply, even with the increase of material deposited. For this reason, another approach[2] for determining the natural frequencies, and the rigidity of the oscillating nanofibers is going to be described next [123]. In this approach, the beam is supported by a rotational spring at the base, instead of a clamp, and free at the end, as shown in Figure 56.

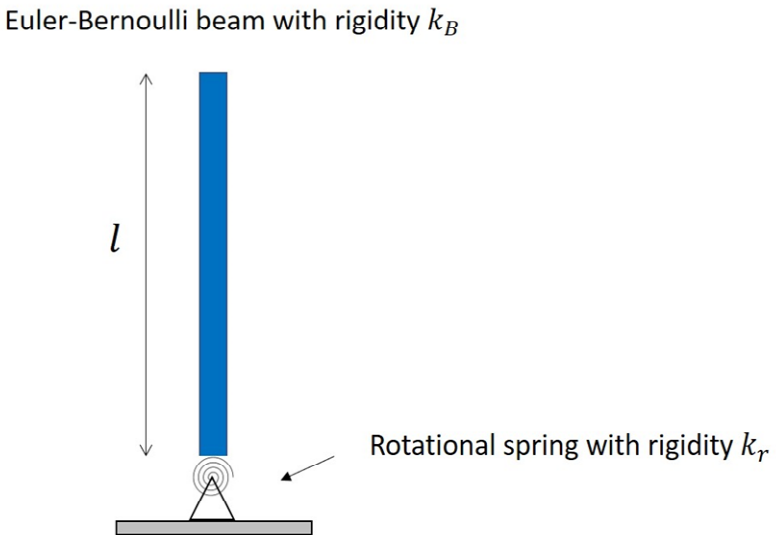

Figure 56: Euler-Bernoulli beam supported by a rotational spring

[2] This approach was developed by Prof. Dr.-Ing. Kerstin Kracht, 2021.

For a Euler-Bernoulli beam with a length l and a flexural rigidity $k_B = EI$, the analysis begins using the Hamilton's principle:

$$\delta \int_{t_0}^{t_1} T - U dt + \int_{t_0}^{t_1} \delta W dt = 0 \tag{5.27}$$

where T is the kinetic energy, U is the potential energy, and W is work. Now, knowing that

$$T = \frac{1}{2}\rho \int_0^l \dot{w}^2(x,t) dx \tag{5.28}$$

$$U = \int_0^l \frac{1}{2} EIw''^2(x,t) dx + \frac{1}{2} k_r \dot{w}^2(x=0,t) \tag{5.29}$$

and

$$\delta W \cong 0 \tag{5.30}$$

where ρ is the density of the beam, E is its Young's modulus, I is the cross-sectional area moment of inertia, and k_r is the rotational spring stiffness, the Hamilton's principle can be then rewritten as:

$$\delta \int_{t_0}^{t_1} \frac{1}{2}\rho \int_0^l \dot{w}^2(x,t) dx - \int_0^l \frac{1}{2} EIw''^2(x,t) dx - \frac{1}{2} k_r \dot{w}^2(0,t) = 0 \tag{5.31}$$

Solving and rearranging each term of the Equation 5.31, results in:

$$\begin{aligned} \int_{t_0}^{t_1} \Bigg[\int_0^l \left(-EIw^{iv} - \rho \ddot{w}\right) \delta w dx + (EIw'' - k_r w') \delta w' \Big|_{x=0} - EIw'' \delta w' \Big|_{x=l} \\ - EIw''' \delta w \Big|_{x=0} + EIw''' \delta w' \Big|_{x=l} \Bigg] dt = 0 \end{aligned} \tag{5.32}$$

Now, knowing that the equation of motion is:

$$-EIw^{iv} - \rho\ddot{w} = 0 \tag{a}$$

The geometric boundary conditions are:

$$w(x = 0, t) = 0 \tag{b}$$

And the dynamic boundary conditions are:

$$EIw'' \Big|_{x = 0} - k_r w' \Big|_{x = 0} = 0 \tag{c}$$

$$-EIw'' \Big|_{x = l} = 0 \tag{d}$$

$$EIw''' \Big|_{x = l} = 0 \tag{e}$$

To evaluate the ratio in question, and its effect on the first natural frequency of the system, (c) is calculated as follows:

$$EIw''(x = 0, t) - k_r w'(x = 0, t) = 0 \Big| : k_B \tag{5.33}$$

And $EI = k_B$, thus

$$k_B w''(x = 0, t) - k_r w'(x = 0, t) = 0 \tag{5.34}$$

$$\frac{k_r}{k_B} w'(x = 0, t) - w''(x = 0, t) = 0 \tag{5.35}$$

The equations for w' and w'' arise from the solution of the differential equation of motion:

$$-EIw^{iv} - \rho\ddot{w} = 0 \tag{5.36}$$

Considering that $w(x,t) = T(t) \cdot W(x)$, the equation above can be rewritten as:

$$-EIT(t) \cdot W^{v}(x) - \rho\ddot{T}(t) \cdot W(x) = 0 \quad \Rightarrow$$

$$\Longrightarrow -\frac{EI}{\rho}\frac{W^{iv}(x)}{W(x)} = \frac{\ddot{T(t)}}{T(t)} = -w_0^2 \tag{5.37}$$

Concerning the deflection mode:

$$(1) \quad \frac{EI}{\rho}\frac{W^{iv}}{W} = w_0^2 \tag{5.38}$$

being

$$W^{iv} = \frac{w_0^2\rho}{EI} \cdot W \tag{5.39}$$

where

$$\frac{w_0^2\rho}{EI} =: \beta^4 \tag{5.40}$$

Thus,

$$w^{iv} - \beta^4 W = 0 \tag{5.41}$$

Now, considering that

$$W(x) = A\sin\beta x + B\cos\beta x + C\sinh\beta x + D\cosh\beta x \tag{5.42}$$

And adjusting from the boundary conditions:

$$(b): \quad w(x=0) = 0 \;\rightarrow\; B + D = 0 \;\rightarrow\; -B = D \tag{5.43}$$

$$(d): \quad w''(x=l) = A\sin\beta l + B(\cos\beta l - \cosh\beta l) - C\sinh\beta l = 0 \tag{5.44}$$

$$(e): \quad w'''(x=l) = -A\beta^3\cos\beta l + B\beta^3\sin\beta l + C\beta^3\cosh\beta l + D\beta^3\sinh\beta l \tag{5.45}$$

knowing that $w'''(l) = 0$ and $B = -D$, the equation above becomes

$$\Rightarrow -A\cos\beta l + B\sin\beta l + C\cosh\beta l + D\sinh\beta l = 0 \tag{5.46}$$

And the boundary condition (c):

$$\begin{aligned}(c): \; & k_r \cdot \beta(A\cos(\beta\cdot 0) + (-B)\sin(\beta\cdot 0) + C\cosh(\beta\cdot 0) + D\sinh(\beta\cdot 0)) \\ & + k_B\beta^2[A\sin(\beta\cdot 0) + B\cos(\beta\cdot 0) - C\sinh(\beta\cdot 0) + B\cosh(\beta\cdot 0)] = 0\end{aligned}$$

$$\Rightarrow K_r\beta(A + C) + k_B\beta^2(2B) = 0 \;\Big|\; : (k_B\beta^2)$$

$$\Rightarrow \frac{k_r}{2k_B\beta}(A + C) + B = 0 \tag{5.47}$$

Since $\boldsymbol{k} = k_r/k_b$, the solution in matrix notation is represented as follows:

$$\underbrace{\begin{bmatrix} 0 & 1 & 0 & 1 \\ \sin\beta l & \cos\beta l & -\sinh\beta l & -\cosh\beta l \\ -\cos\beta l & \sin\beta l & \cosh\beta l & \sinh\beta l \\ \boldsymbol{k}/2\beta & 1 & \boldsymbol{k}/2\beta & 0 \end{bmatrix}}_{\underline{A}} \begin{bmatrix} A \\ B \\ C \\ D \end{bmatrix} = 0 \tag{5.48}$$

The solution of $det\underline{A} = 0$ is presented in the graph of Figure 57 for the ratio $\boldsymbol{k}$ equal to 0, 1, 10, 100 and 1E+6. This range of $\boldsymbol{k}$ values represents the cases of a simply supported beam ($\boldsymbol{k} \rightarrow 0$), a beam supported by rotational springs with different magnitudes of stiffness ($\boldsymbol{k} =$

$1, \boldsymbol{k} = 10, \boldsymbol{k} = 100$), and a hypothetical case when the rigidity of the rotational spring is so high that the system can be considered as fixed-free ($\boldsymbol{k} \to \infty$).

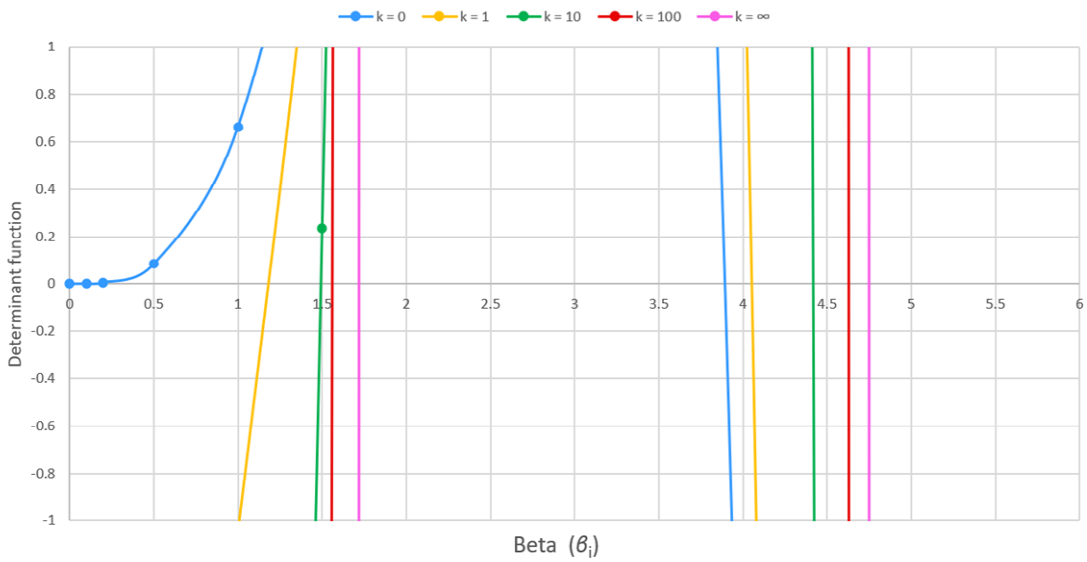

Figure 57: plot of the characteristic equation for the result of $det\underline{A} = 0$. Graph obtained in Microsoft Excel, which has a numeric precision of 15 significant digits that may affect the accuracy of the data collected. The color sequency blue, yellow, green, red, magenta illustrates the plots of functions of k equals to $0, 1, 10, 100, \infty$, respectively.

Now, by analyzing the plot of the determinant function, a few points can be discussed, considering that the stiffness of the beam is constant. Starting with the hypothetical case for the ratio $\boldsymbol{k} = 0$ (graph in blue), where the stiffness of the rotational spring supporting the beam is practically insignificant, it can be observed that β_i is zero for the first and the second eigenmodes. This means that the beam here would exhibit no bending behavior, only a generic motion of rigid bodies. Next, for a rotational spring having the same rigidity as the beam ($\boldsymbol{k} = 1$; graph in yellow), the system demonstrates characteristics of bending vibration with the first and the second eigenmodes $\beta_1 \cong 1.2$ and $\beta_2 \cong 4.1$, respectively. With the increase of the spring stiffness ($\boldsymbol{k} = 10$ and $\boldsymbol{k} = 100$), assuming that the beam is the same, the first eigenfrequency become very close to 1.5 for both these cases, and the second eigenfrequencies are $\beta_2 \cong 4.4$ and $\beta_2 \cong 4.6$, respectively for a spring ten and for a spring one hundred times stiffer than the beam. These are represented by the green and red plots. Here, it is noticed that even with a ten times stiffer spring, the natural frequencies do not differ considerably, meaning that the motion behavior of the beam is not strongly affected by the increase of the spring rigidity by a factor of 10 at the first and the second eigenmodes. However, apparently there is a tendency for β_i to differ more and more at each eigenmode i, for higher eigenfrequencies of the conditions where $\boldsymbol{k} = 10$ and $\boldsymbol{k} = 100$. Although, this was not further verified by the analysis presented here, as only the first and the second eigenfrequencies are being assessed.

Finally, for the case where the spring stiffness is extremely high in relation to the beam ($\boldsymbol{k} = 1 \cdot 10^6$), and the system is approaching a fixed-free state, the eigenvalues are $\beta_1 \cong 1.72$

and $\beta_2 \cong 4.74$, which approximate to the first and the second Euler-Bernoulli fixed-free eigenfrequencies of 1.87 and 4.69, respectively. This case is described by the plot in magenta.

It can be inferred from the results of the determinant function that the presence of a rotational spring implies that the eigenfrequencies for the first and the second modes are lower than the corresponding eigenfrequencies for a fixed-free boundary condition, independently of the magnitude of the spring's stiffness. In addition, the eigenvalues tend to decrease with lower values of the rotational spring stiffness (or lower values of the ratio $\boldsymbol{k}$**)**. In other words, the less stiff the rotational spring is, the lower the eigenfrequencies.

Applying the boundary conditions proposed above to calculate the Young's modulus of the vibrating beam will lead to higher values of E, and consequently higher flexural rigidities in comparison with the fixed-free condition. This occurs because the Young's modulus is inversely proportional to the eigenfrequency β_i (see Equation 2.63). A concrete example can be given using the SiC nanowire number 4 from Table 9, which was evaluated experimentally in this project, based on the fixed-free boundary condition. This nanowire was selected for comparison as it showed a behavior very close to that of a perfect elastic beam, confirmed by the experimental data in Table 9. The Young's modulus of this nanowire was calculated for the three cases described above, $\boldsymbol{k} = 1$, $\boldsymbol{k} = 10$, and $\boldsymbol{k} = 100$, using the resonance frequency detected experimentally at the first mode, and the β_1 obtained with the plot from Figure 57. The resulting modulus are presented in Table 11 and in the graph of Figure 58. The flexural rigidity R was not included in this analysis since it is obtained with the average Young's modulus from all the modes detected for each nanowire. However, it is known that $R = EI$, thus the flexural rigidity increases proportionally with E.

Table 11: Young's modulus of one individual SiC nanowire calculated according to each value of the ratio k, at the first mode of resonance. The error associated to E is 11.7% (Table 10).

Boundary condition	$\boldsymbol{\beta_1}$	E **(GPa)**
$\boldsymbol{k} = 1$	1.2	853
$\boldsymbol{k} = 10$	1.5	349
$\boldsymbol{k} = 100$	1.52	331
Fixed-free	1.875	143

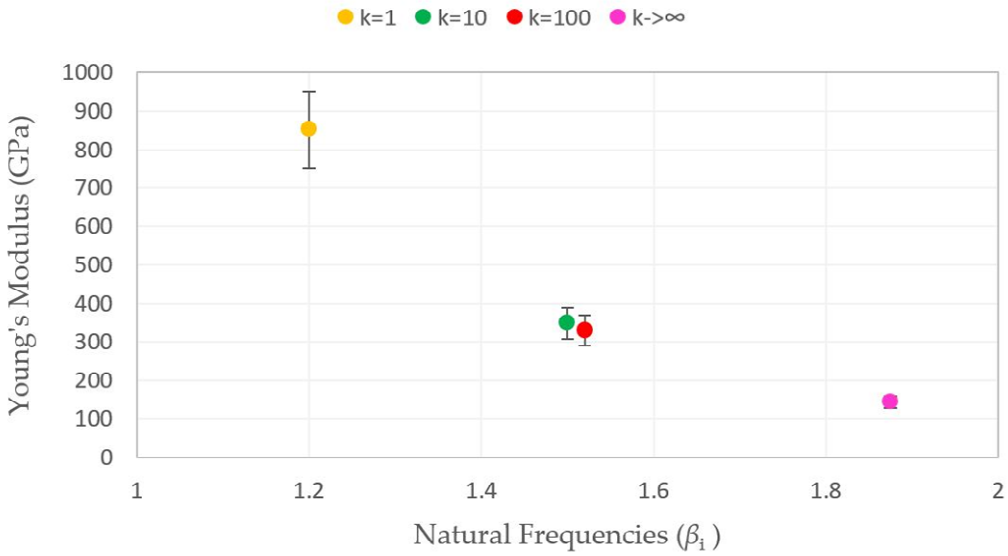

Figure 58: data showing the Young's modulus of an individual SiC nanowire (number 4 from Table 9) calculated for each boundary condition from $k = 1$ to the fixed-free state $k \to \infty$.

Despite the difference of the β_1 values not being very high, the Young's modulus for each state of the boundary condition varies considerably, especially when the ratio $\boldsymbol{k}$ increases from 1 to 10. This is explained by the effect of the term β_i to the fourth power in the equation to calculate the modulus (Equation 2.63). This way, small changes in the values of the natural frequencies β_i will impact strongly on the Young's modulus derived.

The graph above shows clearly the variation of the modulus values for each configuration of boundary conditions. This highlights the importance of defining the appropriate boundary conditions that are being applied to the system. And, in the case of a beam supported by a rotational spring, if the stiffness of the spring is well-known compared to the magnitude of the stiffness of the beam, there are good chances of acquiring more accurate values of E.

6. Remarks

6.1 Recalculation of the error estimation for the MWCNTs

The SiC nanowires presented physical characteristics that were more compatible with the Euler-Bernoulli beam theory than the nanotubes tested in a previous phase of the project. For this reason, an additional step to determine the length deviation of the nanowires was implemented, aiming at increasing the accuracy on the error estimation of their Young's modulus (Section 5.3.3). This procedure was created during the investigation of the SiC NWs, after the error estimation of the MWCNTs was studied. Therefore, here an analysis of a more realistic approach to evaluate the error associated to the Young's modulus of MWCNTs is presented, using the same principle applied for the nanowires.

To define a more authentic value of the error deviation for the length of the MWCNTs, the differences encountered during the length measurements obtained with the two

perspectives of the fiber, 0° and 90° of tilt on the piezo drive (Figure 31), were compared and an average value of 12.7% was observed. This means that the length measured with 90° of tilt on the specimen presented in average an amount 12.7% larger than the value previously measured. Next, this value was applied to the lengths of all the ten MWCNTs tested, and an average value of 1.266 μm was obtained. It was not possible to measure the dimensions of every nanotube from both perspectives because in some cases, the contact point of the fiber with the piezo was located in a cavity of the piezo surface, invisible for observation. Thus, the error associated to the Young's modulus was recalculated with the updated length deviation of ±1.266 μm, and an average value of 59.1% was obtained. The new error values of the Young's modulus for each MWCNT are presented in Table 12.

Table 12: Young's modulus of the MWCNTs from Table 6 with the updated error values

MWCNT	E (GPa)	Error (%)
1	40 ± 34	85.0
2	161 ± 127.8	79.4
3	143.5 ± 53	37.0
4	48 ± 14.2	29.5
5	90.5 ± 43.2	47.7
6	66 ± 24.2	36.7
7	66 ± 57	86.4
8	15.5 ± 10.8	69.4
9	79 ± 46.1	58.4
10	73 ± 45.2	61.9

As can be seen in Table 12, the nanotubes 1, 2, 7, 8 and 10 presented significantly high values of error estimation with the correction on the length deviation. This occurred because these nanotubes are considerably shorter than the others, thus a length deviation of 1.266 μm strongly affected their error estimation. For example, for the nanotube 1, whose length is 6 μm, the length deviation represents 21.1% of its entire length, while for the nanotube 4 it is only 7%. By using an average value of the length deviation for a group of samples with large variations on the dimensions, it is expected that the results of the shorter ones will be more negatively affected.

Since the aim of this work is to evaluate the final stiffness of the nanofibers, an evaluation was made to verify how much an error of 59.1% affects the rigidity calculation. Thus, the flexural rigidity was recalculated using E_b ± 59.1%, and as a result, the order of magnitude of half the nanotubes indeed changed to either below or above the critical rigidity ($R_{critical} \sim 10^{-19}$ N·m²). Naturally, a length deviation of 1.266 μm and 59.1% of error in the Young's modulus are remarkably high values that should not be incorporated into a routinely applicable rigidity measurement technique. Therefore, it is essential to implement a dimension characterization tool that allows the acquisition of the fiber true length, producing therefore quality results.

6.2 Three-dimensional reconstruction of curved nanofibers

The problem of obtaining the right dimensions of curved nanowires has been the work focus of some researchers, aware of the large impact of measurements mistakes on the Young's modulus obtained via resonance frequencies. To overcome this issue, a technique based on the parallax method has been developed by Huang et al. [124]. The parallax method is a well-known principle commonly used in astronomy to measure the distance between stars. It consists of determining the coordinates of an object having different apparent positions by obtaining images from distinguished viewpoints angles. Similarly, this principle was applied in the SEM to form a three-dimensional representation of nanowires. In [124], the authors reconstructed a 3D model of a nanowire by tracing its length on two SEM images acquired from different viewpoint angles, and using epipolar geometry in a MATLAB program developed by them. To estimate the length of the nanowire from the three-dimensional model, the total of pixels of the three-dimensional curve was integrated and divided by the total magnification in the MATLAB program. The larger the tilt or rotation angle, the more accurate was the image reconstruction and consequently the length.

This method for estimating the length of nanowires has been applied by other researchers that investigated the mechanical properties of nanowires with resonance frequencies detection. Zhang et al. characterized the mechanical behavior of silicon carbide nanowires through a nanoscale tensile testing and two different resonance detection tests, via electrical and mechanical excitation. The aim of the study was to compare the Young's modulus obtained from the three different types of tests. To increase the accuracy of the results especially of the excitation tests, the technique developed by Huang et al. was implemented to extract the length of nanowires clamped on the tip of an AFM cantilever (Figure 59). The authors obtained very similar values of Young's modulus from the three testing configurations, which largely was achieved by the certainty on the length value estimated [60].

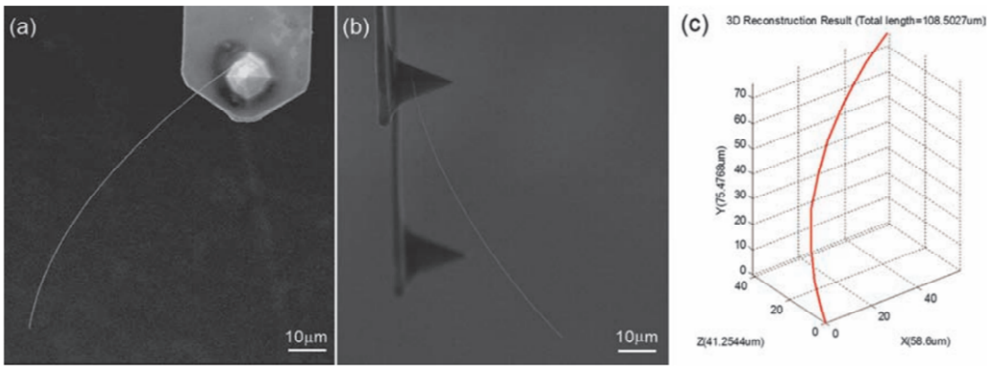

Figure 59: SEM images of a silicon carbide nanowire fixed at the tip of an AFM cantilever, used for the 3D reconstruction of the nanowire: (a) the sample has 0° of tilt; (b) a side view with 90° tilt. (c) 3D model of the nanowire created with the parallax method from Huang et al. [60].

In another study, the authors applied the parallax method from [124] to study the elastic properties of curved boron nanowires by detecting their resonance frequencies as well

[119]. The nanowires were individually attached to the tip of an AFM probe, and mechanically excited with a piezo actuator. To account for the shape deviation from the Euler-Bernoulli beam theory, a correction procedure was proposed based on the vibration of curved beams, using a finite element simulation. The 3D reconstruction of the nanowire was important to permit a reliable correlation of the results obtained experimentally with the results pointed by the numerical analysis.

For future resonance tests using the DySEM technique, and method presented in this work, it is recommended to incorporate this procedure into the routine to define correct dimensions of the nanofibers, before extracting their Young's modulus. For that, a high sensitivity stage tilt needs to be implemented into the Zeiss EVO MA10 SEM to provide high accuracy in the tilt angle control. Upon obtaining SEM images with reliable parameters, and applying the MATLAB source code to obtain the dimensions of the fiber, the modulus can be calculated with the certainty that experimental errors were mitigated.

7. Conclusion

This work sheds light on the fiber toxicological paradigm associated with the possible health risks posed by rigid biopersistent nanofibers. Several types of nanofibers present remarkable properties, being very attractive for commercialization, without having a reliably known Young's modulus characterization. Upon being largely applied in consumer and industrial goods, the nanofibers can be lost into the environment as a consequence of chemical and mechanical degradation processes of their matrices. This could lead to an uncontrolled spread of these materials, becoming a potential hazard subject for nature and society. Therefore, being able to evaluate the rigidity of nanofibers prior to their large-scale commercialization is absolutely essential to promote the development of advanced materials, without compromising the well-being of humans and the balance of ecosystems. For this reason, the focus of this work has been to propose a routinely applicable method to study the rigidity of nanofibers and provide a qualitative analysis of such property.

The proposed method to evaluate the flexural rigidity of nanofibers relies on the detection of resonance frequencies of cantilevered nanofibers via the so-called Dynamic Scanning Electron Microscopy technique. Upon obtaining the resonance frequencies and measuring the fiber's dimensions, the dynamic Young's modulus can be derived using the Euler-Bernoulli beam theory. The flexural rigidity is determined using the Young's modulus value and the second moment of area. This methodology is applicable to nanofibers and nanowires with known material density, exhibiting a beam-like shape and electrically conductive or semiconductive.

The fixation of the nanofibers with a polymeric and not highly stiff material allows for the consideration of another boundary condition rather than the fixed-free to represent the beam supporting state. For this reason, the approach with a rotational spring was presented in Section 5.5, and has demonstrated that if the clamping material is not extremely stiff in comparison to the beam, the values of the non-dimensional resonance frequencies are lower

than the ones used in the fixed-free condition. This leads to the calculation of greater values of Young's modulus, and consequently higher flexural rigidities as well. This means that this approach could be more conservative regarding the evaluation of the flexural rigidity of nanofibers for health and safety purposes. It would detect higher rigidities for nanofibers, and therefore classifying them according to the critical rigidity threshold in a safer way. However, specifically for the carbon nanotubes and the silicon carbide nanowires studied here, this approach would not impact significantly, since the flexural rigidity values obtained through the fixed-free boundary conditions are already above the harmful threshold limit. Nonetheless, for more accurate evaluation of nanofibers stiffness, it is crucial to identify the adequate boundary conditions that are being applied to the excitation system.

The necessity to develop reference methods for nanomechanical testing has been discussed in Section 2.4, as well as the advantages and disadvantages of the existing laboratory established procedures. Here, the mechanical characterization of nanofibers has been presented employing a scanning electron microscope that requires non-sophisticated operational requirements. Compared to other microscopy techniques, the SEM provides a satisfactory range of information during the experimental tests, and it is an alternative to TEM-based tests. The transmission electron microscope is in general a complex and delicate instrument with reduced space for design modifications of the sample holder, limiting the possibilities for innovation. It requires special sample preparation, and a profound electron microscopy know-how, especially to avoid damage of imaged fibers resulting from high beam energies. In addition, it is a highly costly equipment. The SEM instruments used in this work facilitated the experimental set up and did not demand high levels of operational skills. However, it was beneficial to use an ultra-high-resolution SEM for reliable shape measurement and observation of structural details and defects of the MWCNTs investigated. To decrease the errors associated with dimensions measurements, for arched or curvilinear nanofibers particularly, it is recommended to analyze the three-dimensional shape of the fiber. This can be achieved in the SEM by integrating into the experimental routine a procedure to reconstruct a 3D model of the fibers from its stereo-pairs images, obtained with different tilt or rotation angles, combined with and a numerical formulation. For nearly perfect straight fibers, the length measurement from two images with a tilt difference of approximate to 90° is sufficient to result in acceptable error margins.

With the method presented here, the Young's modulus of multi-walled carbon nanotubes and silicon carbide nanowires were successfully obtained. The modulus values obtained for the MWCNTs ranged from 15 to 161 GPa, which is in agreement with the reported data. The literature, however, covers a very wide range of nanotubes diameters and Young's modulus from 5 to 1360 GPa. The reported modulus values appeared to strongly depend on the synthesis technique, which impacts on the fiber diameter, the presence of structural defects, and on the crystallinity. The data suggests that MWCNTs from cCVD synthesis tended to exhibit lower Young's modulus values and were thus in-line with our results. For half of the nanotubes only the fundamental mode of frequency was detected, and for the other half, the ratio ν_2/ν_1 slightly deviate from the theoretical value of 6.27 for perfect linear elastic beams. Since the nanotubes revealed a curvilinear morphology, the principle of vibration of curved beams was proposed as an alternative to the Euler-Bernoulli beam theory, which applies

exclusively to straight beams. The Young's modulus of one single nanotube calculated via the curved beams theory was 27% smaller than the value obtained via E-B. This theory can be applied for curved nanofibers in the future, provided that the fiber has one uniform arc that permits the extraction of the curvature radius.

The silicon carbide nanowires investigated have shown to be a very appropriate material for the method proposed here. It has a very bulky straight configuration, and its semiconducting properties renders high quality images in the SEM without charging effects. For most of the nanowires, both first and second modes of resonance were detected, with a ν_2/ν_1 ratio very close to the theoretical one. For one fiber, the third mode was reached, as well. The Young's modulus for these fibers ranged between 105 and 340 GPa, which is in accordance with the literature values. However, a wide variety of Young's modulus has been reported for SiC nanowires, due to their innumerous nanostructured morphologies. The nanowires presented an average Young's modulus error of 18.6%, after a detailed investigation of the length measurement, which strongly affects the Young's modulus calculation. This error is relatively low, compared to other reported techniques, such as force versus displacement tests in the atomic force microscope, as described in Section 2.4. The damping during the resonance detection of the SiC NWs was significantly low, as the quality factors encountered were between 2800 and 5200.

Finally, the flexural rigidity of both nanofibers was calculated, and characterized according to the rigidity threshold of 10^{-19} N·m^2, which is the critical value that has to be overcome by the macrophages to perform a successful phagocytosis in the presence of nanofibers. All the fibers tested here presented flexural rigidity in the order of 10^{-19} N·m^2 or above, which classifies them as potentially hazardous agents if inhaled by humans. The data obtained for the MWCNTs, showed a threshold diameter of ~ 75 nm, suggesting that nanotubes of the same type, and thinner than 75 nm can be considered harmless for the lung's cells. Although flexural rigidity scales only linearly with the Young's modulus but with the 4th power of fiber diameter, in a specific diameter range, MWCNTs of a larger diameter may not necessarily be of higher toxicological relevance than thinner ones, since the Young's modulus may increase with decreasing diameter due to microstructure-related reasons. Therefore, further progress appears necessary in routinely and reliably measurement of the Young's modulus of nanofibers.

For the case of CNTs specifically, an acceptable path towards large-scale application is by fabrication of ultra-long CNTs that reach centimeters in length by developing the techniques of horizontally aligned CNTs [125] or by the fabrication of CNTs bundles [126]. When the nanofibers are manipulated to become longer, they would not pose harm to the lungs, because bigger particles are trapped in the upper airway before they reach the lungs.

MWCNTs are a very unique material with outstanding properties and with much potential to enable the development of advanced materials and bring solutions that could push society towards a new era, and the same applies to other nanofibers such as silicon carbide nanowires. Therefore, it would be a significant throwback for science and technology if these materials could not be vastly applied in distinguished areas of electronics and engineering due to the harm they may cause to humans and to the environment. Hence, it is crucial to establish

reliable and accurate testing methods, which allow a controlled evaluation of the mechanical properties of nanofibers and that can be implemented for large scale procedures. This is what was intended during this work, to implement a procedure that extracts the elasticity information of multiple fibers by submitting them to resonance frequencies detection.

8. Research Prospects

One of the most critical points in resonance detection tests of cantilevered specimens is to obtain accurate length and diameter values. As emphasized previously, uncertainties in the values of length lead to unreliable results of the elastic properties. Hence, the three-dimensional metrology of a fiber's shape and orientation must be further improved. This could be done by applying eccentric SEM stage rotations to obtain fiber images at defined viewing angles, and using the parallax method as mathematical model described in Section 6.2. Additionally, secondary electrons detectors at different viewing angles or a segmented back-scattered electron detector may help to obtain improved fiber shape and orientation information [127]. Furthermore, dynamic structural changes like the onset of elastic bending deformations during excitation deserve further microscopic analysis since they imply deviations from the assumed simplistic beam mechanics, as well as parametric resonances.

It would be desirable to further reduce the time required to find fiber resonances. One approach could be not to perform continuous frequency sweeps but to use bandwidth-filtered noise to excite fiber oscillations in non-overlapping frequency ranges. By halving the interval size and comparing the fiber response, the resonance frequency range could by narrowed down. Alternatively, or in addition, more than one fiber could be analyzed simultaneously. This would require a fast "fiber-tip-hopping" SEM imaging algorithm that, during a frequency sweep, sequentially images several fiber tips at predetermined locations to monitor their oscillation and demultiplexes the resulting lock-in-amplifier signal.

To improve detection of resonances requires one to enhance oscillation amplitudes. For this, the energy dissipation at the contact point between a nanofiber and its base-embedding layer must be reduced by increasing the layer stiffness. For this purpose, hardened PEDOT:PSS that was crosslinked with glycerol could be studied [128]. Alternatively, a low melting point metal alloy used as the embedding layer could reduce dissipation even further. The preparation of free-standing nanofibers on an alloy-coated piezoelectric actuator by electrostatic precipitation (Section 4.1), however, would require designing a heating unit to keep the alloy melted at a high electrostatic potential, necessary to attract and embed charged nanofibers.

Calibration of routinely applicable rigidity measurement techniques will require the development of reference fiber materials. The silicon carbide nanowires studied here have favorable properties to be employed as a reference fiber.

9. References

1. Chen, Y., X. An, and X. Liao, *Mechanical behaviors of nanowires.* Applied Physics Reviews, 2017. **4**(3): p. 031104.
2. Poncharal, P., et al., *Electrostatic deflections and electromechanical resonances of carbon nanotubes.* Science, 1999. **283**(5407): p. 1513-6.
3. Salvetat, J.P., et al., *Elastic modulus of ordered and disordered multiwalled carbon nanotubes.* Advanced Materials, 1999. **11**(2): p. 161-165.
4. Gao, R., et al., *Nanomechanics of individual carbon nanotubes from pyrolytically grown arrays.* Phys Rev Lett, 2000. **85**(3): p. 622-5.
5. Yu, M.F., et al., *Strength and breaking mechanism of multiwalled carbon nanotubes under tensile load.* Science, 2000. **287**(5453): p. 637-40.
6. Wang, Z.L., et al., *Mechanical and electrostatic properties of carbon nanotubes and nanowires.* Materials Science & Engineering C-Biomimetic and Supramolecular Systems, 2001. **16**(1-2): p. 3-10.
7. Lukić, B., et al., *Elastic modulus of multi-walled carbon nanotubes produced by catalytic chemical vapour deposition.* Applied Physics A, 2005. **80**(4): p. 695-700.
8. Garcia-Sanchez, D., et al., *Mechanical detection of carbon nanotube resonator vibrations.* Phys Rev Lett, 2007. **99**(8): p. 085501.
9. Ding, W., et al., *Modulus, Fracture Strength, and Brittle vs. Plastic Response of the Outer Shell of Arc-grown Multi-walled Carbon Nanotubes.* 2007. **47**(1): p. 25-36.
10. Biedermann, L.B., et al., *Flexural vibration spectra of carbon nanotubes measured using laser Doppler vibrometry.* Nanotechnology, 2009. **20**(3): p. 035702.
11. Jackman, H., P. Krakhmalev, and K. Svensson, *Mechanical behavior of carbon nanotubes in the rippled and buckled phase.* Journal of Applied Physics, 2015. **117**(8).
12. Gorman, J., *Taming high-tech particles: Cautious steps into the nanotech future.* Science News, 2002. **161**(13): p. 200-201.
13. Donaldson, K., et al., *Asbestos, carbon nanotubes and the pleural mesothelium: a review of the hypothesis regarding the role of long fibre retention in the parietal pleura, inflammation and mesothelioma.* Part Fibre Toxicol, 2010. **7**: p. 5.
14. Boyles, M., et al., *The Significance and Insignificance of Carbon Nanotube-Induced Inflammation.* Fibers, 2014. **2**(1): p. 45-74.
15. Donaldson, K. and C.L. Tran, *An introduction to the short-term toxicology of respirable industrial fibres.* Mutat Res, 2004. **553**(1-2): p. 5-9.
16. Golden, J., *Whisker-like Fibres from Chrysotile Asbestos.* Nature, 1968. **220**(5162): p. 64-65.
17. World Health, O., *WHO guidelines on protecting workers from potential risks of manufactured nanomaterials*. 2017, Geneva: World Health Organization.
18. Han, J.H., et al., *Monitoring multiwalled carbon nanotube exposure in carbon nanotube research facility.* Inhal Toxicol, 2008. **20**(8): p. 741-9.
19. Schlagenhauf, L., F. Nüesch, and J. Wang, *Release of Carbon Nanotubes from Polymer Nanocomposites.* Fibers, 2014. **2**(2): p. 108-127.
20. Rhiem, S., et al., *Release of 14C-labelled carbon nanotubes from polycarbonate composites.* Environ Pollut, 2016. **215**: p. 356–365.
21. Lam, C.W., et al., *Pulmonary toxicity of single-wall carbon nanotubes in mice 7 and 90 days after intratracheal instillation.* Toxicol Sci, 2004. **77**(1): p. 126-34.
22. Muller, J., et al., *Respiratory toxicity of multi-wall carbon nanotubes.* Toxicol Appl Pharmacol, 2005. **207**(3): p. 221-31.
23. Donaldson, K., et al., *Carbon nanotubes: a review of their properties in relation to pulmonary toxicology and workplace safety.* Toxicol Sci, 2006. **92**(1): p. 5-22.

24. Schinwald, A. and K. Donaldson, *Use of back-scatter electron signals to visualise cell/nanowires interactions in vitro and in vivo; frustrated phagocytosis of long fibres in macrophages and compartmentalisation in mesothelial cells in vivo.* Particle and Fibre Toxicology, 2012. **9**.
25. Nagai, H., et al., *Diameter and rigidity of multiwalled carbon nanotubes are critical factors in mesothelial injury and carcinogenesis.* Proc Natl Acad Sci U S A, 2011. **108**(49): p. E1330-8.
26. Schröter, M.A., H. Sturm, and M. Holschneider, *Phase and amplitude patterns in DySEM mappings of vibrating microstructures.* Nanotechnology, 2013. **24**(21): p. 215701.
27. Schröter, M.A., et al., *Enhanced DySEM imaging of cantilever motion using artificial structures patterned by focused ion beam techniques.* Journal of Micromechanics and Microengineering, 2016. **26**(3): p. 035010.
28. *Webpage fictiv*. Last access: March 22, 2021; Available from: https://www.fictiv.com/articles/engineering-fundamentals-refresh-strength-vs-stiffness-vs-hardness.
29. Callister, W.D., *Materials Science and Engineering: An Introduction*. 7th ed. ed. 1997, New York: John Wiley & Sons.
30. Bertram, A. and R. Glüge, *Solid mechanics: Theory, modeling, and problems*. 2015. 1-318.
31. Asaro, R. and V.A. Lubarda, *Mechanics of Solids and Materials.* Mechanics of Solids and Materials, 2006.
32. Giurgiutiu, V., *Chapter 2 - Fundamentals of Aerospace Composite Materials*, in *Structural Health Monitoring of Aerospace Composites*, V. Giurgiutiu, Editor. 2016, Academic Press: Oxford. p. 25-65.
33. Inman, D.J., *Engineering Vibration*. 2001: Prentice Hall.
34. Mazurek, F.P.B.E.R.J.J.T.D.D.F., *Mechanics of materials*. 2006, New York, NY: McGraw-Hill Education.
35. Butt, H.J. and M. Jaschke, *Calculation of thermal noise in atomic force microscopy.* Nanotechnology, 1995. **6**(1): p. 1-7.
36. James M. Gere, S.P.T., *Mechanics of Materials*. Fourth Edition ed. 1997: PWS Publishing Company.
37. Rao, S.S., *Vibration of Continuous Systems*. 2007, Hoboken, New Jersey: John Wiley & Sons, Inc.
38. Guhados, G., et al., *Simultaneous measurement of Young's and shear moduli of multiwalled carbon nanotubes using atomic force microscopy.* Journal of Applied Physics, 2007. **101**(3): p. 033514.
39. Lee, K., et al., *Diameter-Dependent Elastic Modulus Supports the Metastable-Catalyst Growth of Carbon Nanotubes.* Nano Letters, 2007. **7**(6): p. 1598-1602.
40. Wang, S., Z. Shan, and H. Huang, *The Mechanical Properties of Nanowires.* Advanced Science, 2017. **4**(4): p. 1600332.
41. Wong, E.W., P.E. Sheehan, and C.M. Lieber, *Nanobeam mechanics: Elasticity, strength, and toughness of nanorods and nanotubes.* Science, 1997. **277**(5334): p. 1971-1975.
42. Song, J., et al., *Elastic Property of Vertically Aligned Nanowires.* Nano Letters, 2005. **5**(10): p. 1954-1958.
43. Wang, Z.L., P. Poncharal, and W.A. de Heer, *Measuring physical and mechanical properties of individual carbon nanotubes by in situ TEM.* Journal of Physics and Chemistry of Solids, 2000. **61**(7): p. 1025-1030.
44. Vincent, P., et al., *Driving self-sustained vibrations of nanowires with a constant electron beam.* Physical Review B - PHYS REV B, 2007. **76**.
45. Perisanu, S., et al., *Mechanical properties of SiC nanowires determined by scanning electron and field emission microscopies.* Physical Review B, 2008. **77**(16): p. 165434.
46. Zeng, H., et al. *Simultaneous characterization of mechanical and electrical properties of nanowire using MEMS device*. in *Transducers & Eurosensors XXVII: The 17th International Conference on Solid-State Sensors, Actuators and Microsystems*. 2013.

47. Hu, P., et al., *Synthesis and characterization of ultralong SiC nanowires with unique optical properties, excellent thermal stability and flexible nanomechanical properties.* Scientific Reports, 2017. **7**(1): p. 3011.
48. Yu, M.-F., et al., *Realization of parametric resonances in a nanowire mechanical system with nanomanipulation inside a scanning electron microscope.* Physical Review B, 2002. **66**(7): p. 073406.
49. Cheng, G., et al., *Mechanical Properties of Silicon Carbide Nanowires: Effect of Size-Dependent Defect Density.* Nano Letters, 2014. **14**(2): p. 754-758.
50. Yang, Y., et al., *Size-dependent mechanical behavior of a-silicon carbide nanowires under in-situ transmission electron microscopy tensile tests.* Materials Research Express, 2019. **6**(4): p. 045009.
51. Wang, Y., et al., *In situTEM/SEM electronic/mechanical characterization of nano material with MEMS chip.* Journal of Semiconductors, 2014. **35**(8): p. 081001.
52. Zhang, Y., et al., *A MEMS Tensile Testing Device for Mechanical Characterization of Individual Nanowires.* 2010: p. 2581-2584.
53. Peng, B., et al., *Measurements of near-ultimate strength for multiwalled carbon nanotubes and irradiation-induced crosslinking improvements.* Nature Nanotechnology, 2008. **3**(10): p. 626-631.
54. Guo, H., et al., *Mechanics and Dynamics of the Strain-Induced M1–M2 Structural Phase Transition in Individual VO2 Nanowires.* Nano Letters, 2011. **11**(8): p. 3207-3213.
55. Zhang, H., et al., *Approaching the ideal elastic strain limit in silicon nanowires.* Science Advances, 2016. **2**(8): p. e1501382.
56. Jackman, H., P. Krakhmalev, and K. Svensson, *Measurements of the critical strain for rippling in carbon nanotubes.* Applied Physics Letters, 2011. **98**(18).
57. Vogl, L.M., et al., *Transforming layered MoS2 into functional MoO2 nanowires.* Nanoscale, 2019. **11**(24): p. 11687-11695.
58. Ma, J., et al., *Effect of different oxide thickness on the bending Young's modulus of SiO2@SiC nanowires.* Scientific Reports, 2016. **6**(1): p. 18994.
59. Ding, W., et al., *Modulus, Fracture Strength, and Brittle vs. Plastic Response of the Outer Shell of Arc-grown Multi-walled Carbon Nanotubes.* Experimental Mechanics, 2006. **47**(1): p. 25-36.
60. Zhang, H., W. Ding, and D.K. Aidun, *Mechanical Properties of Crystalline Silicon Carbide Nanowires.* Journal of Nanoscience and Nanotechnology, 2015. **15**(2): p. 1660-1668.
61. Ricci, J. and C. Cetinkaya, *Air-coupled acoustic method for testing and evaluation of microscale structures.* The Review of scientific instruments, 2007. **78**: p. 055105.
62. Zhou, P., et al., *The Young's modulus of high-aspect-ratio carbon/carbon nanotube composite microcantilevers by experimental and modeling validation.* Applied Physics Letters, 2015. **106**(11): p. 111908.
63. Hassan, M.O., A. Nojeh, and K. Takahata, *A microcantilever of self-suspended carbon nanotube forest for material characterization and sensing applications.* Applied Physics Letters, 2020. **117**(1): p. 013101.
64. Oliver, W.C. and G.M. Pharr, *An improved technique for determining hardness and elastic modulus using load and displacement sensing indentation experiments.* Journal of Materials Research, 1992. **7**(6): p. 1564-1583.
65. Chrobak, D., et al., *Deconfinement leads to changes in the nanoscale plasticity of silicon.* Nature Nanotechnology, 2011. **6**(8): p. 480-484.
66. Wang, Y.-C., et al., *In situ TEM study of deformation-induced crystalline-to-amorphous transition in silicon.* NPG Asia Materials, 2016. **8**(7): p. e291-e291.
67. Kim, Y.-J., et al., *Exploring Nanomechanical Behavior of Silicon Nanowires: AFM Bending Versus Nanoindentation.* Advanced Functional Materials, 2011. **21**(2): p. 279-286.
68. Jorio, A., G. Dresselhaus, and M. Dresselhaus, *Carbon Nanotubes: Advanced Topics in the Synthesis, Structure, Properties and Applications*. Vol. 111. 2008.
69. Iijima, S., *Helical microtubules of graphitic carbon.* Nature, 1991. **354**(6348): p. 56-58.

70. Mike Williams, R.U. *Phys.org*. July 13, 2015 March 23, 2021]; Available from: https://phys.org/news/2015-07-scientists-advance-tunable-carbon-capture-materials.html.
71. Wikiwand. *Single-walled carbon nanohorn*. 2022 16 July 2022]; Available from: https://www.wikiwand.com/en/Single-walled_carbon_nanohorn.
72. LOOS, M.R. *Webpage CNT Composites*. Last access: March 31, 2021]; Available from: https://sites.google.com/site/cntcomposites/structure-of-cnts.
73. Zaytseva, O. and G. Neumann, *Carbon nanomaterials: Production, impact on plant development, agricultural and environmental applications.* Chemical and Biological Technologies in Agriculture, 2016. **3**.
74. Xu, Y.-Q., et al., *Controlled Multistep Purification of Single-Walled Carbon Nanotubes.* Nano Letters, 2005. **5**(1): p. 163-168.
75. MacKenzie, K.J., O.M. Dunens, and A.T. Harris, *An Updated Review of Synthesis Parameters and Growth Mechanisms for Carbon Nanotubes in Fluidized Beds.* Industrial & Engineering Chemistry Research, 2010. **49**(11): p. 5323-5338.
76. Meyer-Plath, A., et al., *Plasma-thermal purification and annealing of carbon nanotubes.* Carbon, 2012. **50**: p. 3934-3942.
77. Treacy, M.M.J., T.W. Ebbesen, and J.M. Gibson, *Exceptionally high Young's modulus observed for individual carbon nanotubes.* Nature, 1996. **381**(6584): p. 678-680.
78. Yamamoto, G., et al., *The influence of nanoscale defects on the fracture of multi-walled carbon nanotubes under tensile loading.* Diamond and Related Materials - DIAM RELAT MATER, 2010. **19**.
79. Demczyk, B.G., et al., *Direct mechanical measurement of the tensile strength and elastic modulus of multiwalled carbon nanotubes.* Materials Science and Engineering a-Structural Materials Properties Microstructure and Processing, 2002. **334**(1-2): p. 173-178.
80. Rasmussen, K., et al., *Multi-walled carbon nanotubes, NM-400, NM-401, NM-402, NM-403, characterisation and physico-chemical properties*, in *JRC Science and Policy Reports*. 2014, EU Joint Research Center: Brussels, Belgium.
81. Kim, S.H., G.W. Mulholland, and M.R. Zachariah, *Density measurement of size selected multiwalled carbon nanotubes by mobility-mass characterization.* Carbon, 2009. **47**(5): p. 1297-1302.
82. Zhang, X., et al., *Shape and Doping Enhanced Field Emission Properties of Quasialigned 3C-SiC Nanowires.* The Journal of Physical Chemistry C, 2010. **114**(18): p. 8251-8255.
83. Feng, X.L., et al., *Low Voltage Nanoelectromechanical Switches Based on Silicon Carbide Nanowires.* Nano Letters, 2010. **10**(8): p. 2891-2896.
84. Niu, J.J., J.N. Wang, and Q.F. Xu, *Aligned Silicon Carbide Nanowire Crossed Nets with High Superhydrophobicity.* Langmuir, 2008. **24**(13): p. 6918-6923.
85. Nhuapeng, W., et al., *Fabrication and mechanical properties of silicon carbide nanowires/epoxy resin composites.* Current Applied Physics, 2008. **8**(3): p. 295-299.
86. Rybak, A., et al., *Synthesis of polystyrene coated SiC nanowires as fillers in a polyurethane matrix for electromechanical conversion.* Nanotechnology, 2010. **21**(14): p. 145610.
87. Righi, M.C., et al., *Ab initio Simulations of Homoepitaxial SiC Growth.* Physical review letters, 2003. **91**: p. 136101.
88. Chen, S., et al., *Silicon Carbide Nanowires and Electronics*. 2019. p. 237-335.
89. Wu, R., et al., *Tuning the morphologies of SiC nanowires via the control of growth temperature, and their photoluminescence properties.* Nanotechnology, 2008. **19**(33): p. 335602.
90. Wang, D.-H., et al., *Periodically twinned SiC nanowires.* Nanotechnology, 2008. **19**(21): p. 215602.
91. Dixkens, J. and H. Fissan, *Development of an Electrostatic Precipitator for Off-Line Particle Analysis.* Aerosol Science and Technology, 1999. **30**(5): p. 438-453.
92. Fortini, R., et al., *Measurement of Flexural Rigidity of Multi-Walled Carbon Nanotubes by Dynamic Scanning Electron Microscopy.* Fibers, 2020. **8**(5).

93. Schröter, M.A., M. Holschneider, and H. Sturm, *Analytical and numerical analysis of imaging mechanism of dynamic scanning electron microscopy.* Nanotechnology, 2012. **23**(43): p. 435501.
94. Dr. Asmus Meyer-Plath, D.D.K., *Resonance Analysis of Nanofibres: Theoretical Background and FEM Simulation*. 2018: Bundesanstalt für Arbeitsschutz und Arbeitsmedizin (BAuA Berlin).
95. Zhou, J., I. Aguilar Ventura, and G. Lubineau, *Probing the Role of Poly(3,4-ethylenedioxythiophene)/Poly(styrenesulfonate)-Coated Multiwalled Carbon Nanotubes in the Thermal and Mechanical Properties of Polycarbonate Nanocomposites.* Industrial & Engineering Chemistry Research, 2014. **53**(9): p. 3539-3549.
96. Li, Y., R. Tanigawa, and H. Okuzaki, *Soft and flexible PEDOT/PSS films for applications to soft actuators.* Smart Materials and Structures, 2014. **23**(7): p. 074010.
97. Fankhänel, J., et al., *Mechanical Properties of Boehmite Evaluated by Atomic Force Microscopy Experiments and Molecular Dynamic Finite Element Simulations.* Journal of Nanomaterials, 2016. **2016**: p. 13.
98. Zhou, J., et al., *The temperature-dependent microstructure of PEDOT/PSS films: Insights from morphological, mechanical and electrical analyses.* Journal of Materials Chemistry C, 2014. **2**: p. 9903-9910.
99. Shan, W., T. Lu, and C. Majidi, *Soft-matter composites with electrically tunable elastic rigidity.* Smart Materials and Structures, 2013. **22**(8): p. 085005.
100. Buckner, T.L., et al., *Enhanced Variable Stiffness and Variable Stretchability Enabled by Phase-Changing Particulate Additives.* Advanced Functional Materials, 2019. **29**(50): p. 1903368.
101. Kumar, M. and Y. Ando, *Chemical Vapor Deposition of Carbon Nanotubes: A Review on Growth Mechanism and Mass Production.* Journal of nanoscience and nanotechnology, 2010. **10**: p. 3739-58.
102. Tibbetts, G.G., *Vapor-Grown Carbon Fibers*, in *Carbon Fibers, Filaments and Composites*, J.L. Figueiredo, et al., Editors. 1990, Kluwer Academic Publis: Dordrecht.
103. Tibbetts, G.G. and C.P. Beetz, *Mechanical properties of vapour-grown carbon fibres.* Journal of Physics D: Applied Physics, 1987. **20**(3): p. 292-297.
104. Wang, M., et al., *Effect of defects on resonance of carbon nanotubes as mass sensors.* Applied Physics Letters, 2006. **88**(11).
105. Qin, Q., et al., *Measuring True Young's Modulus of a Cantilevered Nanowire: Effect of Clamping on Resonance Frequency.* Small, 2012. **8**(16): p. 2571-2576.
106. Purcell, S.T., et al., *Tuning of nanotube mechanical resonances by electric field pulling.* Phys Rev Lett, 2002. **89**(27): p. 276103.
107. Brand, O., et al., *Resonant MEMS: Fundamentals, Implementation, and Application*. 2015, New York, NY, USA Wiley.
108. Sazonova, V., et al., *A tunable carbon nanotube electromechanical oscillator.* Nature, 2004. **431**(7006): p. 284-7.
109. Witkamp, B., M. Poot, and H.S.J. van der Zant, *Bending-Mode Vibration of a Suspended Nanotube Resonator.* Nano Letters, 2006. **6**(12): p. 2904-2908.
110. Liu, J.Z., Q. Zheng, and Q. Jiang, *Effect of a rippling mode on resonances of carbon nanotubes.* Phys Rev Lett, 2001. **86**(21): p. 4843-6.
111. Shima, H., *Buckling of Carbon Nanotubes: A State of the Art Review.* Materials (Basel), 2011. **5**(1): p. 47-84.
112. Wang, C.G., et al., *Buckling behavior of carbon nanotubes under bending: From ripple to kink.* Carbon, 2016. **102**: p. 224-235.
113. Sumpter, B.G. and D.W. Noid, *The onset of instability in nanostructures: The role of nonlinear resonance.* The Journal of Chemical Physics, 1995. **102**(16): p. 6619-6622.
114. Arroyo, M. and T. Belytschko, *Nonlinear mechanical response and rippling of thick multiwalled carbon nanotubes.* Phys Rev Lett, 2003. **91**(21): p. 215505.
115. Wang, X.Y. and X. Wang, *Numerical simulation for bending modulus of carbon nanotubes and some explanations for experiment.* Composites Part B: Engineering, 2004. **35**(2): p. 79-86.

116. Arthur, W.L. and S.Q. Mohamad, *Vibrations of Continuous Systems*. 2011, New York: McGraw-Hill Education.
117. Baxy, A. and A. Sarkar, *Natural frequencies of a rotating curved cantilever beam: A perturbation method-based approach.* Proceedings of the Institution of Mechanical Engineers, Part C: Journal of Mechanical Engineering Science, 2020. **234**: p. 095440621989911.
118. Soedel, W., *Vibrations of Shells and Plates*. 3rd Edition ed. 2004, Boca Raton: CRC Press.
119. Calabri, L., et al., *Resonance of curved nanowires.* Journal of Physics: Condensed Matter, 2006. **18**(33): p. S2175-S2183.
120. Pickering, E., et al., *In situ mechanical resonance behaviour of pristine and defective zinc blende GaAs nanowires.* Nanoscale, 2018. **10**(5): p. 2588-2595.
121. Broßell, D., et al., *A human risk banding scheme for high aspect-ratio materials*. 2020.
122. Ding, W., et al., *Mechanics of hydrogenated amorphous carbon deposits from electron-beam-induced deposition of a paraffin precursor.* Journal of Applied Physics, 2005. **98**(1): p. 014905.
123. Kracht, P.D.-I.K., *Study of the dependence of the first natural frequency on the ratio between the bearing stiffness and the bending stiffness of a beam.* 2021.
124. Huang, Z., et al., *Three-dimensional representation of curved nanowires.* Journal of microscopy, 2005. **216**: p. 206-14.
125. Zhang, R., Y. Zhang, and F. Wei, *Horizontally aligned carbon nanotube arrays: Growth mechanism, controlled synthesis, characterization, properties and applications.* Chem. Soc. Rev., 2017. **46**.
126. Bai, Y., et al., *Carbon nanotube bundles with tensile strength over 80 GPa.* Nature Nanotechnology, 2018. **13**(7): p. 589-595.
127. Hemmleb, M., et al., *3D surface reconstruction with segmented BSE detector: New improvements and application for fracture analysis in SEM*. 2016: Wiley-VCH Verlag GmbH & Co. KgaA: Weinheim, Germany p. 489-490.
128. Kim, J., et al., *Enhanced Humid Reliability of Organic Thermoelectrics via Crosslinking with Glycerol.* Nanomaterials, 2019. **9**(11).